isvr Institute of Sound and Vibration Research

Active Control of Sound Transmission through Panels with Flexible Boundaries under Deterministic and Stochastic Excitation

J Rohlfing and P Gardonio

ISVR Technical Memorandum Nº 977

November 2007

University of Southampton

SCIENTIFIC PUBLICATIONS BY THE ISVR

Technical Reports are published to promote timely dissemination of research results by ISVR personnel. This medium permits more detailed presentation than is usually acceptable for scientific journals. Responsibility for both the content and any opinions expressed rests entirely with the author(s).

Technical Memoranda are produced to enable the early or preliminary release of information by ISVR personnel where such release is deemed to the appropriate. Information contained in these memoranda may be incomplete, or form part of a continuing programme; this should be borne in mind when using or quoting from these documents.

Contract Reports are produced to record the results of scientific work carried out for sponsors, under contract. The ISVR treats these reports as confidential to sponsors and does not make them available for general circulation. Individual sponsors may, however, authorize subsequent release of the material.

UNIVERSITY OF SOUTHAMPTON

INSTITUTE OF SOUND AND VIBRATION RESEARCH

SIGNAL PROCESSING & CONTROL GROUP

Active Control of Sound Transmission Through Panels with Flexible Boundaries under Deterministic and Stochastic Excitation

by

J Rohlfing and P Gardonio

ISVR Technical Memorandum No. 977

November 2007

Authorized for issue by
Prof R Allen
Group Chairman

Acknowledgement

This work was conducted as part of a project within the European Doctorate in Sound and Vibration Studies program (EDSVS), which is financed by the European Commission under a Marie Curie Fellowship scheme.

Contents

List of Tables

List of Figures

Abstract

Environmental and economic considerations increase the demand for weight optimized structures. This often conflicts with the requirement for sound transmission reduction and acoustic comfort. In recent years smart panels comprising active components have therefore been a field of increasing research interest.

Most studies on smart panels have been restricted to well defined boundaries and low audio frequencies where the structural response is dominated by discrete resonant modes. Many practical structures comprise of complicated frameworks covered by thin, plate-like components with uncertain boundaries. With increasing frequency resonant modes overlap and boundary uncertainties become increasingly important in the prediction of the structural response.

Within this report a prediction model for the sound transmission through a smart panel with decentralized velocity feedback loops is introduced. Subsequently the model is extended to incorporate fluid loading and flexible boundaries. This model allows deterministic and stochastic disturbances to be considered. A number of typical excitations i.e. plane wave, rain on the roof, acoustic diffuse field and turbulent boundary layer are discussed. Simulation results for control configurations, fluid loading, flexible boundaries, deterministic and stochastic excitation are presented.

In continuation of this project, this prediction model will be used in systematic simulation studies to investigate the performance of smart panels with uncertain boundaries. In future it may be possible to extend the model to more complex vibro-acoustic systems. It is also intended to cast the model into a stochastic formulation that directly provides the average response of the panel with reference to variations of boundary conditions.

Nomenclature

Symbol	Description	Unit
Latin Letters:		
b	Damping coefficient	Ns/m
c	Wave speed	m/s
d	diameter	m
f	Frequency	Hz
h	Thickness	m
j	Imaginary unit defined as: $j = \sqrt{-1}$	
k	Wavenumber	rad/m
l	length	m
m	Mass	kg
p	Acoustic Pressure amplitude	N/m^2
r_1	reflection coefficient	
r_2	Absolute distance between elements	
s	Stiffens	N/m
t	Time	s
w	Displacement in the z-axis	m
x	x-coordinate (plate axis)	m
y	y-coordinate (plate axis)	m
z	z-coordinate (perpendicular to plate)	m
A	Panel surface area	m^2
D	Flexural rigidity	Nm^2
E_1	Young's modulus of elasticity	N/m^2

E_2	Energy	Ws
F	Force	N
G	Modal flexibility	m/N
H	Control gain	
I	Second moment of area	m^4
M_1	Total number (modes)	
M_2	Moment	Nm
M_3	Mach number	
N	Total number	
P	Power	W
U	Speed	m/s
Y	Mobility	m/(Ns)
Z	Impedance	Ns/m

Greek Letters:

η	Damping loss factor	
θ	Angle of incidence angle relative to surface normal	rad or deg
ν	Poisson's ratio	
ρ	Material density	kg/m^3
σ_1	Radiation efficiency	
σ_2	Standard deviation	
τ	Transmission coefficient	
φ	Angle of incidence relative to x axis	rad or deg
ω	Rotational frequency	rad/s

Subscripts

0	properties of air
c_1	Control element
c_2	Convection
dyn	Dynamic
e	Plate element (element centre point)

i_1	Incident
i_2	General index (plate elements)
m	General index (modes, residual modes)
n	General index (plate elements, dynamic modes)
p	Plate
r	Receiver
rad	Radiation
res	residual
rev	reverberant
s	Source

Mathematical:

X	Real value X
$\tilde{X}$	Complex Value X
$Re\{\tilde{X}\}$	Real part of X
$Im\{\tilde{X}\}$	Imaginary part of X
$\hat{X}$	Peak value X
$\tilde{X}^*$	Conjugant of X
$E\left[\tilde{X}\tilde{X}^*\right]$	Expectation of correlation $\left[\tilde{X}\tilde{X}^*\right]$
$\mathbf{var}\left[X\right]$	variance of X
$\bar{X}$	Time average value of X
$\langle X \rangle$	Space average value of X
X^n	X to the power of n
X'	First spatial derivative of X
X''	Second spatial derivative of X ...
$\dot{X}$	First derivative of X in respect to time
$\ddot{X}$	Second derivative of X in respect to time ...
d	Total differential
∂	Partial differential
$\mathbf{X}$	Matrix X
$\mathbf{X}.\mathbf{X}$	Element by element Matrix multiplication
$\mathbf{X^{-1}}$	Inverse of Matrix X

$\mathbf{X^T}$	Non conjugate transpose of Matrix X
$\mathbf{X^H}$	Complex conjugate transpose (Hermitian transpose) of Matrix X
$\mathbf{I}$	Identity matrix
$\sec(X)$	Secant of X; equals $\frac{1}{cos(X)}$
$J_n(X)$	n^{th} order Bessel function of X
$M_n(X)$	n^{th} order Struve function of X

Chapter 1

Introduction

Environmental and economic considerations increase the demand for weight optimized structural design. This often conflicts with the requirement on sound transmission reduction and vibration isolation performance. In recent years the design of smart panels with active components have therefore been a field of increasing research interest.

Up to now, most studies on smart panels have been restricted to the low frequency range where resonant frequencies are discretely spaced and modal overlap is low. In this frequency region, structural vibration response can be determined using deterministic prediction models.

With increasing frequencies the modal overlap of plate an shell structures is increasing. Deterministic models fail to predict the response accurately. This is partly due to the simplified underlying assumptions made in the models and due to the increasing sensitivity of the response to structural variability. Structural response is therefore often described in terms of statistical models. Mid frequencies are usually defined as the frequency range where mode separation and modal overlap are such that deterministic models start to fail but strict energy methods are not yet applicable.

In practice, this problem is aggravated by the fact that most structures are assembled from elements with different structural properties. Aircraft fuselages for example are constructed from a stiff framework formed by beam-like elements and relatively flexible panels that form the the skin of the fuselage. The boundary conditions in such frameworks are complex and often not well defined, this makes it difficult to predict the structural

response accurately. For many practical vibro-acoustic problems it is also not possible to describe the incident disturbances in a deterministic way. For a range of common forms of excitation approximate solutions are available that describe the disturbances in terms of time and spatial correlation and time and spaced averaged power spectra.

In 2004 Gardonio and Elliott [1] presented a theoretical study comparing the sound transmission through different types of smart panels with applied active feedback control architecture. This work follows the methodology to describe the sound transmission through an rectangular panel proposed by the authors, which uses an elemental approach based on the concept of constant boundary elements [2]. In this report formulations based on these approach are derived to develop a panel model which incorporates:

- Multi input multi output (MIMO) decentralized feedback control loops using collocated point velocity sensors and force actuator pairs.
- Fluid coupling on the source and radiating side of the panel.
- Arbitrary panel boundary conditions by using discrete arrays of bending forces and bending moments that can replicate point stiffness, damping and inertial linear and angular effects.

The excitation of the panel on the source side can either be described in a deterministic sense, by an incident pressure amplitude and geometrical distribution (for example a plane acoustic wave) or in a stochastic sense in terms of the time and spatial averaged incident pressure and the spatial correlation of the excitation.

This report is structured in two principal parts:

- In Chapter 2 the element based model is introduced and subsequently extended to incorporate fluid loading, decentralized velocity feedback control loops and boundary impedances.Formulations for deterministic and stochastic excitation models are discussed.
- In Chapter 3 simulation results of systematic studies on the sound transmission are presented, considering the effect of the control loops spatial distribution, variations in velocity feedback gain, specific fluid loading cases, enforced flexible boundaries and both, deterministic (i.e. acoustic plane wave) and stochastic (i.e. TBL, acoustic diffuse field and rain on the roof) disturbances.

The results from systematic convergence studies for the proposed model are provided in Appendix A. In particular the convergence of the model with reference to number of elements and number of structural modes has been assessed for the case of an acoustic plane wave excitation.

Shorter and Langley [3] present a general method to predict the ensemble average steady-state response of complex vibro-acoustic systems that contain subsystems with uncertain or random properties. It is thought that this framework, in conjunction with the elemental model presented in this report, can be used to model the sound transmission through a panel with uncertain boundary conditions for deterministic and stochastic excitation, at low-mid audio frequencies.

Chapter 2

Modelling sound transmission through a panel

In 1993 Elliott and Johnson [4] published a paper on the prediction of sound radiation from a panel using an elemental approach. In 2004 Gardonio and Elliott [1] presented a theoretical study using this approach to predict and compare the sound transmission through different types of smart panels with active feedback control systems. Following this methodology, this chapter describes an element based modelling approach for the structural vibration of a thin rectangular panel under deterministic excitation.

A more general model will be developed in subsequent steps, incorporating fluid loading, feedback control using discrete idealized point forces, and flexible boundary conditions by means of discrete linear and rotational viscous-elastic effects.

Towards the end of these chapter stochastic excitation models will be introduced. Formulations for considering uncorrelated rain on the roof, acoustic diffuse field [5] and turbulent boundary layer (TBL) [6, 7] disturbances will be discussed.

2.1 The elemental model approach

The elemental approach, considered in this report, referes to the work presented by Elliott and Johnson [4, 8]. The structural response to a deterministic time-harmonic excitation is determined by subdividing the panel into a uniform grid of elements. The time averaged

panel kinetic energy and the time averaged total sound power radiated by the panel is derived in terms of the time averaged element velocities, defined at the element centre positions. Finite modal expansion formulations are used to derive expressions for the point and transfer mobility functions between the elements. Any kind of external disturbance on the panel is expressed by incident point forces on the element centres.

The particular model studied is shown in Figure 2.1; it resembles a thin rectangular aluminium panel mounted in a infinite baffle. The structural and geometrical properties are defined in Table 2.1

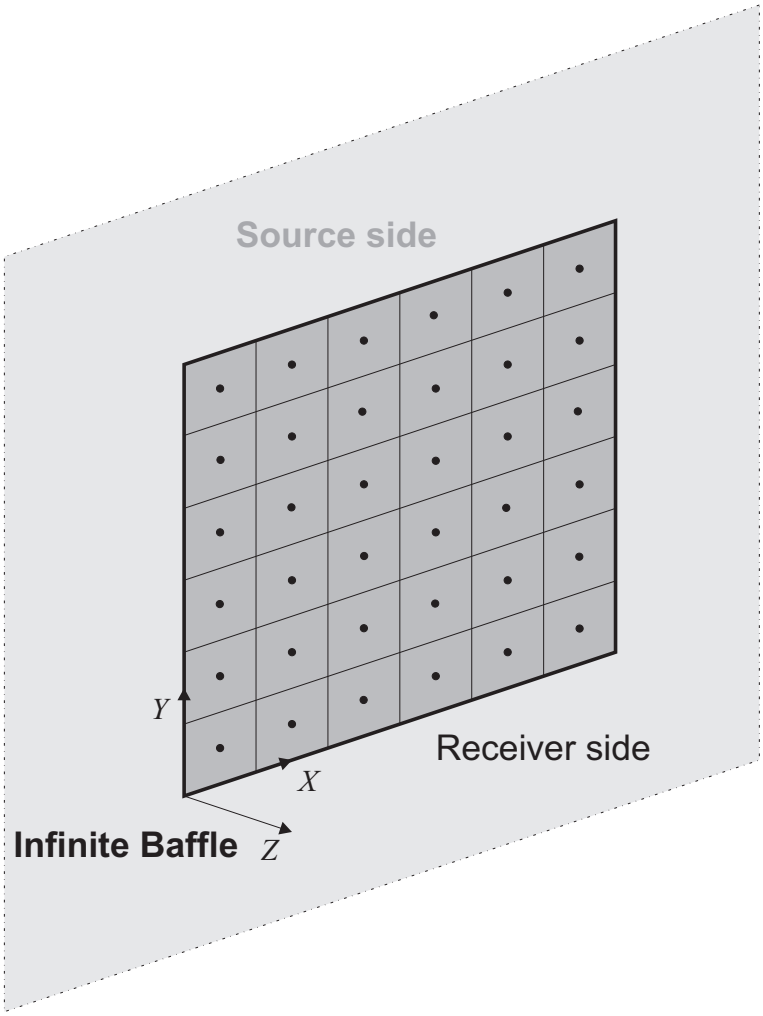

Figure 2.1: Geometrical arrangement considered for the panel model with an paradigmatic subdivision in an uniform grid for elements.

Table 2.1: Geometry and physical constants of the panel

Parameter	Symbol	Value	Unit
x-dimensions	l_x	0.278	m
y-dimensions	l_y	0.247	m
Thickness	h_p	0.001	m
Density	ρ_p	2720	kg m^{-3}
Young's modulus	E_p	7×10^{10}	N m^{-2}
Poisson's ratio	ν_p	0.33	–
Damping ratio	ζ_p	0.01	–
Loss factor	$\eta_p = 2\zeta_p$	0.02	–

2.2 Panel point response to point loads

In this section the finite modal expansion formulations for the response of the panel elements will be developed and cast into matrix formulations that allow a convenient and efficient estimation of the discretised panel response.

The response is derived assuming time-harmonic excitation of the form $Re\{\exp(j\omega t)\}$ where ω is the circular frequency and $j = \sqrt{-1}$. For brevity the time-harmonic term $\exp(j\omega t)$ will be omitted in the formulation which will be given in complex form. Therefore, the time harmonic velocity $\dot{w}(t) = Re\{\dot{\tilde{w}} \exp(j\omega t)\}$ and force $F(t) = Re\{\tilde{F} \exp(j\omega t)\}$ fluctuations will be replaced by the complex velocity and force phasors $\dot{\tilde{w}}$ and $\tilde{F}$ respectively. Throughout the report the superscript $\tilde{}$ will be used to identify complex, frequency dependent functions.

The velocity response of a single panel element $\dot{\tilde{w}}_e(\omega)$ to defined point loads on the panel element centres can be calculated as the sum of the product of elemental mobilities and incident elemental forces;

$$\dot{\tilde{w}}_e(\omega) = \sum_{n=1}^{N_e} \tilde{Y}_{e,n}(\omega)\tilde{F}_{i,n}(\omega), \tag{2.1}$$

where $\tilde{Y}_{e,n}(\omega)$ denotes the point and transfer mobilities between an element e and any other panel element n respectively and $\tilde{F}_{i,n}(\omega)$ is the force incident on each panel element.

The total number of elements N_e is given by the product of the number of elements along

the x and y-axis $N_{ex} \times N_{ey}$. The number of elements along each axis depend on the shortest bending wave length. At least two elements per wave length are needed to describe the panel motion uniquely, i.e. to avoid spatial aliasing. For adequate spatial resolution, usually at least four elements per wavelength are used. In the case of an all side pinned rectangular panel, this criteria corresponds respectively to 1 and 2 elements per highest mode order along the panel axis. A convergence study on the element resolution with reference to the panel total kinetic energy is presented in Appendix A.

In order to accurately model the response of smart panels, the contribution of higher order modes with natural frequencies well beyond the frequency range actually observed must be taken into account. Only in this case near field effects of point control forces can be accurately analysed. This is of specific importance for the prediction of the response with control where the contribution of lower order modes is largely cancelled. Studies on smart panel models [1] showed that a large number of modes with natural frequencies up to 50 times the highest observation frequency are required to describe the response of panels with feedback control forces adequately. Preumont [9] suggested that the point and transfer responses on a structure can be calculated from the sum of dynamic and residual terms

$$\tilde{Y}_{e,n}(\omega) = \frac{j\omega}{m_p} \left(\tilde{G}_{dyn,e,n}(\omega) + \tilde{G}_{res,e,n} \right), \tag{2.2}$$

where $\tilde{G}_{dyn,e,n}(\omega)$ and $\tilde{G}_{res,e,n}(\omega)$ are the mass normalized dynamic and residual point / transfer receptances and m_p is the total mass of the panel. The introduction of receptance terms allows to take the $\frac{j\omega}{m_p}$ term out of the modal expansions. The expansion formulation for the dynamic receptance matrix is given by

$$\tilde{G}_{dyn,e,n}(\omega) = \sum_{m=1}^{M_{dyn}} \frac{\psi_m(x_e, y_e)\, \psi_m(x_n, y_n)}{\omega_m^2 (1 + j\eta_p) - \omega^2}, \tag{2.3}$$

where $\psi_m(x_n, y_n)$ are the modeshapes of the panel at position n and mode m, and M_{dyn} is the total number of dynamic modes considered. The dynamic receptance is a function of the observation frequency ω, it is therefore calculated for the entire range of discrete observation frequencies. Hence the computational effort is increasing with the number of

observation frequencies and also with the number of considered dynamic modes.

For modes with natural frequencies well above the highest observation frequency only the stiffness and damping terms are of importance for the response of the panel, the mass terms can be neglected. A separation of the modal range in dynamic and residual mode regions can increase the computational efficiency. In fact the the modal expansion formulation for the residual receptance matrix is given by

$$\tilde{G}_{res,e,n} = \sum_{m=M_{dyn}+1}^{M_{res}} \frac{\psi_m\left(x_e, y_e\right)\psi_m\left(x_n, y_n\right)}{\omega_m^2\left(1 + j\eta_p\right)}. \tag{2.4}$$

Since the term under the sum in the residual acceptance term $\tilde{G}_{e,n,res}$ is independent of the excitation frequency, it only needs to be computed once for each element, which can reduce the computational effort significantly.

For convenience the formulations for the velocity response of single elements in Equation (2.1) can be cast into a vector matrix expression to yield

$$\dot{\tilde{\mathbf{w}}}_e(\omega) = \tilde{\mathbf{Y}}_{ee}(\omega)\tilde{\mathbf{F}}_{i,e}(\omega), \tag{2.5}$$

where $\dot{\tilde{\mathbf{w}}}_e(\omega)$ is a $[N_e, 1]$ dimensional vector containing the velocities of the single panel elements,

$$\dot{\tilde{\mathbf{w}}}_e(\omega) = \left\{ \begin{array}{c} \dot{\tilde{w}}_{e,1}(\omega) \\ \dot{\tilde{w}}_{e,2}(\omega) \\ \vdots \\ \dot{\tilde{w}}_{e,N_e}(\omega) \end{array} \right\} \tag{2.6}$$

and $\tilde{\mathbf{F}}_{i,e}(\omega)$ is the $[N_e, 1]$ dimensional vector of the external excitation force incident on the elements. The $[N_e, N_e]$ dimensional mobility matrix $\tilde{\mathbf{Y}}_{ee}(\omega)$ contains the point and transfer mobilities for all elements where the main diagonal contains the element point mobilities. In analogy to Equation (2.2) the mobility matrix is calculated as the sum of the $[N_e, N_e]$ dimensional dynamic and the residual element acceptance matrices

$$\tilde{\mathbf{Y}}_{ee}(\omega) = \frac{j\omega}{m_p}\left(\tilde{\mathbf{G}}_{ee,dyn}(\omega) + \tilde{\mathbf{G}}_{ee,res}\right). \tag{2.7}$$

Considering Equation (2.3), the dynamic acceptance matrix is calculated from the diagonal frequency dependent dynamic matrix $\tilde{\mathbf{\Omega}}_{dyn}(\omega)$ and the fully populated frequency independent $\mathbf{\Psi}_{e,dyn}$ matrix of the dynamic mode shapes at the element centre positions;

$$\tilde{\mathbf{G}}_{ee,dyn}(\omega) = \mathbf{\Psi}_{e,dyn}\tilde{\mathbf{\Omega}}_{dyn}(\omega)\mathbf{\Psi}^T_{e,dyn}. \tag{2.8}$$

The diagonal dynamic matrix $\tilde{\mathbf{\Omega}}_{dyn}(\omega)$ is assembled from

$$\tilde{\Omega}_{dyn_{m,m}}(\omega) = \frac{1}{\omega_m^2\left(1 + j\eta_p\right) - \omega^2}, \tag{2.9}$$

where the mode index m ranges from $m = 1$ to the maximum number of dynamic modes $m = M_{dyn}$. Therefore $\tilde{\mathbf{\Omega}}_{dyn}(\omega)$ is a square diagonal matrix with dimensions $[M_{dyn}, M_{dyn}]$. The mode shape matrix $\mathbf{\Psi}_{e,dyn}$ is assembled from

$$\Psi_{e,dyn_{n,m}} = \psi_m\left(x_n, y_n\right), \tag{2.10}$$

where the mode index m ranges from $m = 1$ to the maximum number of dynamic modes $m = M_{dyn}$ and the element index n ranges from $n = 1$ to $n = N_e$ to yield $\mathbf{\Psi}_{e,dyn}$ as a $[N_e, M_{dyn}]$ dimensional matrix. The residual receptance matrix $\tilde{\mathbf{G}}_{ee,res}$ is accordingly calculated from the diagonal frequency independent residual matrix $\tilde{\mathbf{\Omega}}_{res}$ and the fully populated residual mode shape matrix $\mathbf{\Psi}_{e,res}$

$$\tilde{\mathbf{G}}_{ee,res} = \mathbf{\Psi}_{e,res}\tilde{\mathbf{\Omega}}_{res}\mathbf{\Psi}^T_{e,res}, \tag{2.11}$$

where the residual matrix $\tilde{\mathbf{\Omega}}_{res}$ is assembled from

$$\tilde{\Omega}_{res_{m,m}} = \frac{1}{\omega_m^2\left(1 + j\eta_p\right)}. \tag{2.12}$$

Here the mode index m ranges from $m = (M_{dyn} + 1)$ to the maximum number of consid-

ered residual modes $m = M_{res}$. Therefore $\tilde{\mathbf{\Omega}}_{res}$ is a square $[(M_{res} - M_{dyn}), (M_{res} - M_{dyn})]$ dimensional, diagonal matrix. The modeshape matrix $\mathbf{\Psi}_{e,res}$ is assembled from

$$\Psi_{e,res_{n,m}} = \psi_m (x_n, y_n), \tag{2.13}$$

where the mode index m ranges from $m = (M_{dyn} + 1)$ to the maximum number of considered residual modes $m = M_{res}$ and the element index n ranges from $n = 1$ to $n = N_e$ to yield $\mathbf{\Psi}_{e,res}$ as a $[N_e, (M_{res} - M_{dyn})]$ dimensional matrix.

Note that $\tilde{\mathbf{\Omega}}_{dyn}(\omega)$ and $\tilde{\mathbf{\Omega}}_{res}$ are both square diagonal matrices. In practice there are computational benefits to generate a fully populated $[M, N_e]$ dimensional matrix $\tilde{\mathbf{\Phi}}$, replicating the diagonal of the $\tilde{\mathbf{\Omega}}$ matrices in each column and performing an element by element multiplication so that

$$\tilde{\mathbf{G}}_{ee} = \mathbf{\Psi}_e \left(\tilde{\mathbf{\Phi}} . \mathbf{\Psi}_e^T \right), \tag{2.14}$$

where . represents the MatLab element by element multiplication between matrices. In this way a large number of multiplications by the zeros in the diagonal $\tilde{\mathbf{\Omega}}$ matrices can be avoided.

The discussed element based response model is not strictly restricted to thin rectangular plates, yet it depends on the availability of solutions for the natural frequency and modeshapes of the structure. In this study the dynamic behaviour of the panel is described using thin plate theory. The formulations for the modal behaviour of thin rectangular plates are taken from references [10, 11]. The particular formulations used in this study are given in Appendix B. One should note that only the all side pinned boundary condition yields simple closed form analytic solution. The natural frequency and natural modes expressions by Warburton [11] are derived using the Rayleigh method and assume waveforms similar to those of beams. Limitations and uncertainties due to these approximated formulations will be discussed later in this report.

2.3 Deterministic excitation

This section uses the element based model introduced in Section 2.2 to predict the response of a panel to a deterministic distributed disturbance. As for the model problem discussed in reference [1], the example of an acoustic plane wave is considered. Formulations for the kinetic energy and total radiated sound power of the panel are developed and cast in element matrices that fit in with the elemental panel response formulations discussed above.

2.3.1 Plane wave excitation

As an example of deterministic disturbance, an acoustic plane wave excitation is considered here. The wave is defined by its sound pressure complex amplitude which depends on the angles of incidence θ, measured from the normal of the panel surface; and the angle φ in the x, y-plane, measured from the x-axis.

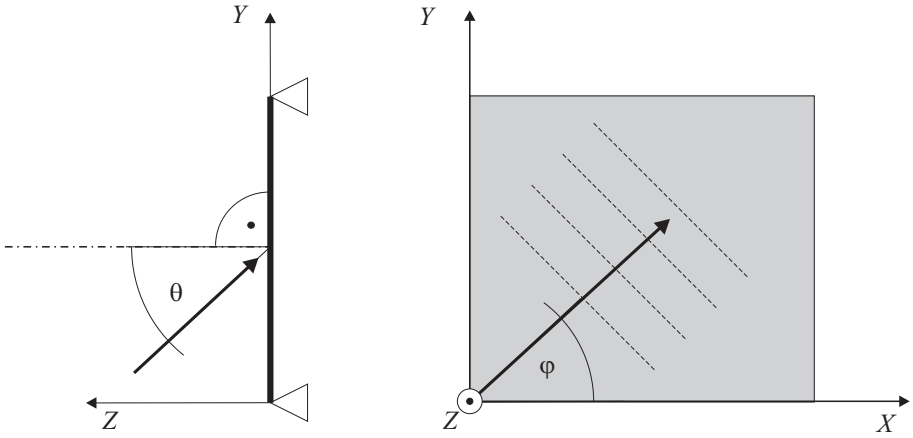

Figure 2.2: Angle of incidence for acoustic plane wave

Assuming time harmonic pressure fluctuation, the incident sound pressure $p_i(x, y, t)$ acting on the source side of the panel is given as

$$p_i(x, y, t) = Re\{\hat{p}_i(\omega)e^{j(\omega t - k_x x - k_y y)}\}, \tag{2.15}$$

where $\hat{p}_i(\omega)$ is the pressure amplitude of the incident wave. The wavenumbers in x and y directions, k_x and k_y, are given by

$$k_x(\omega) = k_0(\omega) \sin\theta \cos\varphi, \tag{2.16}$$

$$k_y(\omega) = k_0(\omega) \sin\theta \sin\varphi, \tag{2.17}$$

where $k_0(\omega) = \frac{\omega}{c_0}$ is the wavenumber of sound in the surrounding fluid. The fluid properties of air and the pressure amplitude $\hat{p}_i(\omega)$ and the angles of incidence θ and φ of the acoustic wave as used within this study are listed in Table 2.2 and Table 2.3 below.

Table 2.2: Acoustical parameters for air

Parameter	Symbol	Value	Unit
Speed of sound	c_0	343	m/s
Density	ρ_0	1.21	kg/m^3
Specific impedance	$Z_0 = c_0\rho_0$	415	Ns/m^3

Table 2.3: Physical and geometrical parameters of the incident plane wave

Parameter	Symbol	Value	Unit
Wave amplitude	$\hat{p}_i$	1	N/m^2
Angle of incidence	ϕ	45	DEG
Angel of incidence	θ	45	DEG

In order to calculate the excitation due to a plane wave, the panel is subdivided into an appropriate number of equally spaced and sized elements. The investigations of the numerical convergence of the model (Appendix A) show that below the critical frequency, where the acoustic wave length is longer than the bending wave length, 4 elements per shortest bending wave length are adequate to produce sufficiently accurate results. Above the critical frequency, where the acoustic wave length is shorter than the bending wave length, at least 4 elements per acoustic wave length are considered. The number of elements along the x and y-axis, N_{ex} and N_{ey} are therefore given as

$$\begin{aligned} N_{ex} &\geq 4 \times \tfrac{l_x}{\lambda_{min}} \\ N_{ey} &\geq 4 \times \tfrac{l_y}{\lambda_{min}} \end{aligned}, \tag{2.18}$$

where the factor of 4 represents the chosen number of elements per wavelength. One might increase this factor if a higher precision is required, it should however be con-

sidered that an increase of the spatial resolution will increase the computational costs considerably.

For an all side pinned rectangular panel a spatial resolution of 4 elements per bending wavelength corresponds to 2 elements per highest modal order $n_{x,max}$ and $n_{y,max}$ along the x and y dimension that fall within the observed frequency range.

The excitation force incident on each panel element $\tilde{F}_{i,e}(\omega)$ is approximated as a point force acting on the element centres

$$\tilde{F}_{i,e}(\omega) = A_e(1+r)\hat{p}_i(\omega)e^{-j(k_x x_e + k_y y_e)}, \tag{2.19}$$

where A_e is the area of a single panel element and r is the wave reflection coefficient. Within this study we assume that the plate impedance of each panel element per unit area $\tilde{Z}_e/A_e$ is much higher than the specific impedance of air Z_0 so that the wave is reflected outright and thus $r = 1$. This results in a pressure doubling on the panel surface [12].

After calculating the incident forces for all panel elements and casting them into a $[N_e, 1]$ dimensional vector $\tilde{\mathbf{F}}_{i,e}(\omega)$, Equation (2.5) can be applied to derive the resulting element velocity response of the panel.

2.3.2 Energy and power terms

Having derived formulations for the velocity response and the incident forces it is now possible to predict the resulting kinetic energy of the panel and the total radiated far field sound power.

Kinetic energy

In general terms, for harmonic excitations, the time-averaged kinetic energy of a thin rectangular panel is given by integral of the squared magnitude of the surface velocity over the panel dimensions in x and y directions, times the panel surface density [12]

$$E(\omega) = \frac{\rho_{s,p}}{4} \int_0^{l_x} \int_0^{l_y} \left|\dot{\tilde{w}}(x,y,\omega)\right|^2 dxdy. \tag{2.20}$$

where a factor of 1/2 is due to the integration and an additional factor 1/2 arises from the conversion from peak to rms values.

In the elemental approach the surface integral in Equation (2.24) is substituted by a sum over the element velocities [12]. Utilizing matrix algebra this summation can be calculated from the inner hermitian product of the element velocity vector. This yields the total kinetic energy as [12]

$$E(\omega) = \frac{m_e}{4} \dot{\underline{\mathbf{w}}}_e^H(\omega)\dot{\underline{\mathbf{w}}}_e(\omega), \tag{2.21}$$

where ^{H} denotes the hermitian transpose and m_e is the mass of a single panel element. Figure 2.3 shows the spectrum of the kinetic energy normalized to the pressure amplitude of a plane acoustic wave incident at an angle $\theta = 45°$ and $\varphi = 45°$ in the frequency range between 50 Hz and 5 kHz. At low frequencies, below 500 Hz, the response of the panel is characterized by well separated resonances which are controlled by low order resonant modes. With increasing frequency, modal overlap [13] constantly rises and thus, above 500 Hz the response is increasingly controlled by clusters of modes. Figure 2.3 clearly highlights that for frequencies above the first resonance, the response of the panel is mass controlled.

The modal overlap factor M is defined as the ratio between the half-power bandwidth and the average natural frequency spacing and is given as [13]

$$M(f) = f\eta_p n \tag{2.22}$$

where f is the frequency in Hz, η_p is the material loss factor and $n(f)$ is the modal density in Hz^{-1}. The statistical mean modal density for a simply supported panel can be approximated as [13]

$$n(f) = \frac{A_p}{2}\sqrt{\frac{\rho_{s,p}}{D_p}} \tag{2.23}$$

where A_p is the panel surface area, $\rho_{s,p}$ is the panel mass per unit area and D_p is the bending stiffness. In the case of a thin panel $n(f)$ is constant. Figure 2.4 shows the

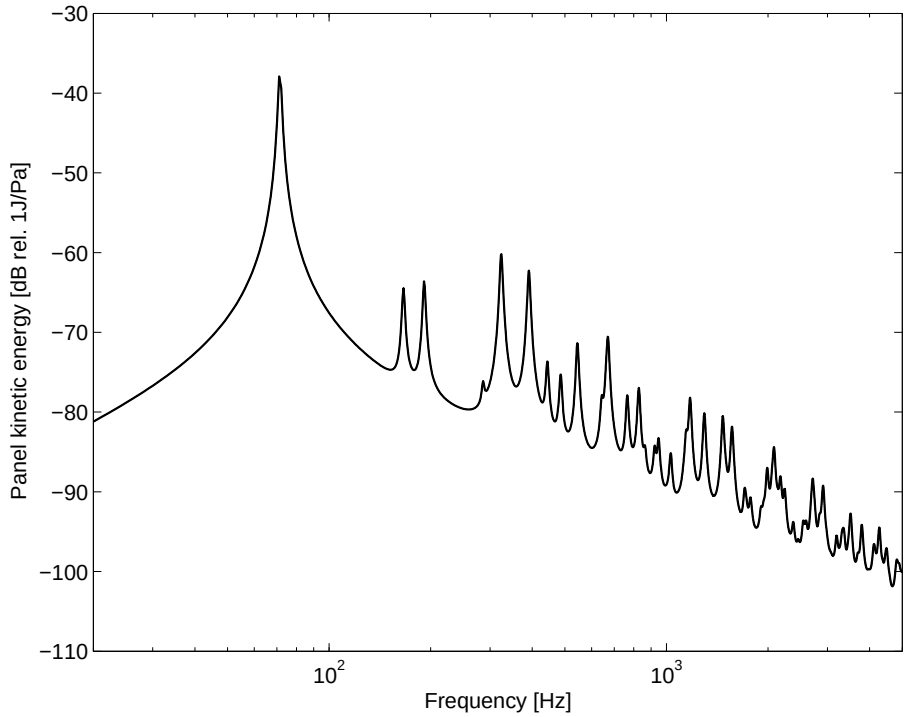

Figure 2.3: Total panel kinetic energy normalized to the pressure amplitude of a plane wave incident at an angle $\theta = 45°$ and angle $\varphi = 45°$ of the plate without control.

estimated modal overlap factor for the panel as specified in Table 2.1. For modal overlap factors larger than 1 the response spectrum is assumed to be damping controlled; for the panel investigated the modal overlap exceeds 1 for frequencies higher than 2250 Hz.

Sound radiation

The time averaged total sound power radiated to one side of a thin rectangular panel is given by the integral of the real part of the complex conjugate product of surface velocity and acoustical pressure, over the panel dimensions in x and y [12]

$$P_{rad}(\omega) = \frac{1}{2} \int_0^{l_x} \int_0^{l_y} Re \left\{ \dot{\tilde{w}}(x, y, \omega)^* p(x, y, \omega) \right\} dxdy. \tag{2.24}$$

where $*$ denotes the complex conjugate and the factor 1/2 arises from the conversion from peak to rms values. Considering radiation into free space, for an ideally planar panel, the Rayleigh integral [12] can be used to rewrite the acoustic pressure on the surface in terms of the surface velocities. Utilizing matrix algebra Equation (2.24) can be approximated as [12]

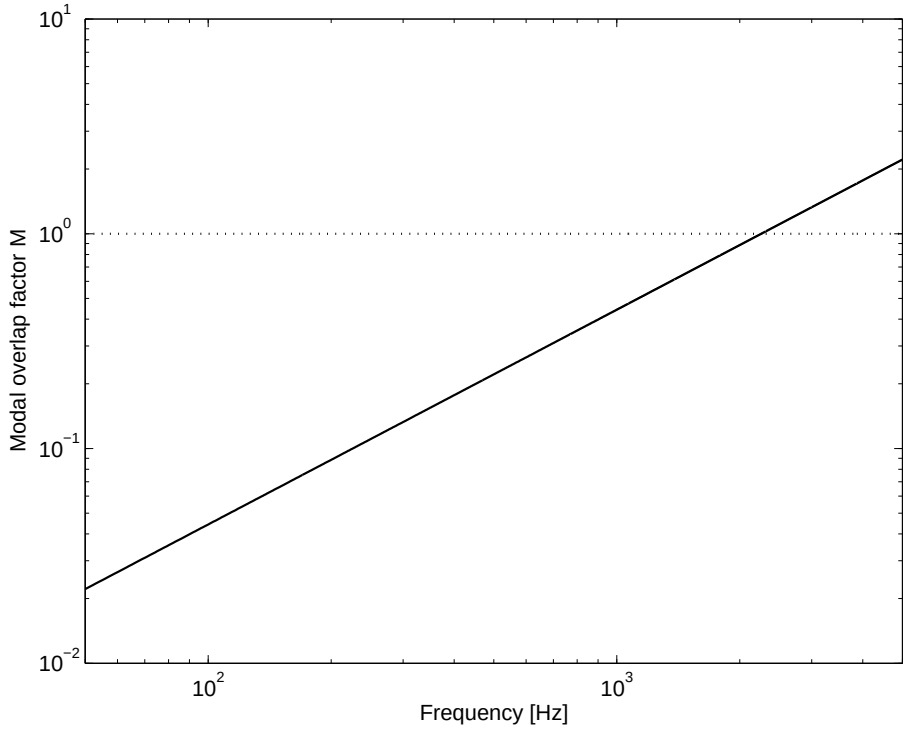

Figure 2.4: Statistical mean modal overlap factor for the aluminum panel specified in Table 2.1

$$P_{rad}(\omega) = \frac{1}{2} Re \left\{ \dot{\tilde{\mathbf{w}}}_e^H(\omega) \tilde{\mathbf{Z}}_{rad}(\omega) \dot{\tilde{\mathbf{w}}}_e(\omega) \right\}, \tag{2.25}$$

where $\tilde{\mathbf{Z}}_{rad}(\omega)$ is the radiation impedance matrix, containing the acoustical point and transfer impedances in front of all panel elements. For convenience and computational efficiency Equation (2.25) can be rewritten as [12]

$$P_{rad}(\omega) = \dot{\tilde{\mathbf{w}}}_e^H(\omega) \mathbf{R}_{rad}(\omega) \dot{\tilde{\mathbf{w}}}_e(\omega), \tag{2.26}$$

where $\mathbf{R}_{rad}(\omega)$ is the $[N_e, N_e]$ dimensional radiation matrix defined as the real part of the radiation impedance divided by two

$$\mathbf{R}_{rad}(\omega) = \frac{1}{2} Re \left\{ \tilde{\mathbf{Z}}_{rad}(\omega) \right\}. \tag{2.27}$$

According to [12] the radiation impedance between two small planar elements in a plane can be approximated as

$$\tilde{Z}_{rad,s,r} = \frac{j\omega\rho_0 A_e^2}{2\pi r_{s,r}} e^{-jk_0 r_{s,r}}; \tag{2.28}$$

substituting $k_0 = \frac{\omega}{c_0}$, the real part of $\tilde{Z}_{rad,s,r}$ between source and receiver element is found as

$$Re\left\{\tilde{Z}_{rad,s,r}\right\} = \frac{\omega^2\rho_0 A_e^2}{2\pi c_0} \quad \frac{\sin k_0 r_{s,r}}{k_0 r_{s,r}}. \tag{2.29}$$

For the real part of the point radiation impedance $Re\left\{\tilde{Z}_{rad,i,i}\right\}$ the distance $r_{i,i}$ is zero, the second term in Equation (2.29) is therefore undefined. Using L' Hôpital's rule [14] it is found

$$\lim_{r\to 0} \frac{\sin(k_0 r)}{k_0 r} = \lim_{r\to 0} \frac{k_0 \cos(k_0 r)}{k_0} = 1. \tag{2.30}$$

The radiation coefficient matrix $\mathbf{R}_{rad}(\omega)$ therefore takes the form:

$$\mathbf{R}_{rad}(\omega) = \frac{\omega^2\rho_0 A_e^2}{4\pi c_0} \begin{bmatrix} 1 & \frac{\sin(k_0 r_{1,2})}{k_0 r_{1,2}} & \cdots & \frac{\sin\left(k_0 r_{1,N_e}\right)}{k_0 r_{1,N_{ep}}} \\ \frac{\sin(k_0 r_{2,1})}{k_0 r_{2,1}} & 1 & \ddots & \vdots \\ \vdots & \ddots & \ddots & \vdots \\ \frac{\sin\left(k_0 r_{N_e,1}\right)}{k_0 r_{N_e,1}} & \cdots & \cdots & 1 \end{bmatrix} \tag{2.31}$$

Figure 2.5 shows the spectrum of the total radiated sound power for plane acoustic wave incident at an angle $\theta = 45°$ and angle $\varphi = 45°$, normalized to an acoustic pressure amplitude of one Pascal. As for Figure 2.3 the spectrum is dominated by the frequency response of the principal panel mode. Resonances of low efficiency radiation modes (even symmetric panel modes) are barely visible.

Sound transmission

Fahy and Gardonio [12] define the sound transmission coefficient τ as the ratio between the radiated sound power in the free, far field of the radiating side of the panel P_{rad} and the sound power of the incident plane wave on the source side of the panel P_i.

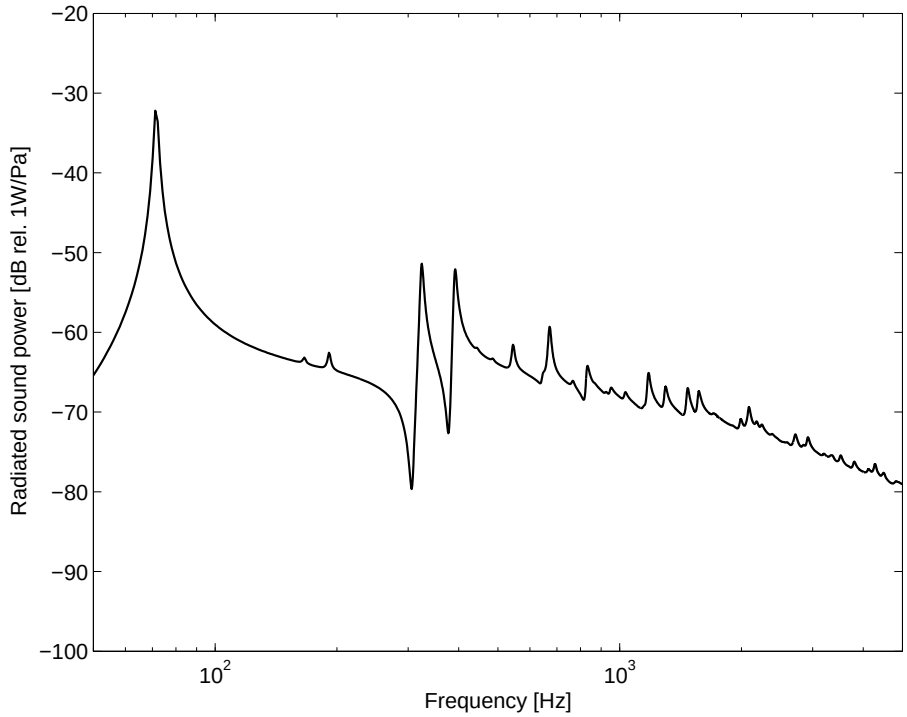

Figure 2.5: Radiated sound power normalized to the pressure amplitude of an acoustic plane wave incident at an angle $\theta = 45°$ and angle $\varphi = 45°$ of the plate without control.

$$\tau(\omega) = \frac{P_{rad}(\omega)}{P_i(\omega)}. \tag{2.32}$$

Note that the definition of the transmission coefficient τ considers the sole power of an infinitely extended incident plane wave P_i and not the total power on the source side of the panel; which is determined by the interaction of the incident, reflected and back radiated sound pressure waves over the area f the panel. The power of the incident acoustic plane wave can be calculated from [12]

$$P_i(\omega) = \hat{p}_i(\omega)^2 \frac{A_e \cos(\theta)}{2\rho_0 c_0}. \tag{2.33}$$

As for most acoustical quantities it is convenient to express the transmission coefficient τ in logarithmic terms

$$T(\omega) = 10 \log_{10} (\tau(\omega)). \tag{2.34}$$

The Sound transmission loss or sound reduction index in decibel is calculated from the

reciprocal of the transmission coefficient and is expressed as follows:

$$R(\omega) = 10 \log_{10} \left(\frac{1}{\tau(\omega)} \right). \tag{2.35}$$

Approximated solutions for the sound transmission coefficients are widely discussed in the literature. In [15] Fahy discusses an approximate formulation that allows to evaluate the transmission coefficient for thin panels for plane wave excitations depending on the out of plane incidence angle θ [15] page 284

$$\tau(\theta) = \frac{\left(\frac{2Z_0}{\omega \rho_s} \right)^2 \sec^2(\theta)}{\left[\left(\frac{2Z_0}{\omega \rho_s} \right) \sec^2(\theta) + \eta \left(\frac{k_0}{k_B} \right)^4 \sin^4(\theta) \right]^2 + \left[1 - \left(\frac{k_0}{k_B} \right)^4 \sin^4(\theta) \right]^2}. \tag{2.36}$$

Fahy [16] gives an approximation for the sound transmission coefficient through a thin unbounded panel mounted upon a viscously damped elastic suspension. This is a first order approximation for the fundamental mode of a large finite panel. The formulation is derived for an acoustic plane wave excitation normal to the surface ($\theta = 0$). For non identical media on both sides of the panel, the transmission coefficient $\tau(0)$ is given as [16] page 146.

$$\tau(0) = \frac{4n}{\left[\frac{\omega \rho_s - \frac{s}{\omega}}{Z_2} \right]^2 + \left(\frac{\omega_{1,1} \rho_s \eta}{Z_2} + n + 1 \right)^2}, \tag{2.37}$$

where n is the ratio between the specific impedance of the fluid on the source side Z_1 and the specific impedance of the fluid on the receiving side of the panel Z_2 so that $n = Z_1/Z_2 = \rho_1 c_1 / \rho_2 c_2$ and s is the stiffness per unit area at the fundamental panel bending mode given by $s = \rho_s \omega_{1,1}^2$.

In the case that the fluid on both sides of the panel is air, the sound transmission coefficient well above the first natural frequency $\omega_{1,1}$ can be approximated as [16]

$$\tau(0) = \left(\frac{2Z_0}{\omega \rho_s} \right)^2. \tag{2.38}$$

This states that the transmission coefficient is dropping by 6 dB per frequency doubling

i.e. 20 dB per decade and is known as the 'mass law'.

Figure 2.6 and 2.7 show the predicted sound transmission loss using the elemental approach and the approximated solutions from Equation (2.36) and (2.37). Figure 2.6 shows the results for an acoustic plane wave incident at an angle $\theta = 45°$ and $\varphi = 45°$. At low frequencies up to 1kHz the modal response dominates the results for the transmission coefficient and the agreement between elemental approach and the analytical approximations is poor. Above 1 kHz the results form the elemental approach and the results for $\tau(\theta)$ from Equation (2.36) converge asymptotically.

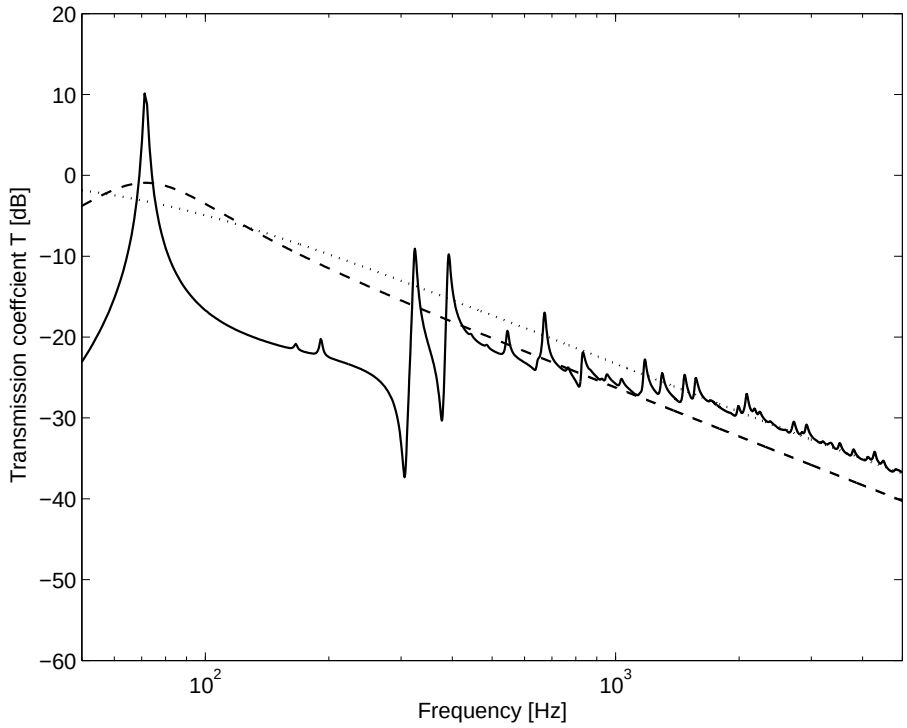

Figure 2.6: Transmission coefficient of the panel excited by an acoustic plane wave incident at an angle $\theta = 45°$ and $\varphi = 45°$. Elemental approach ($solid$), approximated result $\tau(\theta)$ ($dotted$) and $\tau(0)$ ($dashed$).

Figure 2.7 shows the results for an acoustic plane wave incident at an angle $\theta = 0°$ (normal to the panel). At low frequencies up to 800 Hz the modal response dominates the results for the transmission coefficient and the agreement between elemental approach and the analytical approximations is poor. Above 800 Hz the results form the elemental approach and both, the results for $\tau(\theta)$ from Equation (2.36) and $\tau(0)$ from Equation (2.37) converge asymptotically. For the excitation via a perfectly perpendicular plane wave front the contributions of symmetric panel modes cancel entirely so that the corresponding resonances are not at all visible in the predicted sound transmission coefficient.

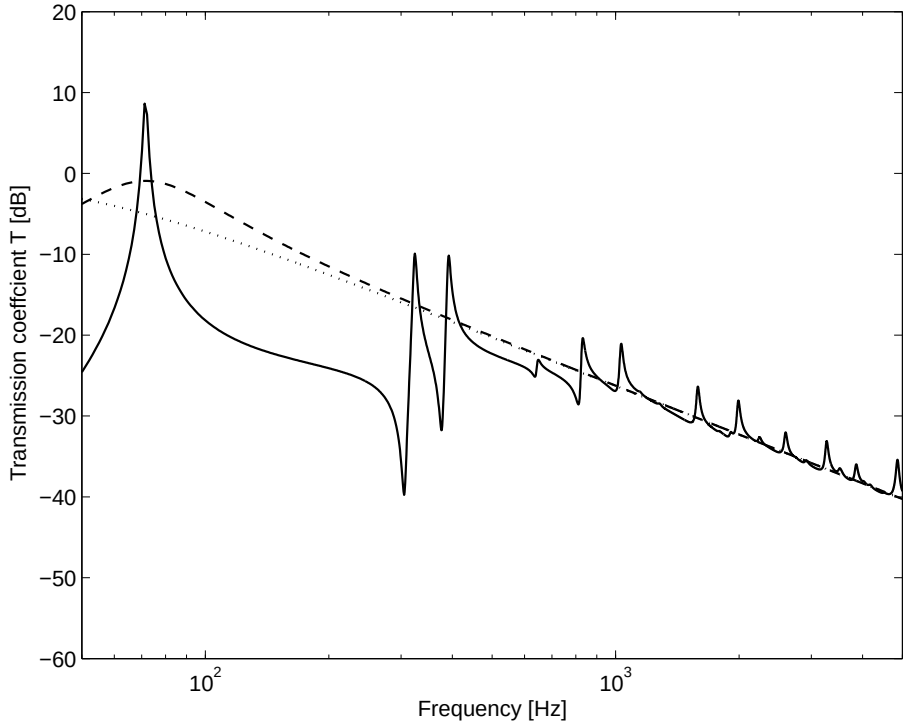

Figure 2.7: Transmission coefficient of the panel excited by an acoustic plane wave incident at an angle $\theta = 0°$ and $\varphi = 0°$. Elemental approach ($solid$), approximated result $\tau(\theta)$ ($dotted$) and $\tau(0)$ ($dashed$).

The two paradigmatic cases considered above, show that the elemental approach reliably converges towards the correct result at higher frequencies. It is interesting to note that for a plane wave normal to the panel only the odd modes are actually radiating sound. At the fundamental natural frequency of the panel the elemental approach predicts transmission coefficients higher than zero dB, i.e. larger than one. This is thought to be possible due to the definition of the transmission coefficient as the ratio between the power of the incident acoustic plane wave and the real part of the radiated sound power on the receiving side (far field radiation).

This definition does not account for the effective sound power incident upon of the panel, which is determined by the effective acoustic field over the surface of the panel due to the incident, reflected and blocked radiated acoustic waves and also neglects any interaction between the acoustic near fields on the source and receiving side of the panel.

It seems therefore be possible that by this definition the sound transmission coefficient could exceed 0 dB for lightly damped structural resonance frequencies, especially at the fundamental bending mode of the panel, where the volumetric response of the panel might cause considerable complex fluid reaction forces.

2.4 Fluid loaded panel model

So far the response of the panel has been considered independent from the fluid loading of the surrounding media. This seems to be a reasonable assumption if the surrounding media is air, i.e if the specific impedance of the surrounding fluid is low compared to the structural impedance per unit area. For fluids with higher specific impedance, such as for example water, this assumption breaks down.

Within this section the element matrix formulations will be extended to incorporate the effect of fluid loading on the source and the receiving sides of the panel in terms of forces acting back from the fluid. Therefore a radiation force $\tilde{\mathbf{F}}_{rad}$ term is added to Equation (2.5)

$$\dot{\tilde{\mathbf{w}}}_e = \tilde{\mathbf{Y}}_{ee}\tilde{\mathbf{F}}_{i,e} + \tilde{\mathbf{Y}}_{ee}\tilde{\mathbf{F}}_{rad}, \tag{2.39}$$

where the $[N_e, 1]$ dimensional radiation force vector $\tilde{\mathbf{F}}_{rad}$ is given by the product of the radiation pressure $\tilde{\mathbf{p}}_{rad}$ on source and receiving side of each panel element and the element surface area A_e,

$$\tilde{\mathbf{F}}_{rad} = -A_e \left(\tilde{\mathbf{p}}_{rad,s} + \tilde{\mathbf{p}}_{rad,r}\right) = -\left(\tilde{\mathbf{Z}}_{rad,s} + \tilde{\mathbf{Z}}_{rad,r}\right) \dot{\tilde{\mathbf{w}}}_e. \tag{2.40}$$

The element radiation pressures can be expressed as the product of the radiation impedance matrices $\tilde{\mathbf{Z}}_{rad}$ and the complex element velocity vector $\dot{\tilde{\mathbf{w}}}_e$. Equation (2.39) can therefore be written as

$$\dot{\tilde{\mathbf{w}}}_e = \tilde{\mathbf{Y}}_{ee}\tilde{\mathbf{F}}_{i,e} - \tilde{\mathbf{Y}}_{ee}\left(\tilde{\mathbf{Z}}_{rad,s} + \tilde{\mathbf{Z}}_{rad,r}\right) \dot{\tilde{\mathbf{w}}}_e. \tag{2.41}$$

Therefore the fluid loading effect can be seen as an acoustic feedback effect, which can be modelled by the block diagram shown in Figure 2.8. An explicit formulation for $\dot{\tilde{\mathbf{w}}}_e$ is subsequently derived as

$$\tilde{\dot{\mathbf{w}}}_e = \underbrace{\left[\left(\mathbf{I}_e + \tilde{\mathbf{Y}}_{ee}\left(\tilde{\mathbf{Z}}_{rad,s} + \tilde{\mathbf{Z}}_{rad,r}\right)\right)^{-1}\tilde{\mathbf{Y}}_{ee}\right]}_{\tilde{\mathbb{Y}}_{ee}}\tilde{\mathbf{F}}_{i,e}, \tag{2.42}$$

where the term within square brackets represents the resulting panel element mobility matrix $\tilde{\mathbb{Y}}_{ee}$, including loading from the surrounding fluid.

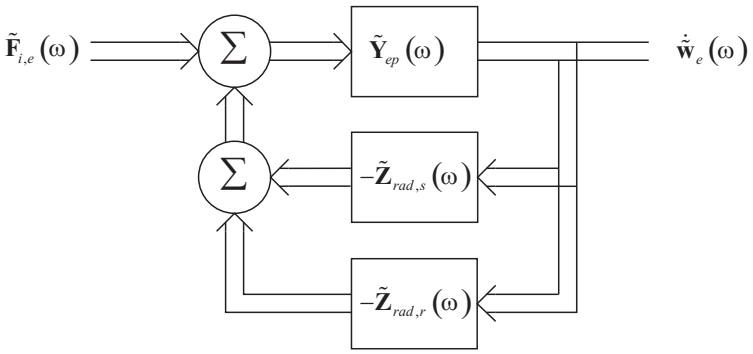

Figure 2.8: Block diagram for a passive fluid loaded panel model.

Approximation for self radiation terms

In section 2.3.2 the real part of the radiation impedance $Re\{\tilde{Z}_{rad}\}$, i.e. the radiation resistance, has been used to calculate the total radiated sound power P_{rad} of the panel. The real part of the element self radiation impedance $Re\{\tilde{Z}_{rad,i,i}\}$ has been determined using Hôpital's rule on the acoustic transfer impedance between two elements in the limit that the distance $r_{s,r}$ goes to zero. To determine radiation forces on the panel elements, the complex point radiation impedance $\tilde{Z}_{rad,i,i}$ needs to be derived. According to Fahy and Gardonio [12] the radiation impedance of a planar surface can be expressed in terms of the following double surface integral

$$\tilde{Z}_{rad} = \frac{j\omega\rho_0}{2\pi}\int_{A_s}\int_{A_r}\frac{e^{-jk_0 r}}{r}dA_s dA_r. \tag{2.43}$$

For the calculations within this study the 'point' radiation impedance of the panel elements was approximated as the radiation impedance of a circular piston of equal surface area, i.e. a piston of diameter $d = 2\sqrt{\frac{A_e}{\pi}}$. Full details about the evaluation of the double integral in Equation (2.43) for a circular piston are given by Pierce [17], the results

are expressed as the sum of the real radiation resistance R_{rad} and the imaginary radiation reactance $\tilde{X}_{rad}$

$$\tilde{Z}_{rad} = \rho_0 c_0 A_e (R_{rad} + jX_{rad}), \tag{2.44}$$

where A_e denotes the element surface and $\rho_0 c_0$ denotes the specific impedance of the fluid. Note that the sign of the imaginary part of the Radiation impedance depends on the definition of the time dependance of the harmonic motion. Within this report the time dependency has been defined as $e^{j\omega t}$.

In the case of a circular piston the solutions for the radiation reactance and resistance are found in terms of first order Bessel and Struve functions [17]. Algorithms that allow an accurate estimation of first order Bessel and Struve functions in MATLAB are available [18]. However in the limits of small arguments, simple first order approximations can be found in terms of a taylor expansion [17]. Obmitting all but the first terms in the series after leads to a simple first or approximation of the form

$$\tilde{Z}_{rad,i,i}(\omega) = \frac{\omega^2 \rho_0 A_e^2}{2\pi c_0} \left[1 + j \frac{16 c_0}{3\omega\sqrt{\pi A_e}} \right]. \tag{2.45}$$

where the real resistance term is identical to that used in the expressions for the radiation matrix in Equation (2.29) to (2.31). More details on the derivation of the radiation impedance of a circular piston [17, 19] and the difference to the formulations for a rectangular piston [19] is given in Appendix C.

2.5 Panel model with feedback control loops

Within this section the formulations for decentralized multi input multi output (MIMIO) feedback loops with idealized feedback forces and point velocity sensors, as shown in Figure 2.9, are discussed. The formulations are casted in the framework of element matrix expressions as introduced in previous sections. The feedback loops discussed are unconditionally stable if perfectly collocated feedback force and velocity sensor pairs are considered. Limitations and instability issues arise for real practical sensor-actuator pairs.

These are not discussed further in this report.

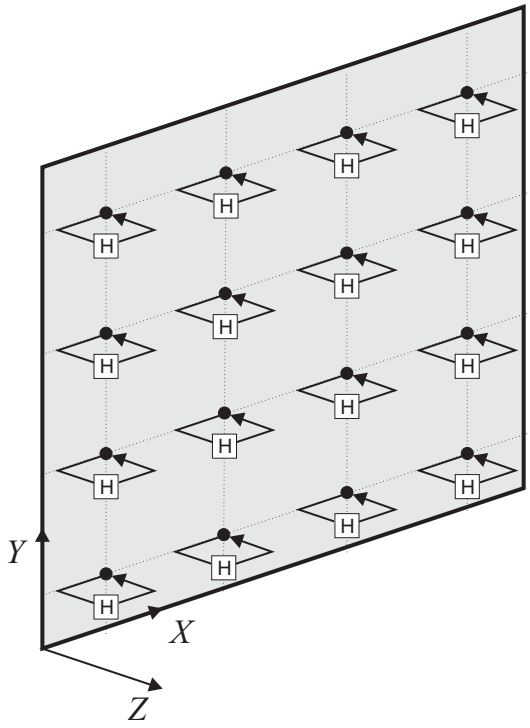

Figure 2.9: Panel model with an paradigmatic distribution of 16 discrete decentralized MIMO control feedback loops.

2.5.1 Active control with discrete point forces and velocity sensors

In extension to Equation (2.5) a set of distributed ideal control forces can be included in the formulation for the panel element velocity response, to give $\dot{\tilde{\mathbf{w}}}_e$ as

$$\dot{\tilde{\mathbf{w}}}_e = \tilde{\mathbf{Y}}_{ee}\tilde{\mathbf{F}}_{i,e} + \tilde{\mathbf{Y}}_{ec}\tilde{\mathbf{F}}_c, \tag{2.46}$$

where $\tilde{\mathbf{Y}}_{ec}$ is the $[N_e, N_c]$ dimensional matrix of transfer mobilities from the control positions to the panel element centres, where N_c is the total number of control loops. Assuming decentralised control loops are implemented, the vector of control forces $\tilde{\mathbf{F}}_c$ is given by the product of the velocities at the control positions and the control gains so that

$$\tilde{\mathbf{F}}_c = -\tilde{\mathbf{H}}_c\dot{\tilde{\mathbf{w}}}_c, \tag{2.47}$$

where $\tilde{\mathbf{H}}_c$ could generally be a fully populated complex matrix describing gain and phase

for all velocity feed back loops. For decentralized fixed gain feedback control this matrix reduces to a diagonal matrix of feedback gains. The velocity vector at the control positions $\dot{\tilde{\mathbf{w}}}_c$ is given by

$$\dot{\tilde{\mathbf{w}}}_c = \tilde{\mathbf{Y}}_{ce}\tilde{\mathbf{F}}_{i,e} + \tilde{\mathbf{Y}}_{cc}\tilde{\mathbf{F}}_c, \tag{2.48}$$

where $\tilde{\mathbf{Y}}_{cc}$ is the $[N_c, N_c]$ dimensional matrix of point and transfer mobilities for the control positions. Substituting Equation (2.47) into Equation (2.48) gives

$$\dot{\tilde{\mathbf{w}}}_c = \tilde{\mathbf{Y}}_{ce}\tilde{\mathbf{F}}_{i,e} - \tilde{\mathbf{Y}}_{cc}\tilde{\mathbf{H}}_c\dot{\tilde{\mathbf{w}}}_c. \tag{2.49}$$

An explicit formulation for $\dot{\tilde{\mathbf{w}}}_c$ can hence be written as

$$\dot{\tilde{\mathbf{w}}}_c = \left(\mathbf{I}_c + \tilde{\mathbf{Y}}_{cc}\tilde{\mathbf{H}}_c\right)^{-1}\tilde{\mathbf{Y}}_{ce}\tilde{\mathbf{F}}_{i,e} \tag{2.50}$$

and the control force $\tilde{\mathbf{F}}_c$ in equation (2.47) can subsequently be reformulated to yield

$$\tilde{\mathbf{F}}_c = -\tilde{\mathbf{H}}_c\left(\mathbf{I}_c + \tilde{\mathbf{Y}}_{cc}\tilde{\mathbf{H}}_c\right)^{-1}\tilde{\mathbf{Y}}_{ce}\tilde{\mathbf{F}}_{i,e}. \tag{2.51}$$

Substituting Equation (2.51) into Equation (2.46) and rearranging for $\dot{\tilde{\mathbf{w}}}_e$ finally gives

$$\dot{\tilde{\mathbf{w}}}_e = \underbrace{\left[\tilde{\mathbf{Y}}_{ee} - \tilde{\mathbf{Y}}_{ec}\tilde{\mathbf{H}}_c\left(\mathbf{I}_c + \tilde{\mathbf{Y}}_{cc}\tilde{\mathbf{H}}_c\right)^{-1}\tilde{\mathbf{Y}}_{ce}\right]}_{\tilde{\mathbb{Y}}_{ee}}\tilde{\mathbf{F}}_{i,e}, \tag{2.52}$$

where the term in square brackets represents the resulting panel element mobility matrix $\tilde{\mathbb{Y}}_{ee}$, including the response of the velocity feedback control forces. Figure 2.10 shows the two port network block diagram of the velocity feedback loops [20].

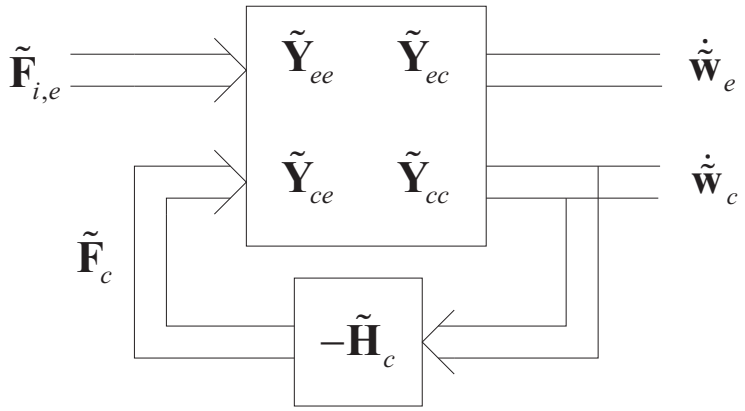

Figure 2.10: Block diagram for a panel model with multi channel feedback control loops.

As a practical note: When $\tilde{\mathbf{H}}_c$ is a diagonal matrix, as seen in Section 2.2, the computational effort can be reduced. Similar to Equation (2.14) a $[N_c, N_c]$ dimensional matrix $\tilde{\mathbf{\Phi}}_c$ is created, replicating the diagonal of $\tilde{\mathbf{H}}_c$ in each column. Then the matrix multiplication in Equation (2.52) is substituted by an element by element operations so that

$$\dot{\tilde{\mathbf{w}}}_e = \left[\tilde{\mathbf{Y}}_{ee} - \tilde{\mathbf{Y}}_{ec}\tilde{\mathbf{\Phi}}_c . \left(\mathbf{I}_c + \tilde{\mathbf{Y}}_{cc}.\tilde{\mathbf{\Phi}}_c^T\right)^{-1} \tilde{\mathbf{Y}}_{ce}\right] \tilde{\mathbf{F}}_{i,e}. \tag{2.53}$$

As discussed earlier, in this way it is possible to avoid a large number of multiplications by zero of diagonal terms. For the Equation (2.53) above, it is important to note, that

$$\mathbf{ADC} = \mathbf{A}(\mathbf{\Phi}.\mathbf{C}) = \mathbf{A}.\mathbf{\Phi}^T\mathbf{C} \tag{2.54}$$

where $\mathbf{D}$ is a diagonal matrix and $\mathbf{\Phi}$ is the replicated fully populated matrix sorted by columns as described above.

2.6 Fluid loaded panel model with feedback control loops

In this section the formulations for a fluid loaded panel from Section 2.4 and the panel model with decentralized velocity feedback control loops from Section 2.5 will be combined to one matrix formulation that can be represented with a two port network [20]. The block diagram in Figure 2.11 a) shows that this modelling problem reduces to the formulation of three independent back effects on the panel: The fluid loading reaction forces on

the source and the radiation sides of the panel and the control force feedback effect.

As before the element and control velocity vectors $\dot{\tilde{\mathbf{w}}}_e$ and $\dot{\tilde{\mathbf{w}}}_c$ are written in terms of element and control forces and the according mobility matrices to yield a set of two linear equations

$$\dot{\tilde{\mathbf{w}}}_e = \tilde{\mathbf{Y}}_{ee}\tilde{\mathbf{F}}_e + \tilde{\mathbf{Y}}_{ec}\tilde{\mathbf{F}}_c \tag{2.55}$$

$$\dot{\tilde{\mathbf{w}}}_c = \tilde{\mathbf{Y}}_{ce}\tilde{\mathbf{F}}_e + \tilde{\mathbf{Y}}_{cc}\tilde{\mathbf{F}}_c. \tag{2.56}$$

In contrast to the derivation in Section 2.5.1 the net elemental force $\tilde{\mathbf{F}}_e$ is considered instead of the incident element forces due to the disturbance. As discussed in Section 2.4, the net force on the element is given by the difference between incident force and radiation forces on the elements. The radiation forces can be expressed in terms of the element radiation impedances on the source and receiving side of the panel. The element and control forces can hence be written as

$$\tilde{\mathbf{F}}_e = \tilde{\mathbf{F}}_{i,e} - \tilde{\mathbf{F}}_{rad} = \tilde{\mathbf{F}}_{i,e} - \left(\tilde{\mathbf{Z}}_{rad,s} + \tilde{\mathbf{Z}}_{rad,r}\right)\dot{\tilde{\mathbf{w}}}_e \tag{2.57}$$

$$\tilde{\mathbf{F}}_c = -\tilde{\mathbf{H}}_c\dot{\tilde{\mathbf{w}}}_c. \tag{2.58}$$

Substituting these results in Equation (2.55) and (2.56) yields

$$\dot{\tilde{\mathbf{w}}}_e = \tilde{\mathbf{Y}}_{ee}\tilde{\mathbf{F}}_{i,e} - \tilde{\mathbf{Y}}_{ee}\left(\tilde{\mathbf{Z}}_{rad,s} + \tilde{\mathbf{Z}}_{rad,r}\right)\dot{\tilde{\mathbf{w}}}_e + \tilde{\mathbf{Y}}_{ec}\tilde{\mathbf{F}}_c \tag{2.59}$$

$$\dot{\tilde{\mathbf{w}}}_c = \tilde{\mathbf{Y}}_{ce}\tilde{\mathbf{F}}_{i,e} - \tilde{\mathbf{Y}}_{ce}\left(\tilde{\mathbf{Z}}_{rad,s} + \tilde{\mathbf{Z}}_{rad,r}\right)\dot{\tilde{\mathbf{w}}}_e + \tilde{\mathbf{Y}}_{cc}\tilde{\mathbf{F}}_c. \tag{2.60}$$

Substituting the explicit formulation for the control point velocities $\dot{\tilde{\mathbf{w}}}_c$ into Equation (2.59) and rearranging for the element velocity vector $\dot{\tilde{\mathbf{w}}}_e$ yields

$$\dot{\tilde{\mathbf{w}}}_e = \underbrace{\left[\left(\mathbf{I}_e + \tilde{\mathbf{Y}}_{ee}\left(\tilde{\mathbf{Z}}_{rad,s} + \tilde{\mathbf{Z}}_{rad,r}\right)\right)^{-1}\tilde{\mathbf{Y}}_{ee}\right]}_{\tilde{\mathbf{Q}}_{ee}}\tilde{\mathbf{F}}_{i,e} + \underbrace{\left[\left(\mathbf{I}_e + \tilde{\mathbf{Y}}_{ee}\left(\tilde{\mathbf{Z}}_{rad,s} + \tilde{\mathbf{Z}}_{rad,r}\right)\right)^{-1}\tilde{\mathbf{Y}}_{ec}\right]}_{\tilde{\mathbf{Q}}_{ec}}\tilde{\mathbf{F}}_c \tag{2.61}$$

where the terms in square brackets, $\tilde{\mathbf{Q}}_{ee}$ and $\tilde{\mathbf{Q}}_{ec}$, represent fluid coupled mobility matrices. This notation allows to short write the formulation for the element velocity vector $\dot{\tilde{\mathbf{w}}}_e$ as

$$\dot{\tilde{\mathbf{w}}}_e = \tilde{\mathbf{Q}}_{ee}\tilde{\mathbf{F}}_{i,e} + \tilde{\mathbf{Q}}_{ec}\tilde{\mathbf{F}}_c. \tag{2.62}$$

Substituting Equation (2.62) into Equation (2.60) gives the control point velocity vector as

$$\dot{\tilde{\mathbf{w}}}_c = \underbrace{\left[\left(\tilde{\mathbf{Y}}_{ce} - \tilde{\mathbf{Y}}_{ce}\left(\tilde{\mathbf{Z}}_{rad,s} + \tilde{\mathbf{Z}}_{rad,r}\right)\tilde{\mathbf{Q}}_{ee}\right)\right]}_{\tilde{\mathbf{Q}}_{ce}}\tilde{\mathbf{F}}_{i,e} + \underbrace{\left[\left(\tilde{\mathbf{Y}}_{cc} - \tilde{\mathbf{Y}}_{ce}\left(\tilde{\mathbf{Z}}_{rad,s} + \tilde{\mathbf{Z}}_{rad,r}\right)\tilde{\mathbf{Q}}_{ec}\right)\right]}_{\tilde{\mathbf{Q}}_{cc}}\tilde{\mathbf{F}}_c \tag{2.63}$$

where the terms in square brackets, $\tilde{\mathbf{Q}}_{ce}$ and $\tilde{\mathbf{Q}}_{cc}$, represent a second set of fluid coupled mobility matrices. This allows to short write the control velocity vector $\dot{\tilde{\mathbf{w}}}_c$ as

$$\dot{\tilde{\mathbf{w}}}_c = \tilde{\mathbf{Q}}_{ce}\tilde{\mathbf{F}}_{i,e} + \tilde{\mathbf{Q}}_{cc}\tilde{\mathbf{F}}_c. \tag{2.64}$$

Thus, as shown in Figure 2.11 b) the problem has been cast in the classic two port network via transfer matrices between the elements and control positions velocity / force functions for the fluid-loaded panel. Replacing the control force vector by Equation (2.58) and rearranging for $\dot{\tilde{\mathbf{w}}}_c$ gives

$$\dot{\tilde{\mathbf{w}}}_c = \left(\mathbf{I}_c + \tilde{\mathbf{Q}}_{cc}\tilde{\mathbf{H}}_c\right)^{-1}\tilde{\mathbf{Q}}_{ce}\tilde{\mathbf{F}}_{i,e}. \tag{2.65}$$

Utilizing Equation (2.58) again allows to eliminate the control point velocity term; rearranging for the control force vector gives

$$\dot{\tilde{\mathbf{F}}}_c = -\tilde{\mathbf{H}}_c\left(\mathbf{I}_c + \tilde{\mathbf{Q}}_{cc}\tilde{\mathbf{H}}_c\right)^{-1}\tilde{\mathbf{Q}}_{ce}\tilde{\mathbf{F}}_{i,e}. \tag{2.66}$$

Finally Equation (2.66) is substituted in Equation (2.55); rearranging for the element velocity vector $\dot{\tilde{\mathbf{w}}}_e$ one yields

$$\dot{\tilde{\mathbf{w}}}_e = \underbrace{\left[\tilde{\mathbf{Q}}_{ee} - \tilde{\mathbf{Q}}_{ec}\tilde{\mathbf{H}}_c\left(\mathbf{I}_c + \tilde{\mathbf{Q}}_{cc}\tilde{\mathbf{H}}_c\right)^{-1}\tilde{\mathbf{Q}}_{ce}\right]}_{\tilde{\mathbb{Y}}_{ee}}\tilde{\mathbf{F}}_{i,e}. \tag{2.67}$$

This expression is analogous to Equation (2.52) where the mobility matrices $\tilde{\mathbf{Y}}$ have been replaced by the fluid coupled mobility matrices $\tilde{\mathbf{Q}}$. The term in square brackets represents the resulting panel element mobility matrix $\tilde{\mathbb{Y}}_{ee}$, including loading from the surrounding fluid and the response of the velocity feedback control loops. Figure 2.11 shows the analogous block diagram in terms of a corresponding two port network.

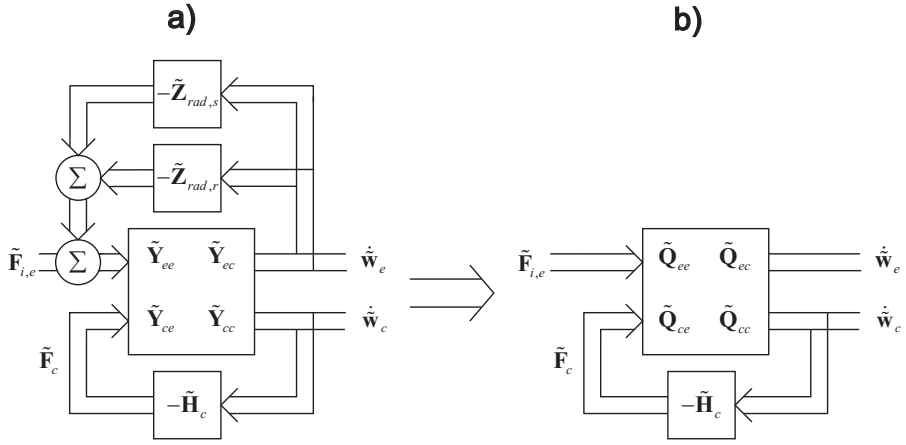

Figure 2.11: Block diagram for a panel model with fluid loading and multi channel feedback control loops. a): Separate consideration of active velocity feedback and fluid loading back forces; b): Combined two port network with fluid coupled mobility matrices.

2.7 Panel model with flexible boundaries

This section discusses the formulations for a rectangular panel with flexible boundary conditions. Initially a completely free panel is modelled. Boundary conditions are then enforced by introducing discrete back forces and moments along the panel boundaries. Visco-elastic-inertial boundary effects can be modelled as a mixture of acceleration, velocity and displacement reaction forces respectively. The formulations for the structural response are solely given in terms of matrix formulations.

In a first step linear boundary impedances are considered, the formulations are conceptually similar to those derived in Section 2.5.1 for active velocity feedback loops. In the limits of infinite boundary impedances this results in an approximation for a pinned

panel. Successively the formulations are extended to include reactive boundary moments in x and y direction. In the limits of infinite rotational boundary impedances a sliding panel can be approximated. The combination of infinite boundary forces and moments allows to approximate clamped boundaries. By varying the boundary impedances the formulations allow to model arbitrary visco-elastic-inertial boundary conditions.

The formulations for the natural frequencies, mode shapes and mobilities for a thin free free rectangular plate are taken from Gardonio and Brennan [10] (after Warburton [11]). For completeness it should be mentioned that more accurate solutions for the modal vibration response for thin complete free rectangular plates are available. Gorman [21, 22] discusses formulations for the response of completely free panels by the method of superposition. Gorman [23] also extends this method to the vibration analysis of completely free rectangular Mindlin plates. At this stage however the approximated formulation after Warburton [11] is assumed to be sufficiently accurate for the aims of this study.

2.7.1 Discrete boundary forces

The formulations for purely linear boundary forces on the edges of a completely free panel are conceptually similar to the formulations derived for active velocity feedback loops in Section 2.5.1. The discussed boundaries however do not resemble active but reactive forces.

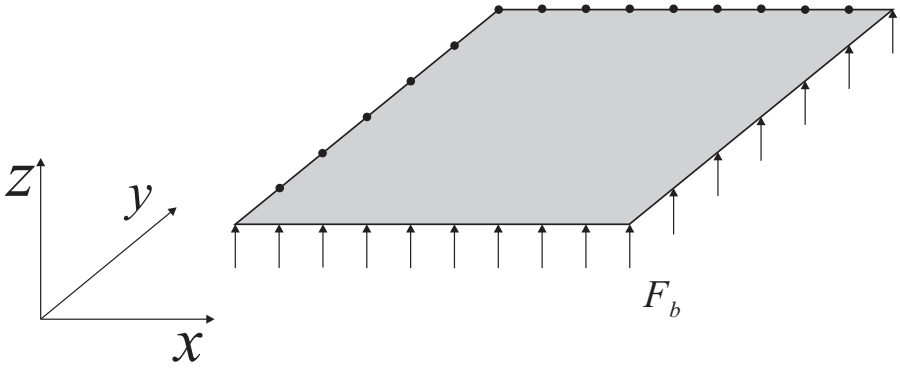

Figure 2.12: Completely free panel with variable boundary feedback forces

Similar to the derivation in Section 2.5.1 the initial expression for the element velocity vector in Equation (2.5) is extended by formulations for distributed boundary reaction forces, to give $\dot{\tilde{\mathbf{w}}}_e$ as

$$\dot{\tilde{\mathbf{w}}}_e = \tilde{\mathbf{Y}}_{ee}\tilde{\mathbf{F}}_{i,e} + \tilde{\mathbf{Y}}_{eb}\tilde{\mathbf{F}}_b. \tag{2.68}$$

where $\tilde{\mathbf{Y}}_{eb}$ is the $[N_e, N_b]$ dimensional matrix of transfer boundary mobilities to the panel element centres, where N_b is the total number of discrete boundary points. The vector of boundary forces $\tilde{\mathbf{F}}_b$ is given by the product of the velocities at boundary locations and the square $[N_b, N_b]$ dimensional matrix of boundary point impedances $\tilde{\mathbf{Z}}_{F,b}$,

$$\tilde{\mathbf{F}}_b = -\tilde{\mathbf{Z}}_{F,b}\dot{\tilde{\mathbf{w}}}_c, \tag{2.69}$$

where $\tilde{\mathbf{Z}}_{F,b}$ generally is a diagonal matrix. The velocity vector at the boundary locations $\dot{\tilde{\mathbf{w}}}_b$ is given by

$$\dot{\tilde{\mathbf{w}}}_b = \tilde{\mathbf{Y}}_{be}\tilde{\mathbf{F}}_{i,e} + \tilde{\mathbf{Y}}_{bb}\tilde{\mathbf{F}}_b, \tag{2.70}$$

where $\tilde{\mathbf{Y}}_{bb}$ is the $[N_b, N_b]$ dimensional matrix of point and transfer boundary mobilities. Substituting Equation (2.69) into Equation (2.70) and rearranging for the velocities along the boundary $\dot{\tilde{\mathbf{w}}}_b$ gives

$$\dot{\tilde{\mathbf{w}}}_b = \left(\mathbf{I}_b + \tilde{\mathbf{Y}}_{bb}\tilde{\mathbf{Z}}_{F,b}\right)^{-1}\tilde{\mathbf{Y}}_{be}\tilde{\mathbf{F}}_{i,e} \tag{2.71}$$

and the boundary forces $\tilde{\mathbf{F}}_b$ in equation (2.69) can subsequently be reformulated to yield

$$\dot{\tilde{\mathbf{F}}}_b = -\tilde{\mathbf{Z}}_b\left(\mathbf{I}_b + \tilde{\mathbf{Y}}_{bb}\tilde{\mathbf{Z}}_{F,b}\right)^{-1}\tilde{\mathbf{Y}}_{be}\tilde{\mathbf{F}}_{i,e}. \tag{2.72}$$

Substituting Equation (2.72) into Equation (2.68) and rearranging for $\dot{\tilde{\mathbf{w}}}_e$ finally gives

$$\dot{\tilde{\mathbf{w}}}_e = \underbrace{\left[\tilde{\mathbf{Y}}_{ee} - \tilde{\mathbf{Y}}_{eb}\tilde{\mathbf{Z}}_{F_b}\left(\mathbf{I}_c + \tilde{\mathbf{Y}}_{bb}\tilde{\mathbf{Z}}_{F,b}\right)^{-1}\tilde{\mathbf{Y}}_{be}\right]}_{\tilde{\mathbb{Y}}_{ee}}\tilde{\mathbf{F}}_{i,e}. \tag{2.73}$$

In general the boundary point impedance $\tilde{Z}_{F,b}(\omega)$ is a function of frequency. The impedances at each boundary location can be represented in terms of masses, dampers and springs.

The boundary impedance matrix is therefore assembled from

$$\tilde{Z}_{b_n}(\omega) = \quad i\omega m_{b_n} \quad + \quad b_{b_n} \quad + \quad \frac{s_{b_n}}{i\omega} \tag{2.74}$$

where n denotes the index of the discrete boundary location and m_b, b_b and s_b denote mass [kg], damping coefficient [Nsm^{-1}] and stiffness [Nm^{-1}] boundary parameters.

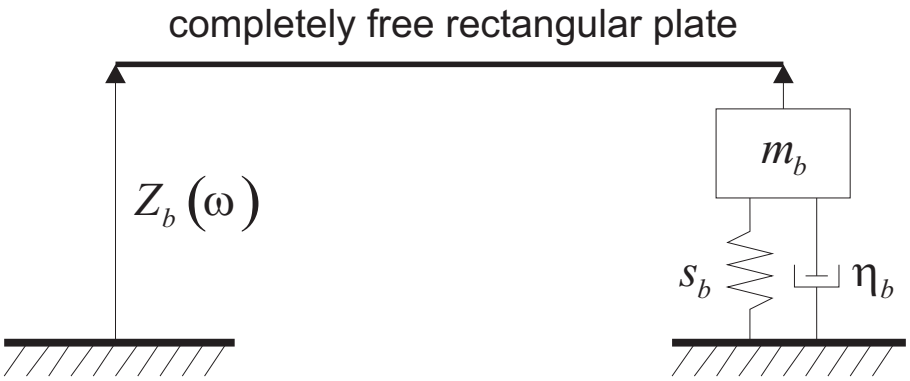

Figure 2.13: Completely free panel with variable linear boundary impedance.

2.7.2 Discrete boundary forces and moments

In a next logical step the same framework can be used include reactive boundary moments. These moments are proportional to the angular velocities $\dot{\tilde{\Theta}}_x$ and $\dot{\tilde{\Theta}}_y$ at the discrete boundary positions along the panel edges. Formulations for the rotational modeshapes and the nine possible combinations for linear and rotational acceptance terms for forces and moments are discussed by Gardonio and Brennan [10], formulations used within this report are given in Appendix B.

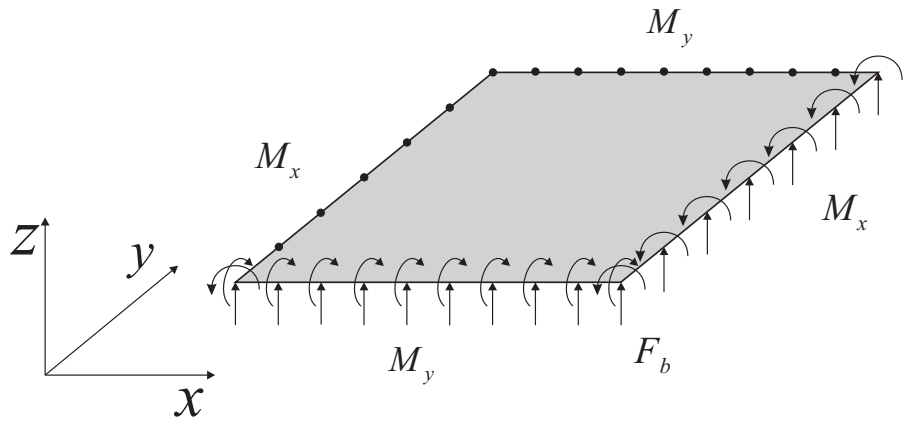

Figure 2.14: Completely free panel with variable boundary feedback forces and moments.

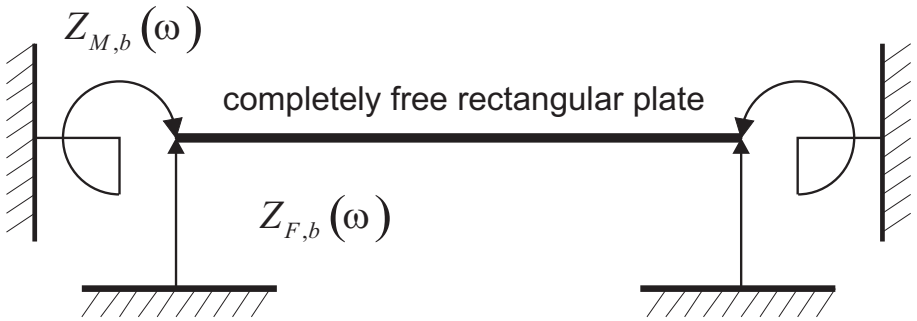

Figure 2.15: Completely free panel with variable linear and rotational boundary impedances.

The formulation for the element velocity vector in Equation (2.68) is extended to give

$$\dot{\tilde{\mathbf{w}}}_e = \tilde{\mathbf{Y}}_{\dot{\tilde{w}},F,ee}\tilde{\mathbf{F}}_{i,e} + \tilde{\mathbb{Y}}_{eb}\tilde{\mathbb{F}}_b \tag{2.75}$$

where $\tilde{\mathbb{Y}}_{eb}$ is the combined matrix of force and moment mobilities defined as

$$\tilde{\mathbb{Y}}_{eb} = \left[\begin{array}{ccc} \tilde{\mathbf{Y}}_{\dot{\tilde{w}},F,eb} & \tilde{\mathbf{Y}}_{\dot{\tilde{w}},M_x,eb} & \tilde{\mathbf{Y}}_{\dot{\tilde{w}},M_y,eb} \end{array} \right] \tag{2.76}$$

where $\tilde{\mathbf{Y}}_{\dot{\tilde{w}},F,eb}$ term denotes the boundary force mobility matrix as used before and $\tilde{\mathbf{Y}}_{\dot{\tilde{w}},M_x,eb}$ and $\tilde{\mathbf{Y}}_{\dot{\tilde{w}},M_x,eb}$ denote the boundary moment mobilities. The combined boundary 'force' matrix $\tilde{\mathbb{F}}_b$ is defined as

$$\tilde{\mathbb{F}}_b = \begin{bmatrix} \tilde{\mathbf{F}}_b \\ \tilde{\mathbf{M}}_{x,b} \\ \tilde{\mathbf{M}}_{y,b} \end{bmatrix} \tag{2.77}$$

where $\tilde{\mathbf{F}}_b$ is the vector of boundary forces and $\tilde{\mathbf{M}}_{x,b}$ and $\tilde{\mathbf{M}}_{y,b}$ denote the vectors of boundary moments in x and y direction. Conceptually similar to the derivations before, the force and moment vectors are expressed as the product of boundary impedance matrices $\tilde{\mathbf{Z}}_{F,b}$, $\tilde{\mathbf{Z}}_{M_x,b}$ and $\tilde{\mathbf{Z}}_{M_y,b}$ and the lateral and angular boundary velocity vectors $\dot{\tilde{\mathbf{w}}}_b$, $\dot{\tilde{\mathbf{\Theta}}}_{x,b}$ and $\dot{\tilde{\mathbf{\Theta}}}_{x,b}$, so that

$$\begin{aligned} \dot{\tilde{\mathbf{F}}}_b &= -\tilde{\mathbf{Z}}_{F,b}\dot{\tilde{\mathbf{w}}}_b \\ \dot{\tilde{\mathbf{M}}}_{x,b} &= -\tilde{\mathbf{Z}}_{M_x,b}\dot{\tilde{\mathbf{\Theta}}}_{x,b} \\ \dot{\tilde{\mathbf{M}}}_{y,b} &= -\tilde{\mathbf{Z}}_{M_y,b}\dot{\tilde{\mathbf{\Theta}}}_{y,b}. \end{aligned} \tag{2.78}$$

The linear and angular velocities at the control positions $\dot{\tilde{\mathbf{w}}}_b$ and $\dot{\tilde{\mathbf{\Theta}}}_{x,b}$, $\dot{\tilde{\mathbf{\Theta}}}_{y,b}$ are given by a set of linear simultaneous equations. Similar to the derivations in Section 2.7.1 Equation (2.71) yields

$$\dot{\tilde{\mathbb{W}}}_b = \left(\mathbb{I}_b + \tilde{\mathbb{Y}}_{bb}\tilde{\mathbb{Z}}_b\right)^{-1} \tilde{\mathbb{Y}}_{be}\tilde{\mathbf{F}}_{i,e}, \tag{2.79}$$

where $\dot{\tilde{\mathbb{W}}}_b$ denotes the vector of linear and angular velocities

$$\dot{\tilde{\mathbb{W}}}_b = \begin{bmatrix} \dot{\tilde{\mathbf{w}}}_b \\ \dot{\tilde{\mathbf{\Theta}}}_{x,b} \\ \dot{\tilde{\mathbf{\Theta}}}_{y,b} \end{bmatrix}, \tag{2.80}$$

$\tilde{\mathbb{Y}}_{bb}$ is the block matrix of point and transfer, force and moment mobilities of the discrete boundary points

$$\tilde{\mathbb{Y}}_{bb} = \begin{bmatrix} \tilde{\mathbf{Y}}_{\dot{\tilde{w}},F,bb} & \tilde{\mathbf{Y}}_{\dot{\tilde{w}},M_x,bb} & \tilde{\mathbf{Y}}_{\dot{\tilde{w}},M_y,bb} \\ \tilde{\mathbf{Y}}_{\dot{\tilde{\Theta}}_x,F,bb} & \tilde{\mathbf{Y}}_{\dot{\tilde{\Theta}}_x,M_x,bb} & \tilde{\mathbf{Y}}_{\dot{\tilde{\Theta}}_x,M_y,bb} \\ \tilde{\mathbf{Y}}_{\dot{\tilde{\Theta}}_y,F,bb} & \tilde{\mathbf{Y}}_{\dot{\tilde{\Theta}}_y,M_x,bb} & \tilde{\mathbf{Y}}_{\dot{\tilde{\Theta}}_y,M_y,bb} \end{bmatrix}, \tag{2.81}$$

$\tilde{\mathbb{Y}}_{be}$ is the block matrix of transfer mobilities between the panel elements and the boundary locations

$$\tilde{\mathbb{Y}}_{be} = \begin{bmatrix} \tilde{\mathbf{Y}}_{\dot{\hat{w}},F,be} \\ \tilde{\mathbf{Y}}_{\Theta_x,F,be} \\ \tilde{\mathbf{Y}}_{\Theta_y,F,be} \end{bmatrix} \tag{2.82}$$

and $\tilde{\mathbb{Z}}_b$ is the block matrix of force and moment boundary impedances

$$\tilde{\mathbb{Z}}_b = \begin{bmatrix} \tilde{\mathbf{Z}}_{F,b} & 0 & 0 \\ 0 & \tilde{\mathbf{Z}}_{M_x,b} & 0 \\ 0 & 0 & \tilde{\mathbf{Z}}_{M_y,b} \end{bmatrix}. \tag{2.83}$$

The boundary force in Equation (2.75) can subsequently be rewritten as

$$\tilde{\mathbb{F}}_b = -\tilde{\mathbb{H}}_b \left(\mathbb{I}_b + \tilde{\mathbb{Y}}_{bb} \tilde{\mathbb{Z}}_b \right)^{-1} \tilde{\mathbb{Y}}_{be} \tilde{\mathbf{F}}_{i,e}. \tag{2.84}$$

Substituting Equation (2.84) in (2.75) and rearranging for the vector of lateral panel element velocities $\dot{\tilde{\mathbf{w}}}_e$ finally yields

$$\dot{\tilde{\mathbf{w}}}_e = \underbrace{\left[\tilde{\mathbf{Y}}_{ee} - \tilde{\mathbb{Y}}_{eb} \tilde{\mathbb{Z}}_b \left(\mathbb{I}_b + \tilde{\mathbb{Y}}_{bb} \tilde{\mathbb{Z}}_b \right)^{-1} \tilde{\mathbb{Y}}_{be} \right]}_{\tilde{\mathbb{Y}}_{ee}} \tilde{\mathbf{F}}_{i,e} \tag{2.85}$$

where the term under in square brackets represents the resulting panel element mobility matrix $\tilde{\mathbb{Y}}_{ee}$, including the boundary feedback forces and moments.

2.8 Panel model with feedback control loops and flexible boundaries

This section discusses formulations for an element based panel model that allows to consider active velocity feedback control loops and flexible boundaries at the same time. Combining the control and boundary forces might be formulated in two different ways

- The boundary and control forces could be combined in one matrix formulation similar to those derived for combined force and moment boundary impedance in Section 2.7.2. This formulation is very appealing from the mathematical point of view since it involves just one matrix expression. However, it does not yield a good insight into the actual physics of the system and also does not offer an efficient computational approach since the matrices are formed by many blocks of zeros.

- The problem can also be formulated keeping the boundary conditions and the feedback control parts of the problem separate. This is thought to be the preferred approach since it will give a better insight into the actual physics of the system. Also it should prove more computationally efficient and improve numerical accuracy since the matrix formulation is broken down into sub steps which involve fully populated smaller matrices, which can be more efficiently manipulated numerically, particularly inversion operations become more efficient and accurate.

The relationship between the velocity of the panel elements $\dot{\tilde{\mathbf{w}}}_e$, the control positions $\dot{\tilde{\mathbf{w}}}_c$ and the boundary locations $\dot{\tilde{\mathbf{w}}}_b$ along the plate edges can be described as a set of three linear algebraic matrix equations:

$$\begin{aligned}
\dot{\tilde{\mathbf{w}}}_e &= \tilde{\mathbf{Y}}_{ee}\tilde{\mathbf{F}}_{i,e} + \tilde{\mathbf{Y}}_{ec}\tilde{\mathbf{F}}_c + \tilde{\mathbf{Y}}_{eb}\tilde{\mathbf{F}}_b, \\
\dot{\tilde{\mathbf{w}}}_b &= \tilde{\mathbf{Y}}_{be}\tilde{\mathbf{F}}_{i,e} + \tilde{\mathbf{Y}}_{bc}\tilde{\mathbf{F}}_c + \tilde{\mathbf{Y}}_{bb}\tilde{\mathbf{F}}_b, \\
\dot{\tilde{\mathbf{w}}}_c &= \tilde{\mathbf{Y}}_{ce}\tilde{\mathbf{F}}_{i,e} + \tilde{\mathbf{Y}}_{cc}\tilde{\mathbf{F}}_c + \tilde{\mathbf{Y}}_{cb}\tilde{\mathbf{F}}_b.
\end{aligned} \tag{2.86}$$

As for derivations in the previous sections, the control feedback and boundary force vectors $\tilde{\mathbf{F}}$ are given by the product of the velocities at the corresponding panel coordinates $\dot{\tilde{\mathbf{w}}}$ and the associated feedback control gain matrix $\tilde{\mathbf{H}}_c$ and boundary impedance matrix $\tilde{\mathbf{Z}}_b$, so that

$$\tilde{\mathbf{F}}_b = -\tilde{\mathbf{Z}}_b\dot{\tilde{\mathbf{w}}}_b \tag{2.87}$$

$$\tilde{\mathbf{F}}_c = -\tilde{\mathbf{H}}_c\dot{\tilde{\mathbf{w}}}_c. \tag{2.88}$$

The element velocity vector $\dot{\tilde{\mathbf{w}}}_e$ can therefore be written in terms of the velocity at the control positions $\dot{\tilde{\mathbf{w}}}_c$ and the boundary positions $\dot{\tilde{\mathbf{w}}}_b$ to yield

$$\dot{\tilde{\mathbf{w}}}_e = \tilde{\mathbf{Y}}_{ee}\tilde{\mathbf{F}}_{i,e} - \tilde{\mathbf{Y}}_{eb}\tilde{\mathbf{Z}}_b\dot{\tilde{\mathbf{w}}}_b - \tilde{\mathbf{Y}}_{ec}\tilde{\mathbf{H}}_c\dot{\tilde{\mathbf{w}}}_c. \tag{2.89}$$

Accordingly the velocity vectors for the control positions $\dot{\tilde{\mathbf{w}}}_c$ and boundary locations $\dot{\tilde{\mathbf{w}}}_b$ can be written as

$$\dot{\tilde{\mathbf{w}}}_b = \tilde{\mathbf{Y}}_{be}\tilde{\mathbf{F}}_{i,e} - \tilde{\mathbf{Y}}_{bc}\tilde{\mathbf{H}}_c\dot{\tilde{\mathbf{w}}}_c + \tilde{\mathbf{Y}}_{bb}\tilde{\mathbf{F}}_b \tag{2.90}$$

$$\dot{\tilde{\mathbf{w}}}_c = \tilde{\mathbf{Y}}_{ce}\tilde{\mathbf{F}}_{i,e} - \tilde{\mathbf{Y}}_{cc}\tilde{\mathbf{H}}_c\dot{\tilde{\mathbf{w}}}_c + \tilde{\mathbf{Y}}_{eb}\tilde{\mathbf{F}}_b. \tag{2.91}$$

An explicit formulation for $\dot{\tilde{\mathbf{w}}}_c$ can now be found by rearranging (2.91), which gives

$$\dot{\tilde{\mathbf{w}}}_c = \left(\mathbf{I_c} + \tilde{\mathbf{Y}}_{cc}\tilde{\mathbf{H}}_c\right)^{-1}\tilde{\mathbf{Y}}_{cb}\tilde{\mathbf{F}}_b + \left(\mathbf{I_c} + \tilde{\mathbf{Y}}_{cc}\tilde{\mathbf{H}}_c\right)^{-1}\tilde{\mathbf{Y}}_{ce}\tilde{\mathbf{F}}_{i,e}. \tag{2.92}$$

Substituting this into the formulation for $\dot{\tilde{\mathbf{w}}}_b$ in Equation (2.90) yields

$$\dot{\tilde{\mathbf{w}}}_b = \underbrace{\left[\tilde{\mathbf{Y}}_{be} - \tilde{\mathbf{Y}}_{bc}\tilde{\mathbf{H}}_c\left(\mathbf{I_c} + \tilde{\mathbf{Y}}_{cc}\tilde{\mathbf{H}}_c\right)^{-1}\tilde{\mathbf{Y}}_{ce}\right]}_{\tilde{\mathbf{T}}_{be}}\tilde{\mathbf{F}}_{i,e} + \underbrace{\left[\tilde{\mathbf{Y}}_{bb} - \tilde{\mathbf{Y}}_{bc}\tilde{\mathbf{H}}_c\left(\mathbf{I_c} + \tilde{\mathbf{Y}}_{cc}\tilde{\mathbf{H}}_c\right)^{-1}\tilde{\mathbf{Y}}_{cb}\right]}_{\tilde{\mathbf{T}}_{bb}}\tilde{\mathbf{F}}_b. \tag{2.93}$$

Using the relation between boundary feedback force $\tilde{\mathbf{F}}_b$ and boundary impedance $\tilde{\mathbf{Z}}_b$ in Equation (2.87) and (2.88) finally allows to formulate an explicit equation for the vector of panel boundary velocities as

$$\dot{\tilde{\mathbf{w}}}_b = \left(\mathbf{I_b} + \tilde{\mathbf{T}}_{bb}\tilde{\mathbf{Z}}_\mathbf{b}\right)^{-1}\tilde{\mathbf{T}}_{be}\tilde{\mathbf{F}}_{i,e}. \tag{2.94}$$

Similarly explicit expressions for the vector of control velocities can be derived to give

$$\dot{\tilde{\mathbf{w}}}_c = \underbrace{\left[\tilde{\mathbf{Y}}_{ce} - \tilde{\mathbf{Y}}_{cb}\tilde{\mathbf{Z}}_b\left(\mathbf{I_b} + \tilde{\mathbf{Y}}_{bb}\tilde{\mathbf{Z}}_b\right)^{-1}\tilde{\mathbf{Y}}_{be}\right]}_{\tilde{\mathbf{T}}_{ce}}\tilde{\mathbf{F}}_{i,e} + \underbrace{\left[\tilde{\mathbf{Y}}_{cc} - \tilde{\mathbf{Y}}_{cb}\tilde{\mathbf{Z}}_b\left(\mathbf{I_b} + \tilde{\mathbf{Y}}_{bb}\tilde{\mathbf{Z}}_b\right)^{-1}\tilde{\mathbf{Y}}_{bc}\right]}_{\tilde{\mathbf{T}}_{cc}}\tilde{\mathbf{F}}_c, \quad (2.95)$$

i.e. substituting equation (2.88)

$$\dot{\tilde{\mathbf{w}}}_c = \left(\mathbf{I}_c + \tilde{\mathbf{T}}_{cc}\tilde{\mathbf{H}}_c\right)^{-1}\tilde{\mathbf{T}}_{ce}\tilde{\mathbf{F}}_{i,e}. \quad (2.96)$$

Substituting the expressions for $\dot{\tilde{\mathbf{w}}}_c$ in Equation (2.96) and $\dot{\tilde{\mathbf{w}}}_b$ in Equation (2.94) into Equation (2.89) yields the vector of plate element velocities as

$$\dot{\tilde{\mathbf{w}}}_e = \underbrace{\left[\tilde{\mathbf{Y}}_{ee} - \tilde{\mathbf{Y}}_{ec}\tilde{\mathbf{H}}_c\left(\mathbf{I}_c + \tilde{\mathbf{T}}_{cc}\tilde{\mathbf{H}}_c\right)^{-1}\tilde{\mathbf{T}}_{ce} - \tilde{\mathbf{Y}}_{eb}\tilde{\mathbf{Z}}_b\left(\mathbf{I}_b + \tilde{\mathbf{T}}_{bb}\tilde{\mathbf{Z}}_b\right)^{-1}\tilde{\mathbf{T}}_{be}\right]}_{\tilde{\mathbb{Y}}_{ee}}\tilde{\mathbf{F}}_{i,e}. \quad (2.97)$$

where the term under in square brackets represents the resulting panel element mobility matrix $\tilde{\mathbb{Y}}_{ee}$, including feedback control forces and flexible boundaries. Figure 2.16 shows the corresponding combined block diagram as a three port network.

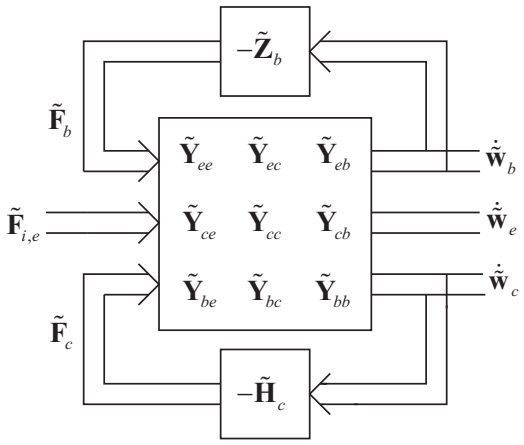

Figure 2.16: Block diagram for a panel model with discrete decentralized multi channel feedback control loops and discrete boundary impedances.

As a next logical step rotational moment boundary feedback can be introduced to enforce restricted rotation in x and y along the panel edges. Similar to the derivation in section 2.7.2 the additional degrees of freedom can be included by exchanging the boundary

transfer mobility, and boundary impedance matrices in Equation (2.93), (2.95) and (2.97) by block matrixes containing rotational impedances.

2.9 Fluid loaded panel model with feedback control loops and flexible boundaries

To complete the set of formulations, a combined expression that allows to consider a fluid loaded panel model with feedback control loops and flexible boundaries is derived in this section. The derivation conceptually follows the methodology in Sections 2.4 to 2.8.

Similar to Equation (2.86) the relationship between the velocity of the panel elements $\dot{\tilde{\mathbf{w}}}_e$, the control positions $\dot{\tilde{\mathbf{w}}}_c$ and the boundary locations $\dot{\tilde{\mathbf{w}}}_b$ along the plate edges can be described as a set of three linear algebraic equations:

$$\begin{aligned}
\dot{\tilde{\mathbf{w}}}_e &= \tilde{\mathbf{Y}}_{ee}\tilde{\mathbf{F}}_e + \tilde{\mathbf{Y}}_{eb}\tilde{\mathbf{F}}_b + \tilde{\mathbf{Y}}_{ec}\tilde{\mathbf{F}}_c, \\
\dot{\tilde{\mathbf{w}}}_b &= \tilde{\mathbf{Y}}_{be}\tilde{\mathbf{F}}_e + \tilde{\mathbf{Y}}_{bb}\tilde{\mathbf{F}}_b + \tilde{\mathbf{Y}}_{bc}\tilde{\mathbf{F}}_c, \\
\dot{\tilde{\mathbf{w}}}_c &= \tilde{\mathbf{Y}}_{ce}\tilde{\mathbf{F}}_e + \tilde{\mathbf{Y}}_{cb}\tilde{\mathbf{F}}_b + \tilde{\mathbf{Y}}_{cc}\tilde{\mathbf{F}}_c.
\end{aligned} \tag{2.98}$$

The only difference is that instead of the incident element forces $\tilde{\mathbf{F}}_{i,e}$, the net element forces $\tilde{\mathbf{F}}_e$ are considered here. With the definitions of the radiation force in Equation (2.40) the net element force, control and boundary force vectors are given by

$$\begin{aligned}
\dot{\tilde{\mathbf{F}}}_e &= \dot{\tilde{\mathbf{F}}}_{i,e} - \left(\tilde{\mathbf{Z}}_{rad,s} + \tilde{\mathbf{Z}}_{rad,r}\right)\dot{\tilde{\mathbf{w}}}_e \\
\dot{\tilde{\mathbf{F}}}_b &= -\tilde{\mathbf{H}}_b\dot{\tilde{\mathbf{w}}}_b \\
\dot{\tilde{\mathbf{F}}}_c &= -\tilde{\mathbf{H}}_c\dot{\tilde{\mathbf{w}}}_c
\end{aligned} \tag{2.99}$$

Analogous to section 2.6 Equations (2.89), (2.90) and (2.91) we can rewrite the formulations for the velocity vectors as

$$\begin{aligned}
\dot{\tilde{\mathbf{w}}}_e &= \tilde{\mathbf{Q}}_{ee}\tilde{\mathbf{F}}_e + \tilde{\mathbf{Q}}_{eb}\tilde{\mathbf{F}}_b + \tilde{\mathbf{Q}}_{ec}\tilde{\mathbf{F}}_c \\
\dot{\tilde{\mathbf{w}}}_b &= \tilde{\mathbf{Q}}_{be}\tilde{\mathbf{F}}_e + \tilde{\mathbf{Q}}_{bb}\tilde{\mathbf{F}}_b + \tilde{\mathbf{Q}}_{bc}\tilde{\mathbf{F}}_c \\
\dot{\tilde{\mathbf{w}}}_c &= \tilde{\mathbf{Q}}_{ce}\tilde{\mathbf{F}}_e + \tilde{\mathbf{Q}}_{cb}\tilde{\mathbf{F}}_b + \tilde{\mathbf{Q}}_{cc}\tilde{\mathbf{F}}_c.
\end{aligned} \tag{2.100}$$

where the fluid coupled mobility terms $\tilde{\mathbf{Q}}$ (compare Section 2.6 Equation (2.61) and (2.63)) are given by

$$\begin{aligned}
\tilde{\mathbf{Q}}_{ee} &= \left[\mathbf{I}_e + \tilde{\mathbf{Y}}_{ee}\left(\tilde{\mathbf{Z}}_{rad,s} + \tilde{\mathbf{Z}}_{rad,r}\right)\right]^{-1} \tilde{\mathbf{Y}}_{ee} \\
\tilde{\mathbf{Q}}_{eb} &= \left[\mathbf{I}_e + \tilde{\mathbf{Y}}_{ee}\left(\tilde{\mathbf{Z}}_{rad,s} + \tilde{\mathbf{Z}}_{rad,r}\right)\right]^{-1} \tilde{\mathbf{Y}}_{eb} \\
\tilde{\mathbf{Q}}_{ec} &= \left[\mathbf{I}_e + \tilde{\mathbf{Y}}_{ee}\left(\tilde{\mathbf{Z}}_{rad,s} + \tilde{\mathbf{Z}}_{rad,r}\right)\right]^{-1} \tilde{\mathbf{Y}}_{ec}
\end{aligned} \tag{2.101}$$

$$\begin{aligned}
\tilde{\mathbf{Q}}_{be} &= \tilde{\mathbf{Y}}_{be} - \tilde{\mathbf{Y}}_{be}\left(\tilde{\mathbf{Z}}_{rad,s} + \tilde{\mathbf{Z}}_{rad,r}\right) \tilde{\mathbf{Q}}_{ee} \\
\tilde{\mathbf{Q}}_{bb} &= \tilde{\mathbf{Y}}_{bb} - \tilde{\mathbf{Y}}_{be}\left(\tilde{\mathbf{Z}}_{rad,s} + \tilde{\mathbf{Z}}_{rad,r}\right) \tilde{\mathbf{Q}}_{eb} \\
\tilde{\mathbf{Q}}_{bc} &= \tilde{\mathbf{Y}}_{bc} - \tilde{\mathbf{Y}}_{be}\left(\tilde{\mathbf{Z}}_{rad,s} + \tilde{\mathbf{Z}}_{rad,r}\right) \tilde{\mathbf{Q}}_{ec}
\end{aligned} \tag{2.102}$$

$$\begin{aligned}
\tilde{\mathbf{Q}}_{ce} &= \tilde{\mathbf{Y}}_{ce} - \tilde{\mathbf{Y}}_{ce}\left(\tilde{\mathbf{Z}}_{rad,s} + \tilde{\mathbf{Z}}_{rad,r}\right) \tilde{\mathbf{Q}}_{ee} \\
\tilde{\mathbf{Q}}_{cb} &= \tilde{\mathbf{Y}}_{cb} - \tilde{\mathbf{Y}}_{ce}\left(\tilde{\mathbf{Z}}_{rad,s} + \tilde{\mathbf{Z}}_{rad,r}\right) \tilde{\mathbf{Q}}_{eb} \\
\tilde{\mathbf{Q}}_{cc} &= \tilde{\mathbf{Y}}_{cc} - \tilde{\mathbf{Y}}_{ce}\left(\tilde{\mathbf{Z}}_{rad,s} + \tilde{\mathbf{Z}}_{rad,r}\right) \tilde{\mathbf{Q}}_{ec}
\end{aligned} . \tag{2.103}$$

The introduction of variable boundary forces is conducted following the formulations in Section 2.8 to yield the final formulation for the element velocity vector as

$$\dot{\tilde{\mathbf{w}}}_e = \underbrace{\left[\tilde{\mathbf{Q}}_{ee} - \tilde{\mathbf{Q}}_{ec}\tilde{\mathbf{H}}_c\left(\mathbf{I}_c + \tilde{\mathbb{T}}_{cc}\tilde{\mathbf{H}}_c\right)^{-1}\tilde{\mathbb{T}}_{ce} - \tilde{\mathbf{Q}}_{eb}\tilde{\mathbf{Z}}_b\left(\mathbf{I}_b + \tilde{\mathbb{T}}_{bb}\tilde{\mathbf{Z}}_b\right)^{-1}\tilde{\mathbb{T}}_{be}\right]}_{\tilde{\mathbb{Y}}_{ee}} \tilde{\mathbf{F}}_{i,e}, \tag{2.104}$$

where the term in square brackets represents the resulting panel element mobility matrix $\tilde{\mathbb{Y}}_{ee}$, including loading from the surrounding fluid, feedback control loops and variable boundary conditions. The fluid coupled boundary and control mobility terms $\tilde{\mathbb{T}}$ (compare Section 2.8 Equation (2.93) and (2.95)) are given by

$$\begin{aligned}
\tilde{\mathbb{T}}_{be} &= \tilde{\mathbf{Q}}_{be} - \tilde{\mathbf{Q}}_{bc}\tilde{\mathbf{H}}_c\left(\mathbf{I}_c + \tilde{\mathbf{Q}}_{cc}\tilde{\mathbf{H}}_c\right)^{-1}\tilde{\mathbf{Q}}_{ce} \\
\tilde{\mathbb{T}}_{bb} &= \tilde{\mathbf{Q}}_{bb} - \tilde{\mathbf{Q}}_{bc}\tilde{\mathbf{H}}_c\left(\mathbf{I}_c + \tilde{\mathbf{Q}}_{cc}\tilde{\mathbf{H}}_c\right)^{-1}\tilde{\mathbf{Q}}_{cb} \\
\tilde{\mathbb{T}}_{ce} &= \tilde{\mathbf{Q}}_{ce} - \tilde{\mathbf{Q}}_{cb}\tilde{\mathbf{Z}}_b\left(\mathbf{I}_b + \tilde{\mathbf{Q}}_{bb}\tilde{\mathbf{Z}}_b\right)^{-1}\tilde{\mathbf{Q}}_{be} \\
\tilde{\mathbb{T}}_{cc} &= \tilde{\mathbf{Q}}_{cc} - \tilde{\mathbf{Q}}_{cb}\tilde{\mathbf{Z}}_b\left(\mathbf{I}_b + \tilde{\mathbf{Q}}_{bb}\tilde{\mathbf{Z}}_b\right)^{-1}\tilde{\mathbf{Q}}_{bc}
\end{aligned} \tag{2.105}$$

As a further generalisation the rotational moment boundary feedback can be introduced by exchanging the boundary transfer mobility, and boundary impedance matrix terms $\tilde{\mathbf{Q}}_{eb}$, $\tilde{\mathbf{Q}}_{be}$, $\tilde{\mathbf{Q}}_{bb}$, $\tilde{\mathbf{Q}}_{bc}$ and $\tilde{\mathbf{Q}}_{cb}$ by Block matrices containing rotational impedances.

Equation (2.104) represents a general model for the response of a panel based on the elemental approach. Step by step formulations to include fluid loading, feedback control force loops and arbitrary flexible boundaries have been derived. This framework allows for a variety of theoretical case studies that might prove useful in the prediction of the sound transmission through smart panels with well defined or fuzzy boundary conditions.

2.10 Stochastic excitation

For many practical vibro-acoustic problems it is not possible to describe the excitation in a deterministic way. For a range of common forms of disturbance stochastic formulations are available. These formulations define stochastic disturbances in terms of time and spaced averaged power and cross spectral density functions.

In this section it will be discussed how these cross and power spectral terms can be used within the framework of the element-based panel model that has been developed in the previous sections.

In particular three common models for stochastic excitations will be used, namely random uncorrelated rain on the roof, acoustic diffuse field and turbulent boundary layer (TBL) excitation.

2.10.1 Energy and power terms

As done for the deterministic plane acoustic wave excitation, the distributed field of the stochastic excitation is discretised into point forces located at the centres of the elements into which the panel has been divided. The cross spectral density $\tilde{\mathbf{S}}_{ee,i}$ of a stochastic force excitation incident on the panel can generally be calculated from

$$\tilde{\mathbf{S}}_{ee,i}(\omega) = \Phi_i \tilde{\mathbf{C}}_{ee}, \tag{2.106}$$

where Φ_i is the excitation power spectral density in terms of the mean square excitation force spectrum and $\tilde{\mathbf{C}}_{ee}$ is the spatial cross correlation matrix of the excitation forces for the plate element centre locations.

Note that the spatial correlation for the different possible types of disturbances might impose additional criteria for the spatial resolution in the elemental approach; for the calculation of the response and sound radiation of the panel. For predictions presented in this report the shortest bending wave length criterion is considered to be adequate. The influence of the spatial correlation of the excitation is not discussed in greater detail here. References [5] and [7] provide some discussion on the spatial correlation of acoustic diffuse field and TBL disturbance.

Kinetic energy spectral density of the panel

The power spectral density for the total kinetic energy of the panel can be calculated from the product of the panel element mobility matrix and the cross spectral density matrix of the excitation so that [7]

$$S_{EE}(\omega) = \frac{m_e}{2}\ trace\left(\tilde{\mathbf{Y}}_{ee}^{H}\tilde{\mathbf{S}}_{ee,i}\tilde{\mathbf{Y}}_{ee}\right). \tag{2.107}$$

Sound power radiation spectral density of the panel

The power spectral density of the total sound power radiated to the receiving side of the panel can be calculated from [7]

$$S_{PP}(\omega) = trace\left[\left(\tilde{\mathbf{Y}}_{ee}^{H}\tilde{\mathbf{S}}_{ee,i}\tilde{\mathbf{Y}}_{ee}\right)\tilde{\mathbf{R}}_{rad,r}\right]. \tag{2.108}$$

As practical note: Since we are only interested in the trace of the matrix product, the calculation can be speeded up using the following formulation

$$S_{PP}(\omega) = \sum\sum\left[\left(\tilde{\mathbf{Y}}_{ee}^{H}\tilde{\mathbf{S}}_{ee,i}\tilde{\mathbf{Y}}_{ee}\right).\tilde{\mathbf{R}}_{rad,r}^{T}\right], \tag{2.109}$$

where . denotes an element by element multiplication and the double sum represents

the total sum of all elements (columns and rows) of the resulting matrix of contributions to the radiated power.

2.10.2 Rain on the roof excitation

A rain on the roof disturbance is characterized by temporal and spatial uncorrected random point forces across the panel surface. Hence the spatial cross correlation is a delta function at $r = 0$. The spatial correlation is 1 for $r_{i,i}$ and zero otherwise. The excitation correlation matrix $\tilde{\mathbf{C}}_{ee}$ therefore has no off diagonal terms and takes the form of an $[N_e, N_e]$ identity matrix.

$$\mathbf{C}_{ee} = I_e \tag{2.110}$$

The power spectral density Φ_i can be described in terms of the variance of the random excitation forces on the panel over time

$$\Phi_i = \mathbf{var}\left[F_i(t, x, y)\right]. \tag{2.111}$$

In the case of single events (e.g. rain drops) the power spectral density of the disturbance is the average power spectral density of all events. Within this study a frequency independent, i.e. constant power spectral density with a unit magnitude has been considered, this either corresponds to an excitation via random white noise signals or via random idealized delta impulses.

2.10.3 Diffuse field excitation

Diffuse field excitation is a widely used model to describe the acoustic field in reverberant enclosures. The spatial correlation for an acoustic diffuse field excitation has been discussed by Shorter and Langley [24]. The spatial correlation function is given as a function of the absolute distance between two points on the panel

$$C(r_{i,j},\omega) = \frac{\sin\left(k_0 r_{i,j}\right)}{k_0 r_{i,j}}, \tag{2.112}$$

where k_0 is the wavenumber in the media on the source side of the panel and $r_{i,j}$ is the absolute distance between two points on the panel. As discussed in Section 2.3.2, the $sinc$ function takes a value of unity as r tends to zero. The correlation Matrix for the elemental approach can therefore be written as

$$\tilde{\mathbf{C}}_{ee} = \begin{bmatrix} 1 & \frac{\sin(k_0 r_{1,2})}{k_0 r_{1,2}} & \cdots & \frac{\sin\left(k_0 r_{1,N_e}\right)}{k_0 r_{1,N_e}} \\ \frac{\sin(k_0 r_{2,1})}{k_0 r_{2,1}} & 1 & \ddots & \vdots \\ \vdots & \ddots & \ddots & \vdots \\ \frac{\sin\left(k_0 r_{N_e,1}\right)}{k_0 r_{N_e,1}} & \cdots & \cdots & 1 \end{bmatrix}. \tag{2.113}$$

The power spectral density of the excitation forces on the elements is given as

$$\Phi_i(\omega) = 4E\left[\tilde{p}_{rev}\tilde{p}^*_{rev}\right] A_e^2 = 4\langle\overline{p^2_{rev}}\rangle A_e^2 \tag{2.114}$$

where $\langle\overline{p^2_{rev}}\rangle$ is the spatial and time averaged mean square pressure in the diffuse field on the source side of the partition and the factor four arises from the pressure doubling at a rigid surface and the relationship between pressure amplitude and mean square value.

2.10.4 Turbulent boundary layer excitation

Turbulent boundary layer excitations are typical for aircraft high speed train and automotive vehicles. The spatial correlation for turbulent boundary layer excitation has been discussed in references [5] and [7]. The most common expression for TBL cross correlation is given by Corcos [6]. The parameters that define the correlation structure of a fully developed TBL as used in this report are given in 2.4.

Table 2.4: Parameters for the Turbulent boundary layer excitation

Parameter	Symbol	Value	Unit
Free-stream velocity	U_∞	225	m/s
Convection velocity (Chase)	U_c	0.6 $\times U_\infty$	m/s
Mach number	M	0.66	–
–	α_x	1.2	–
–	α_y	0.8	–
Boundary layer thickens	δ	0.1	m
Mean wall shear stress	τ_w	55.13	N/m^2

The Correlation function for a TBL excitation in x and y direction is given as [6]

$$\tilde{C}(r_{x,i,j}, r_{y,i,j}, \omega) = e^{-\frac{|r_{x,i,j}|}{L_x(\omega)}} e^{-\frac{|r_{y,i,j}|}{L_y(\omega)}} e^{-j\frac{\omega r_{y,i,j}}{U_c}} \tag{2.115}$$

where $|r_{x,i,j}|$ and $|r_{y,i,j}|$ are the x and y components of the distance between two points on the panel and L_x and L_y are the correlation lengths in x and y direction given by

$$L_x(\omega) = \frac{\alpha_x U_c}{\omega}, \tag{2.116}$$

$$L_y(\omega) = \frac{\alpha_y U_c}{\omega}, \tag{2.117}$$

where α_x and α_y are empirical constants [5, 7] as defined in Table 2.4 and U_c is the convection velocity [6]. Elliott et al. [5] give an estimator model for the power spectral density for the pressure fluctuations across a rigid surface caused by an turbulent boundary layer,

$$\Phi_i(\omega) = \frac{\tau_w^2 \delta}{U_\tau} \frac{0.01\pi}{\left(1 + 0.02Sh(\omega)^{\frac{2}{3}}\right)} A_e^2, \tag{2.118}$$

where Sh is the Strouhal number given by

$$Sh(\omega) = \frac{\omega \delta}{U_\infty} \tag{2.119}$$

and the friction velocity U_τ is calculated from the square root of the ratio of mean wall shear stress and the density of the fluid

$$U_\tau = \sqrt{\frac{\tau_w}{\rho_0}}. \tag{2.120}$$

2.11 Summary

In this chapter a general element based model for the sound transmission through a thin rectangular panel has been developed. Subsequently this model has been extended to incorporate fluid loading, velocity feedback control forces and arbitrary flexible boundaries. For convenience the formulations have been cast in matrix expressions that allow an efficient numerical evaluation.

Formulations for deterministic and stochastic excitation models have been discussed and applied to the matrix formulations of the panel response and sound radiation.

The derived framework of formulations is quite flexible and allows the theoretical study of a wide range of panel and control system setups.

Chapter 3

Simulation Results

In this chapter the simulation results of systematic studies on the vibration response and sound transmission through a rectangular panel with sixteen decentralized velocity feedback control loops, predicted from the model developed in Chapter 2 are presented. The following issues are addressed and discussed with respect to the passive and active sound transmission effects:

- variation of the gain in the velocity feedback loops and spatial distribution of the control loops across the panel;
- consideration of symmetric and asymmetric fluid loading on source and receiving side of the panel;
- arbitrary flexible panel boundaries;
- response to the three stochastic excitations models described in Section 2.10;

The panel parameters for the panel used in this study are defined in Table 2.1. The assumed properties of air are given in Table 2.2, further definitions of the model parameters used are referenced or stated in the corresponding sections.

3.1 Control parameters

In this section the effect of the feedback control gain on the control performance is discussed. Results for two different spatial distributions of 16 feedback control loops with

collocated point forces and velocity sensors are presented. The distribution of the control loops is shown in Figure 3.1, where a) is identical to that considered by Gardonio and Elliott [1]. Results for a second case with alternative spatial control force distribution, shown in Figure 3.1 b), are also presented. It will be shown that the control force distribution has a significant effect on the control performance at low frequencies. If a wider range of frequencies is considered no significant difference in the overall performance is observed.

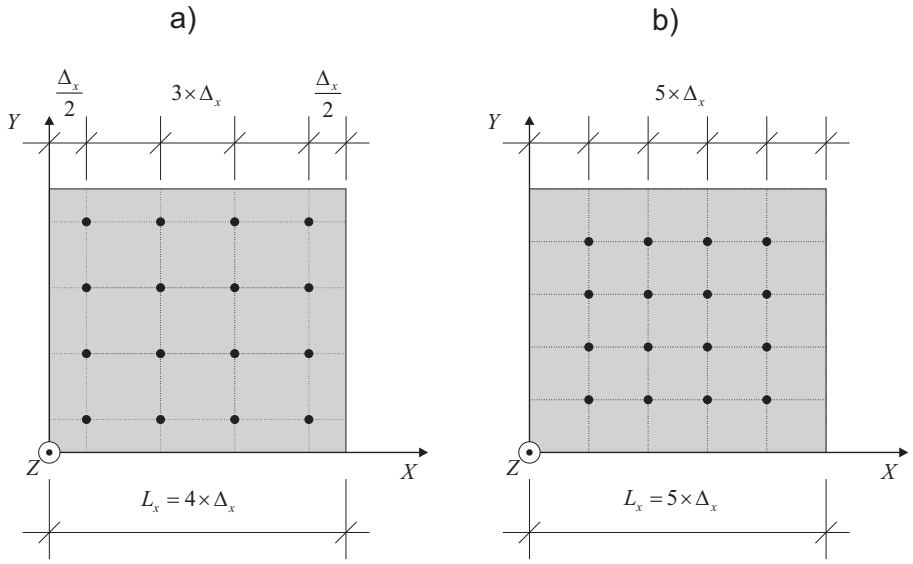

Figure 3.1: Spatial distribution of control loops across the panel; a): $(\Delta/2, \Delta, \Delta/2)$ distribution on the left and b): uniform (Δ, Δ, Δ) distribution on the right.

Within this study an all side pinned panel has been considered. The surrounding fluid on source and receiving side of the panel is modelled using the physical parameters of air at normal ambient temperature. Fluid loading back forces are not considered. The panel kinetic energy and sound transmission coefficient are calculated for a plane acoustic wave with a 1 Pa pressure amplitude, incident at an angle $\theta = 45°$ and $\varphi = 45°$ (see definition in Section 2.3). The element resolution has been chosen to meet the criterion of at least 2 elements per highest mode order in x and y direction. A systematic study discussing appropriate spatial resolution and dynamic and residual mode range is presented in Appendix A.

Figure 3.2 shows the spectra of predicted panel kinetic energy and transmission coefficient for a $(\Delta/2, \Delta, \Delta/2)$ configuration of the control loops (Figure 3.1 a). Gardonio and Elliott [1] present identical results but only observe frequencies up to 1 kHz. They already

discuss that the achievable control performance largely depends on the applied velocity feedback gain.

The upper two graphs in Figure 3.2 shows the panel kinetic energy and sound transmission coefficient for a passive panel without control and for a range of control gains up to a maximum gain of 10^6. It can be seen that velocity feedback gains up to an optimal level introduce damping to all panel modes. Further increase in the feedback gain results in a situation where the control forces actually pin the panel locally, this completely cancels low order panel modes but introduces new undamped modes at higher frequencies. Gardonio and Elliott [1] present this phenomena for predictions on a plate with active control loops, the authors also investigated this phenomena in greater detail for a beam system with a single velocity feedback control unit [25].

The bottom graph in Figure 3.2 shows the overall reduction achieved in panel kinetic energy and radiated sound power for a range of velocity feedback gains from 10^{-3} to 10^6. The results for the frequency range 0.1 Hz to 1 kHz and 0.1 Hz and 5 kHz are presented. The reduction in total kinetic energy and radiated sound power is calculated from the ratio of the integrated spectra with and without control,

$$Reduction = 10log_{10}\left(\frac{\int_{f_{low}}^{f_{up}} Spectra\ \ with\ \ control}{\int_{f_{low}}^{f_{up}} Spectra\ \ without\ \ control}\right) \quad [dB] \tag{3.1}$$

where the integration across the frequency range is obtained using the trapezoidal integration rule [14] on the discrete spectra. For both frequency ranges the reduction achieved in the panel kinetic energy and radiated sound power is increasing with increasing control gain, reaching an optimal level at a control gain of about 40. For further increase of the control gain less improvement is achieved. Above a control gain of about 10^4 the reduction converges to a constant level. For control gains above 10^3 an increase of radiated sound power above the levels of the uncontrolled panel is predicted. The comparison between the two considered frequency ranges shows that the predicted reduction in the 1 kHz range tends to be up to 4 dB higher than for the 5 kHz range. For high feedback gains the overall radiated sound power for both spectra converge to the same value, the estimated reduction for the panel kinetic energy shows comparable characteristics but is about 1 dB higher for the 1 kHz frequency range estimate.

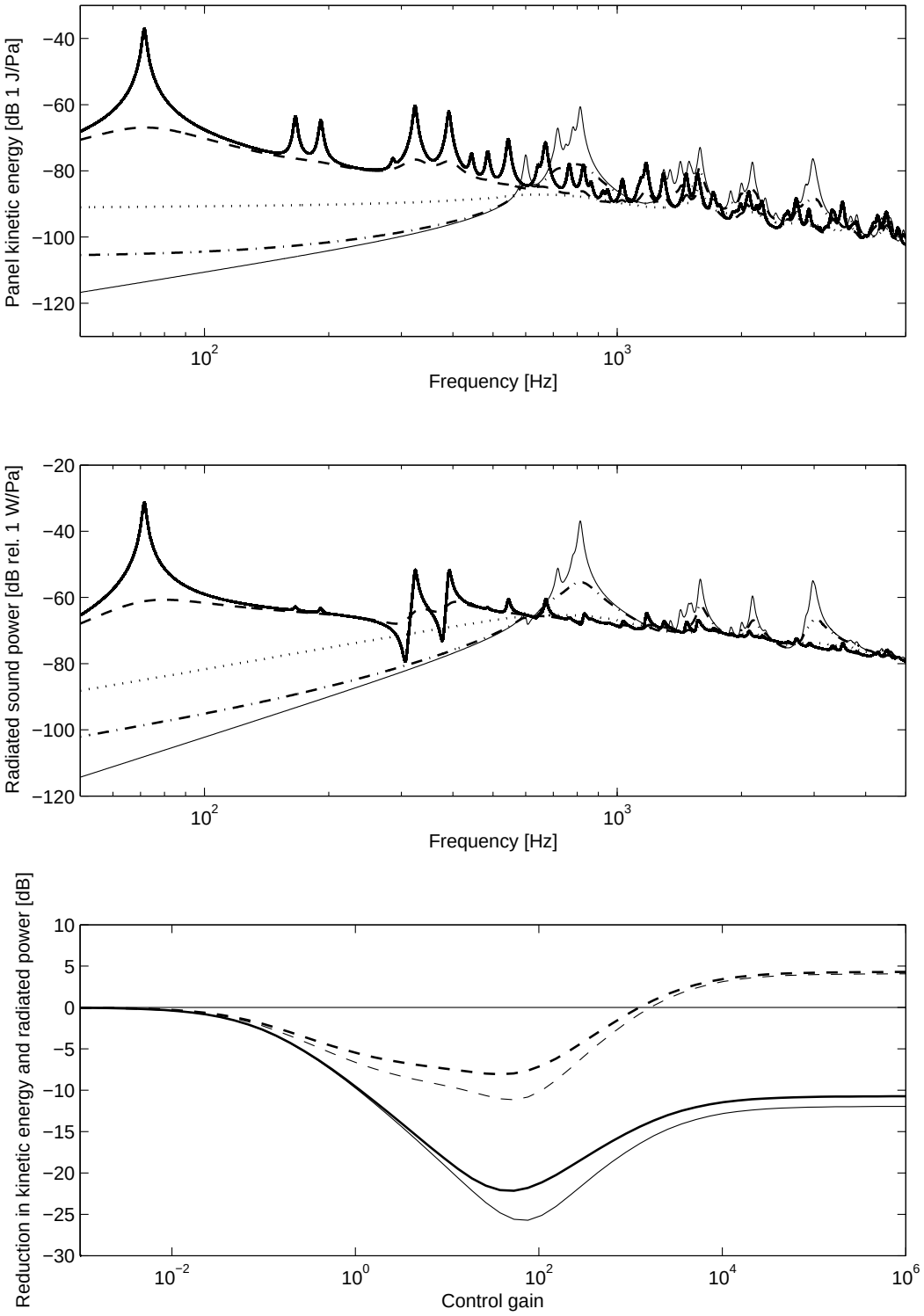

Figure 3.2: Panel kinetic energy (top graph) and transmission coefficient (middle graph) for a panel with $(\Delta/2, \Delta, \Delta/2)$ velocity feedback loop distribution. No control ($solid$), a feedback gain of 3 ($dashed$), an optimal velocity feedback gain of 40 ($dotted$), a gain of 310 ($dash-dotted$) and a 'maximum' feedback gain of 10^6 ($faint$). Achieved reductions (bottom graph) in panel kinetic energy ($solid$) and radiated sound power ($dashed$) for the frequency range between 0.1 Hz 5 kHz ($thick$) and between 0.1 and 1 kHz ($faint$).

The top two graphs in Figures 3.3 show the predicted spectra of kinetic energy and transmission coefficient for a (Δ, Δ, Δ) distribution of the velocity feedback loops (Figure 3.1 b) for a range of velocity feedback gains. This configuration generally shows comparable behaviour as seen for the $(\Delta/2, \Delta, \Delta/2)$ control distribution before. It is interesting to note though that this configuration is more effective in suppressing low order modes. The altered modes for high feedback gains appear at higher frequencies. This results in a better performance of this control point distribution at low frequencies.

The bottom graph in Figure 3.3 shows the overall reduction achieved in the panel kinetic energy and radiated sound power for a range of velocity feedback gains from 10^{-3} to 10^{6}. As before results for a frequency range from 0.1 Hz up to 1 kHz and 0.1 Hz to 5 kHz are presented. For both frequency ranges the achieved reduction in the panel kinetic energy and radiated power is increasing with increasing control gain, reaching an optimal level at a control gain of about 40. The results for the 5 kHz frequency range show similar characteristic as the corresponding results for the $(\Delta/2, \Delta, \Delta/2)$ control point distribution. However, the estimation of the reduction for the 1 kHz frequency range shows quite a different result. An optimal reduction is achieved for roughly the same level of control gain, but for further increase of feedback gain, the control performance does not decrease significantly. This is because most of the altered panel modes due to the pinning effect at the control points predominantly produces new resonances above the 1 kHz frequency range.

This is due to the fact that, as can be deduced from Figure 3.1, the pinning effect produced by the $(\Delta/2, \Delta, \Delta/2)$ configuration divides the panel into rectangular sections whose area are relatively larger then those sections produced by the (Δ, Δ, Δ) control loop distribution.

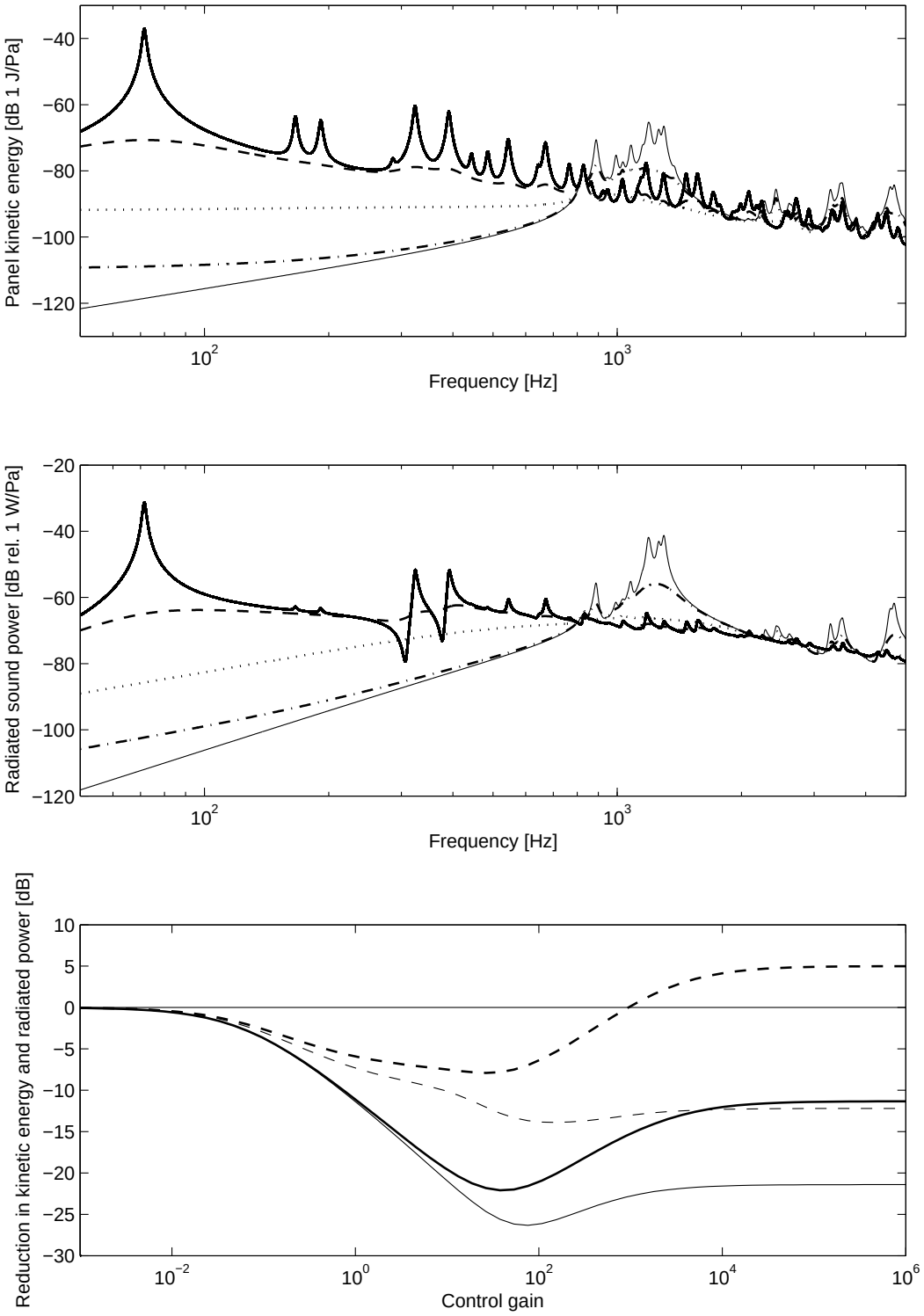

Figure 3.3: Panel kinetic energy (top graph) and transmission coefficient (middle graph) for a panel with (Δ, Δ, Δ) velocity feedback loop distribution. No control $(solid)$, a feedback gain of 3 $(dashed)$, an optimal velocity feedback gain of 40 $(dotted)$, a gain of 310 $(dash - dotted)$ and a 'maximum' feedback gain of 10^6 $(faint)$. Achieved reductions (bottom graph) in panel kinetic energy $(solid)$ and radiated sound power $(dashed)$ for the frequency range between 0.1 Hz 5 kHz $(thick)$ and between 0.1 and 1 kHz $(faint)$.

However, if the observed frequency range is increased these modes are included in the estimation of the control performance. Figure 3.4 shows that there is only a small difference in the overall control performance for the two observed control point distributions if the complete frequency range from 0.1 Hz to 5 kHz is considered. For a further increase in the observed frequency range one might expect the two control loop distributions to show an even more similar overall performance.

When considering these results, one should bear in mind that to date practical sensor actuator loops operate in regions below the predicted optimal gain. This is mainly caused by stability limitation due to imperfect sensor actuator collocation and the response of the controller used [12], chapter 9. Optimisation of the feedback gain for various configurations of sensor-actuator feedback loops is a region of high research interest.

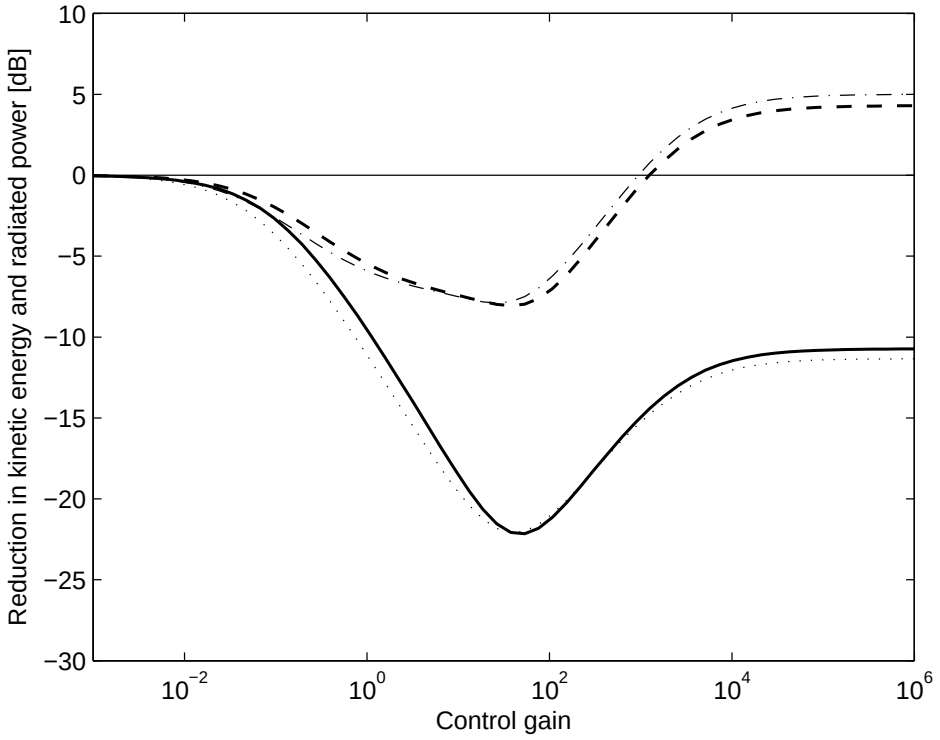

Figure 3.4: Comparison of the overall reduction in total kinetic energy and radiated sound power for a $(\Delta/2, \Delta, \Delta/2)$ and (Δ, Δ, Δ) feedback loop configuration in the frequency range from 0.1 Hz to 5 kHz. $(\Delta/2, \Delta, \Delta/2)$ configuration: Reduction in kinetic energy $(solid)$ and radiated sound power $(dashed)$. (Δ, Δ, Δ) configuration: Reduction in kinetic energy $(dotted)$ and radiated sound power $(dash - dotted)$.

3.2 Fluid loaded panel

In this section the results of a study on the fluid loading effects on the panel are presented and discussed. Homogeneous and mixed cases of fluid loading on the source and receiving side of the panel have been considered. The dynamic fluid parameters are taken as those for air and water at normal ambient temperature. This is because both fluids are quite common media in engineering applications and possess significantly different dynamic behaviour. The results show that fluid coupled models solely considering air loading do not exhibit much differences to simulations obtained with a weakly coupled model. However models comprising water loading on either one or both sides of the panel show significant differences in terms of resulting natural panel frequencies and the magnitude of the predicted panel kinetic energy and radiated sound power spectra.

Throughout this section an all side pinned panel under an acoustic plane wave excitation with a 1 Pa pressure amplitude, incident at an angle $\theta = 45°$ and $\varphi = 45°$ (see definition in Section 2.3) was considered. The results are evaluated using the final formulations from Section 2.4 and 2.6. The results for panel kinetic energy and transmission coefficient for fluid loaded and unloaded panel without control, and for a panel with 16 discrete $(\Delta/2, \Delta, \Delta/2)$ distributed idealized velocity feedback loops, with a feedback gain of 10^2 (high control performance) and 10^6 (pinned condition) are compared. In addition the control performance of the fluid loaded panel models for a range of control gains from 10^{-3} to 10^6 are studied. The assumed acoustical parameters for air are given in Table 2.2. The assumed acoustical parameters for water are given in Table 3.1.

Table 3.1: Acoustical parameters for water

Parameter	Symbol	Value	Unit
Speed of sound	c_0	1483	m/s
Density	ρ_0	998.2	kg/m^3
Specific impedance	$Z_0 = c_0\rho_0$	14.8×10^5	Ns/m^3

3.2.1 Identical Fluid on source and receiving side

First the two homogeneous cases of identical fluids on both sides of the panel i.e. air to air and water to water are considered.

Air to air

The case of air to air transmission is the classic sound transmission situation as encountered in many acoustic engineering applications. Figure 3.5 and 3.6 show the predicted panel kinetic energy and transmission coefficient for a panel with and without considering fluid loading. The comparison of the two cases show only minor differences i.e. a small shift of the panel modes towards lower frequencies and a slight reduction in the magnitude of the resonance peaks. This indicates that the reactive fluid loading forces primarily act as a distributed mass loading on the panel and also seem to introduce a small amount of damping. Almost no frequency shift and change in magnitude can be seen for the optimal control case since all modes are highly damped due to the applied velocity feedback control.

The top two graphs in Figure 3.7 show the resulting panel kinetic energy and transmission coefficient for a passive panel, a panel with the 'optimal' velocity feedback gain and a 'maximum' velocity feedback gain of 10^6. The bottom graph shows the achieved reduction in panel kinetic energy and radiated sound power for a velocity feedback gain range form 10^{-3} to 10^6. It can be seen that the optimal velocity feedback gain (defined by maximum reduction in kinetic energy) is achieved for a velocity feedback gain of about 40. These results are very similar to those presented for the uncoupled panel in Section 3.1 Figure 3.2. The increase in panel kinetic energy and radiated sound power for velocity feedback levels above 10^3 are predicted to be less then those in the uncoupled case.

Water to water

The case of water to water transmission is not an uncommon engineering situation, in this study it is used as an example for the loading forces created by a liquid fluid. The dynamic properties of air and water are quite different as the density of water is about three orders of magnitude higher than that of air and the wave speed is more than four times higher. Non linear effects due to incompressibility of water have not been considered.

Figure 3.8 and 3.9 show the predicted kinetic panel energy and transmission coefficient with and without considering fluid loading. Both Figures show a significant effect of fluid loading forces on the resulting spectra. As already identified for the air to air coupled

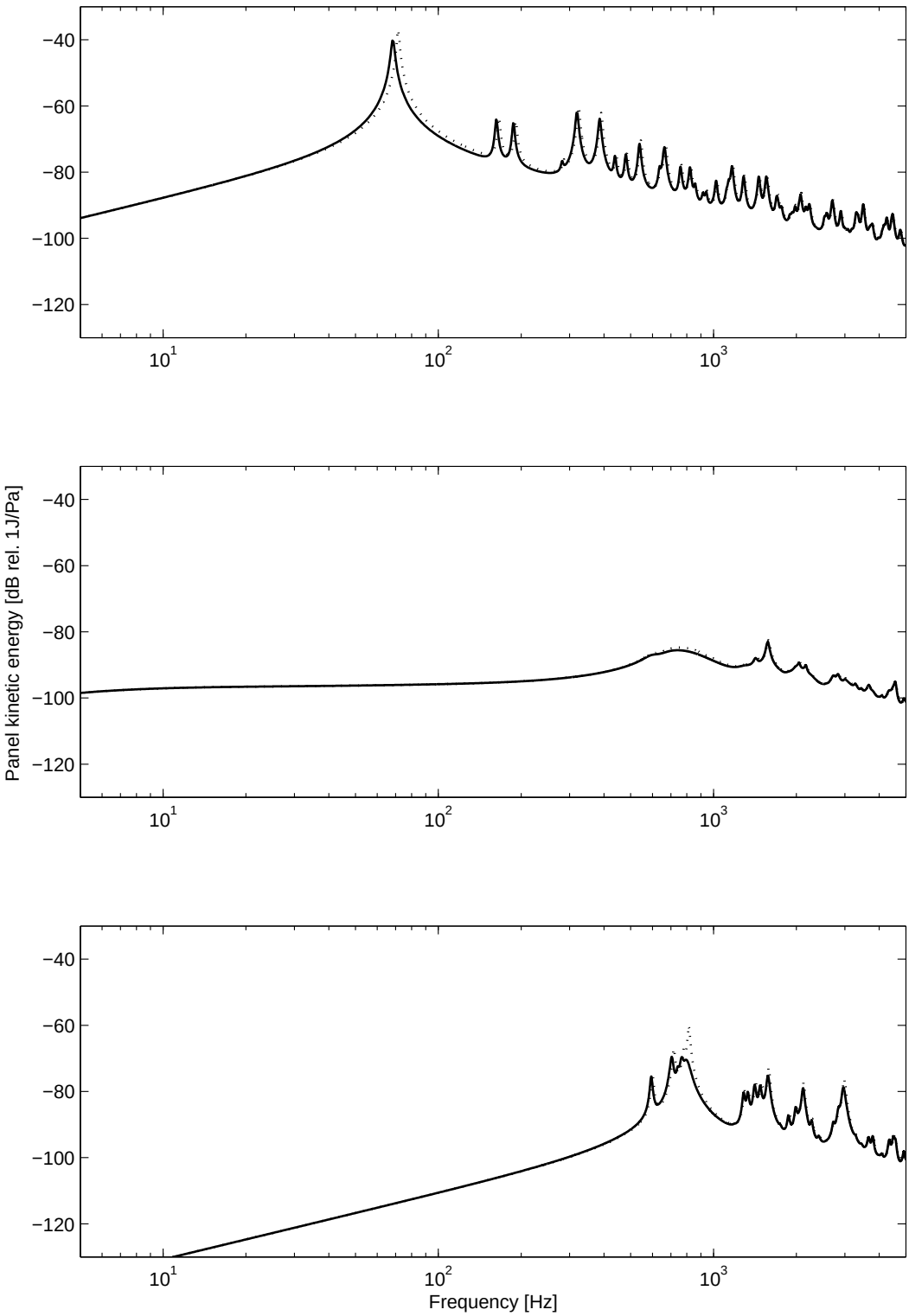

Figure 3.5: Panel kinetic energy normalized to the pressure amplitude of an acoustic plane wave for the case of AIR on the source and receiver side of the panel. No control (top graph) velocity feedback gain of 10^2 (middle graph) and feedback gain of 10^6 (bottom graph). Considering fluid loading ($solid$) and without considering fluid loading ($dotted$).

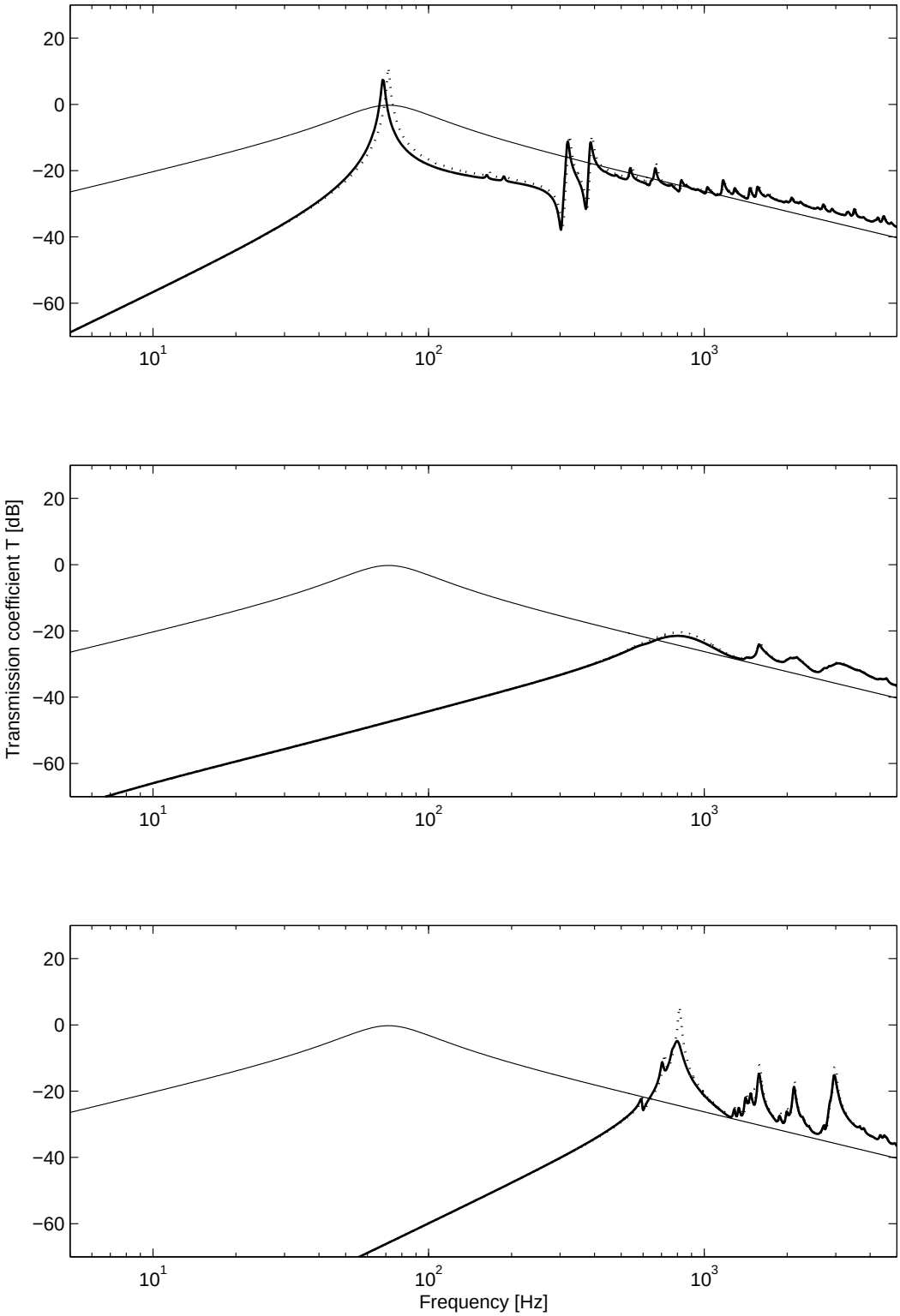

Figure 3.6: Transmission coefficient of panel plane excited by an acoustic plane wave for the case of AIR on the source and receiver side. No control (top) velocity feedback gain of 10^2 (middle) and feedback gain of 10^6 (bottom). Considering fluid loading ($solid$) and without considering fluid loading ($dotted$); transmission coefficient for normal incidence according to Equation (2.37) ($faint$).

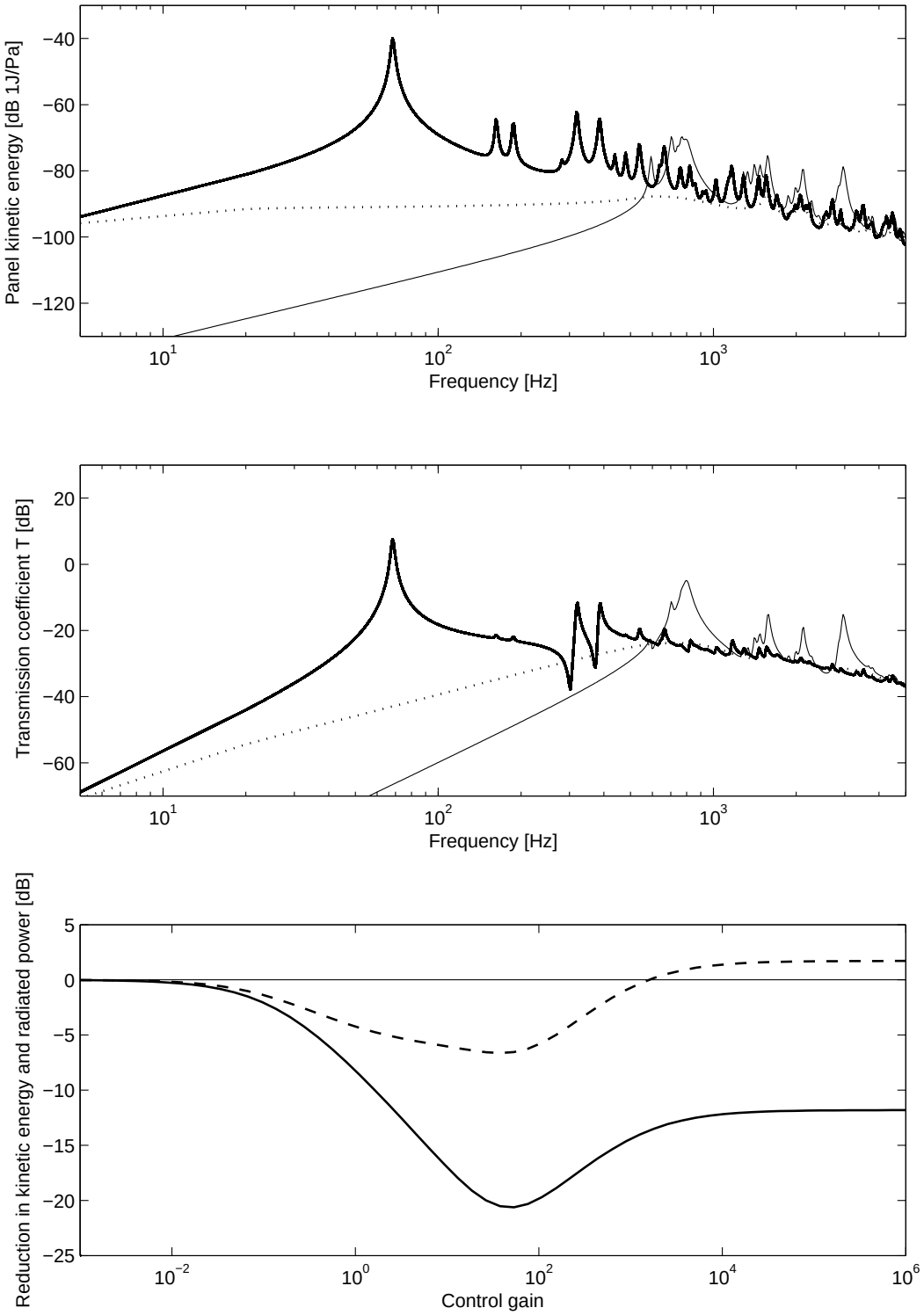

Figure 3.7: Panel kinetic energy, transmission coefficient and achieved reductions of an AIR to AIR fluid loaded panel under plane wave excitation for a range of velocity feedback gains between 10^-3 and 10^6. Panel kinetic energy (top graph) Transmission coefficient (mid graph), no control ($solid$) optimal control($dotted$) max control (10^6) ($faint$) and achieved reduction (bottom graph) in total panel kinetic energy ($solid$)and total radiated sound power ($dashed$).

case, the fluid loading forces predominantly act as distributed mass loading. Due to the hig specific impedance of water this effect is far more significant than in the air to air transmission case. The first natural frequency of the panel is shifted down from 71.5 Hz to 8.3 Hz all higher order modes are also shifted towards lower frequencies.

Differences in the spectral characteristics between the uncoupled air to air and uncoupled water to water case arise from the different values for the wavenumber k_0 in the two media, which affects the formulation for the spatial distribution of the excitation forces in Equation (2.19) i.e. Equations (2.16) and (2.17).

Figure 3.8 shows that the additional mass loading effect causes an overall reduction of the panel kinetic energy for all three considered control gain settings. The predicted transmission coefficient in Figure 3.9 indicates that the overall transmission coefficient above the first few panel modes tends towards 0 dB i.e. to a value of unity, indicating that the panel does not represent an effective sound barrier under water. The results for the uncoupled spectrum indicate a transmission coefficient much higher than unity for all frequencies above 10 Hz. This is physically not plausible and indicates that the consideration of fluid loading is important if fluids with high specific impedance are considered.

The top two graphs in Figure 3.10 show the resulting panel kinetic energy and transmission coefficient for a passive panel, a panel with 'optimal' velocity feedback gain and a 'maximum' velocity feedback gain of 10^6. The bottom graph shows the achieved reduction in panel kinetic energy and radiated sound power for a velocity feedback gain range form 10^-3 to 10^6. It can be seen that the optimal control (defined by maximum reduction in kinetic energy) is achieved for a velocity feedback gain of about 300. In comparison to the uncoupled and weak air to air coupling case this is an significant shift. Almost no reduction in the radiated sound power is achieved, above a feedback gain of about 10^4 a slight increase in radiated sound power is predicted.

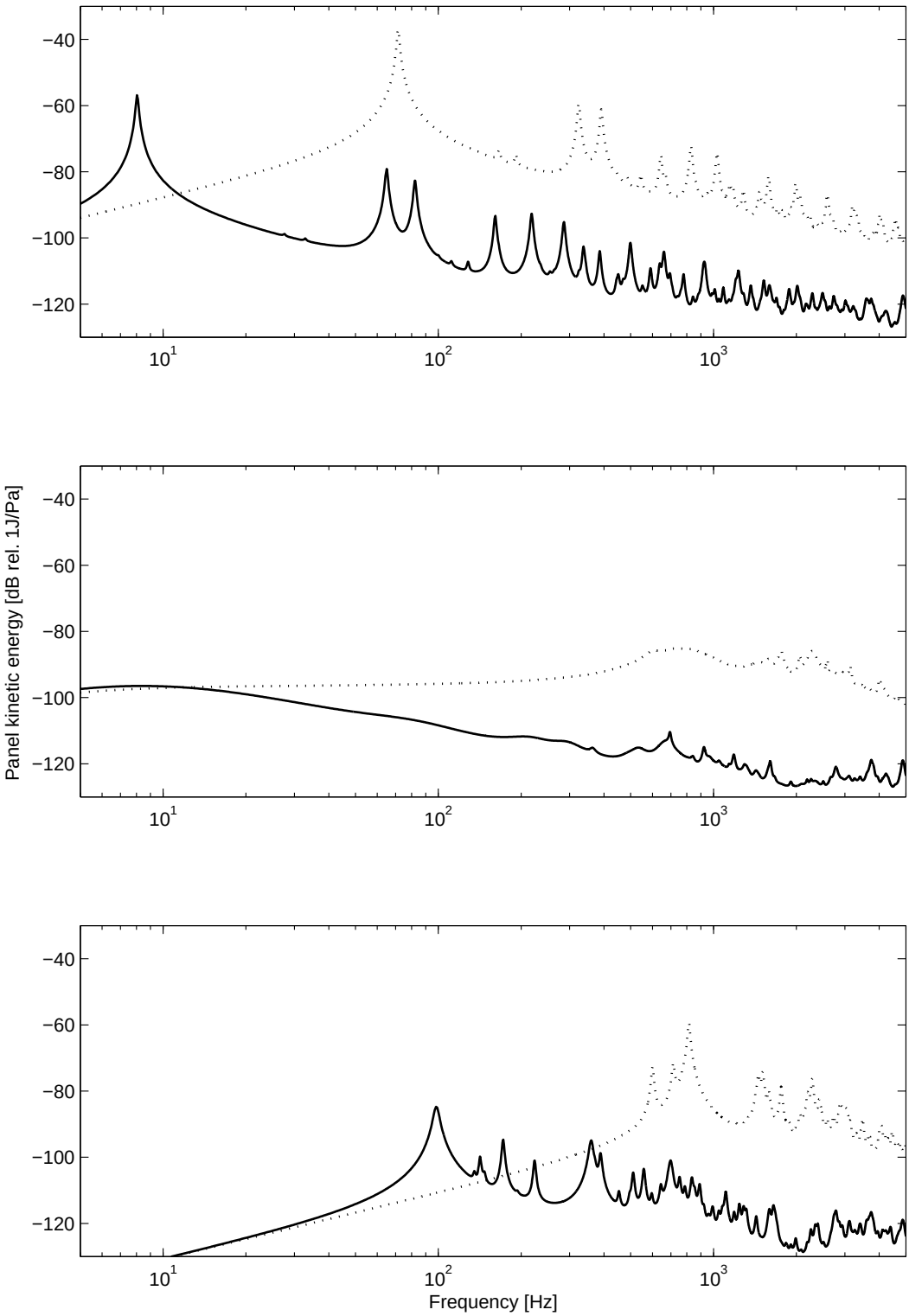

Figure 3.8: Panel kinetic energy normalized to the pressure amplitude of an acoustic plane wave for the case of WATER on the source and receiver side of the panel. No control (top) velocity feedback gain of 10^2 (middle) and feedback gain of 10^6 (bottom). Considering fluid loading $(solid)$ and without considering fluid loading $(dotted)$.

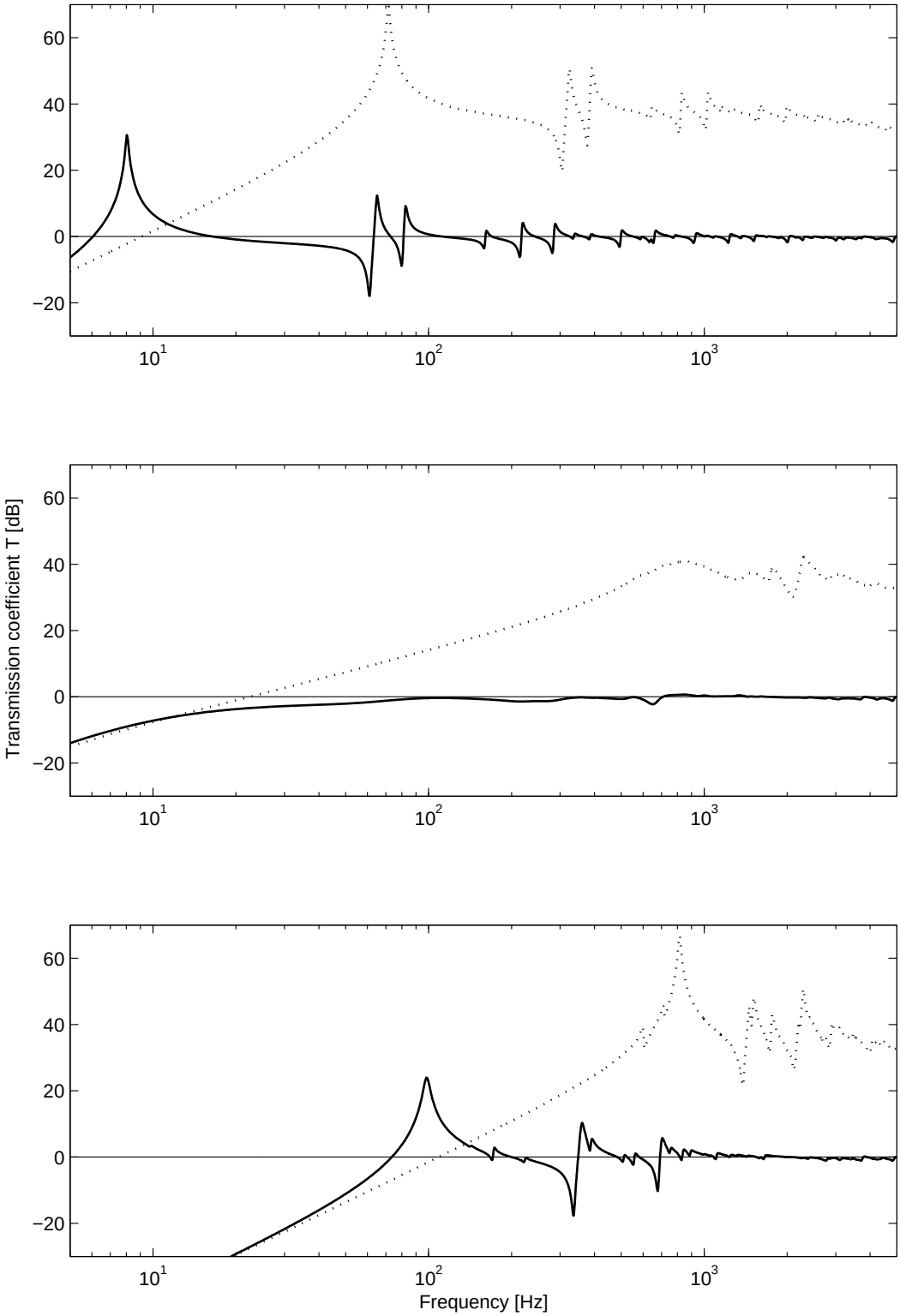

Figure 3.9: Transmission coefficient of panel plane excited by an acoustic plane wave for the case of WATER on the source and receiver side. No control (top) velocity feedback gain of 10^2 (middle) and feedback gain of 10^6 (bottom). Considering fluid loading ($solid$) and without considering fluid loading ($dotted$); transmission coefficient for normal incidence according to Equation (2.37) ($faint$).

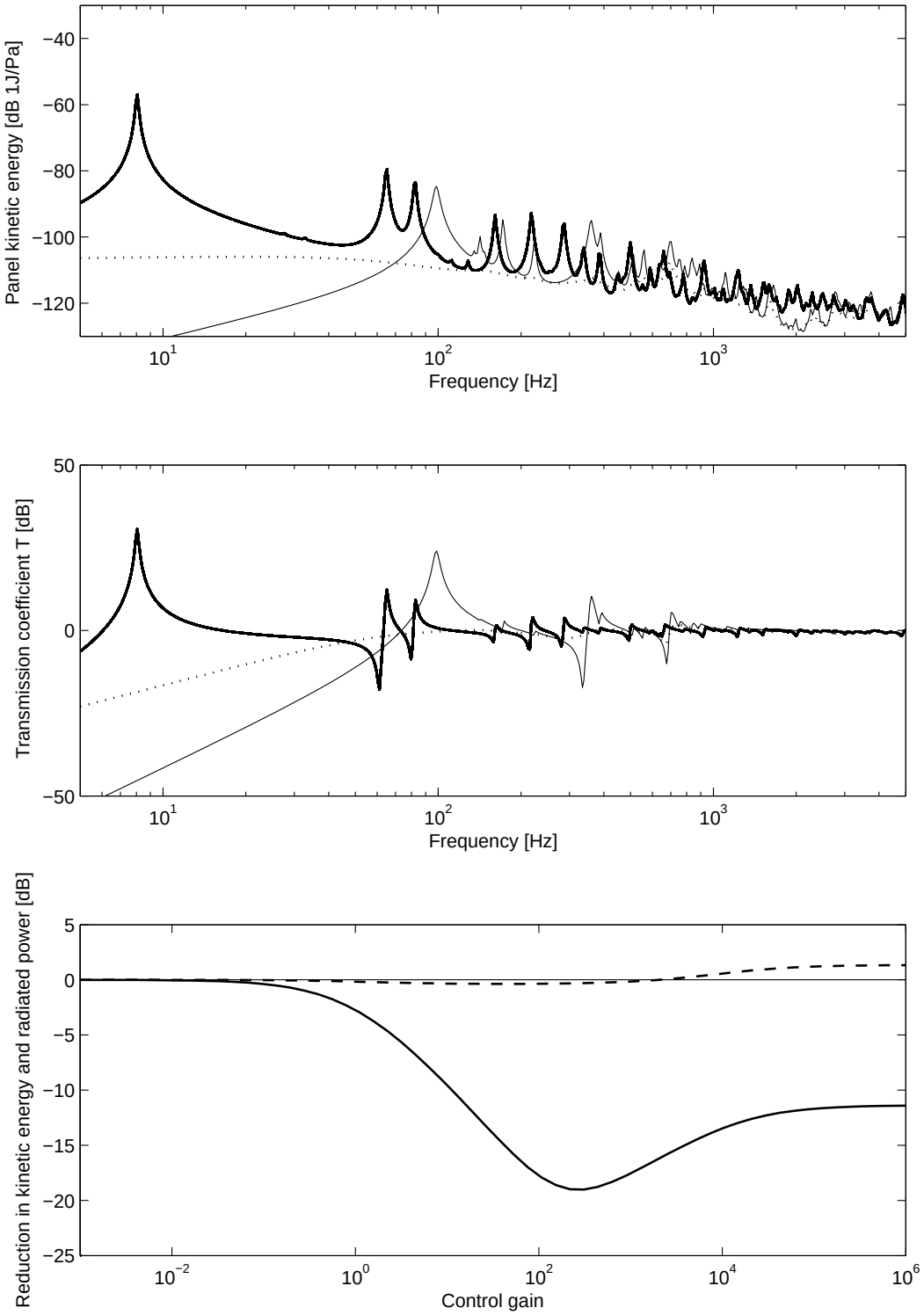

Figure 3.10: Panel kinetic energy, transmission coefficient and achieved reductions of a WATER to WATER fluid loaded panel under plane wave excitation for a range of velocity feedback gains between 10^-3 and 10^6. Panel kinetic energy (top graph) Transmission coefficient (mid graph), no control ($solid$) optimal control ($dotted$) max control (10^6) ($faint$) and achieved reduction (bottom graph) in total panel kinetic energy ($solid$)and total radiated sound power ($dashed$).

3.2.2 Different fluid on source and receiving side

For completeness asymmetric fluid loading cases, represented by the case of water to air and air to water transmission are considered.

Water to Air

Figure 3.11 and 3.12 show the predicted panel kinetic energy and radiated sound power for the case of water on the excitation side and air on the radiating side of the panel, with and without considering fluid loading. As for the case of water to water transmission, both figures show a significant difference between the results with and without consideration of fluid back forces. Since the panel is only loaded with water on one side the additional mass effect is less significant and the first natural frequency of the panel is only shifted down from 71.5 Hz to 11.6 Hz, a trend also seen for all higher order modes.

Figure 3.11 shows that the additional mass loading effect causes an overall reduction in panel kinetic panel energy for all three considered velocity feedback gains. Similarly Figure 3.12 shows that the predicted transmission coefficients considering fluid loading in are much lower than those without. With exception for the fundamental panel resonance, the transmission coefficient in the fluid loaded case is lower than 0 dB.

For a very light panel (low impedance compared to surrounding fluid) the sound transmission coefficient is dominated by the impedance difference between the fluid on the source and receiving side. For the combination water to air and vice versa this leads to a theoretical transmission coefficient for normal incidence of $T(0) \approx -29.5$ dB [16]. The results in Figure 3.12 show that the predicted transmission is significantly higher; this will be further discussed later in this section.

The top two graphs in Figure 3.13 show the resulting panel kinetic energy and transmission coefficient for a passive panel, a panel with 'optimal' velocity feedback gain and a 'maximum' velocity feedback gain of 10^6. The bottom graph shows the achieved reduction in panel kinetic energy and radiated sound power for a velocity feedback gain range form 10^{-3} to 10^6. It can be seen that the optimal control is achieved for a velocity feedback gain of about 200. This indicates that the optimal velocity feedback gain is increasing with increasing fluid loading, which also means that control settings might need

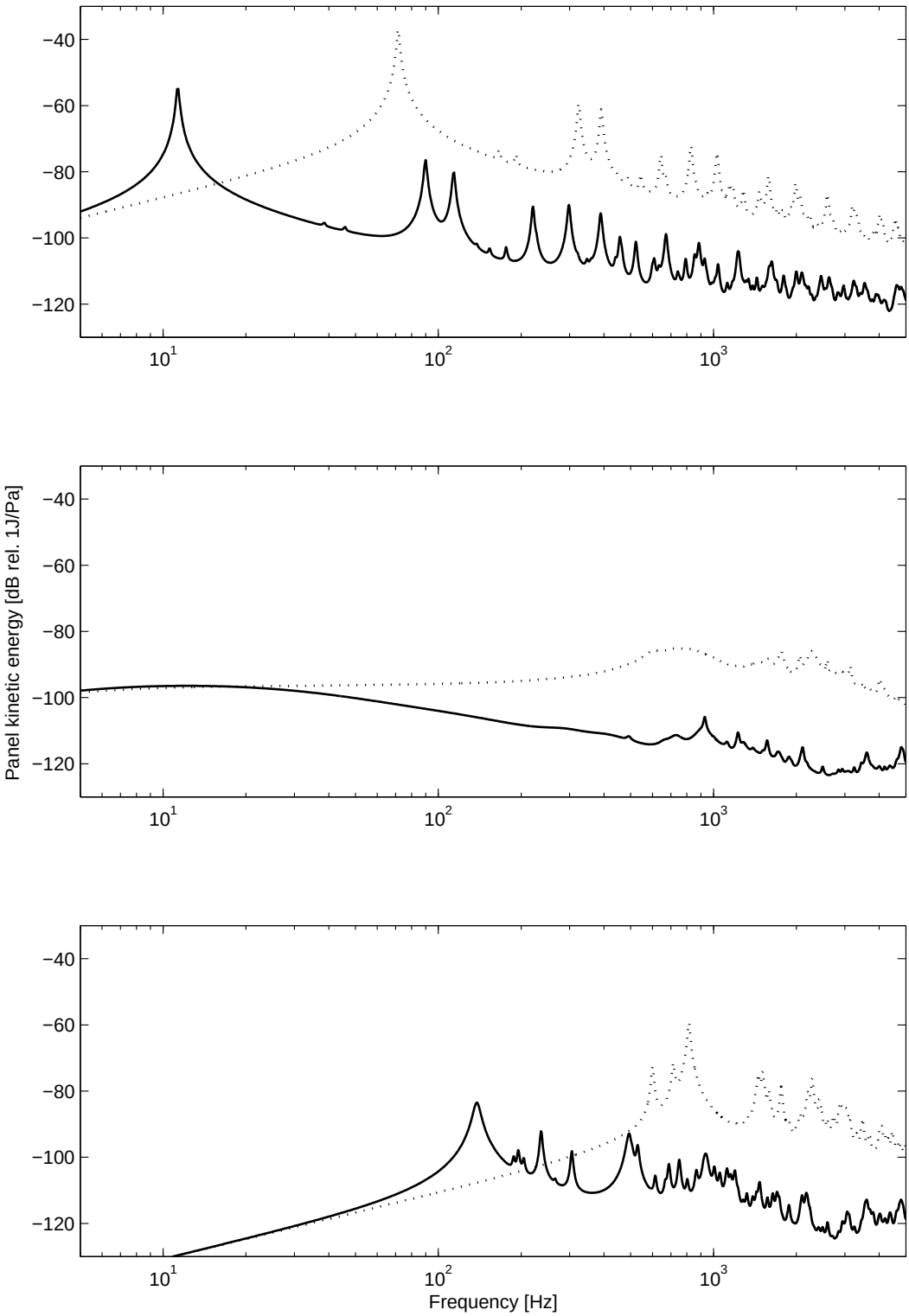

Figure 3.11: Panel kinetic energy normalized to the pressure amplitude of an acoustic plane wave for the case of WATER on the source and AIR on the receiver side of the panel. No control (top) velocity feedback gain of 10^2 (middle) and feedback gain of 10^6 (bottom). Considering fluid loading $(solid)$ and without considering fluid loading $(dotted)$.

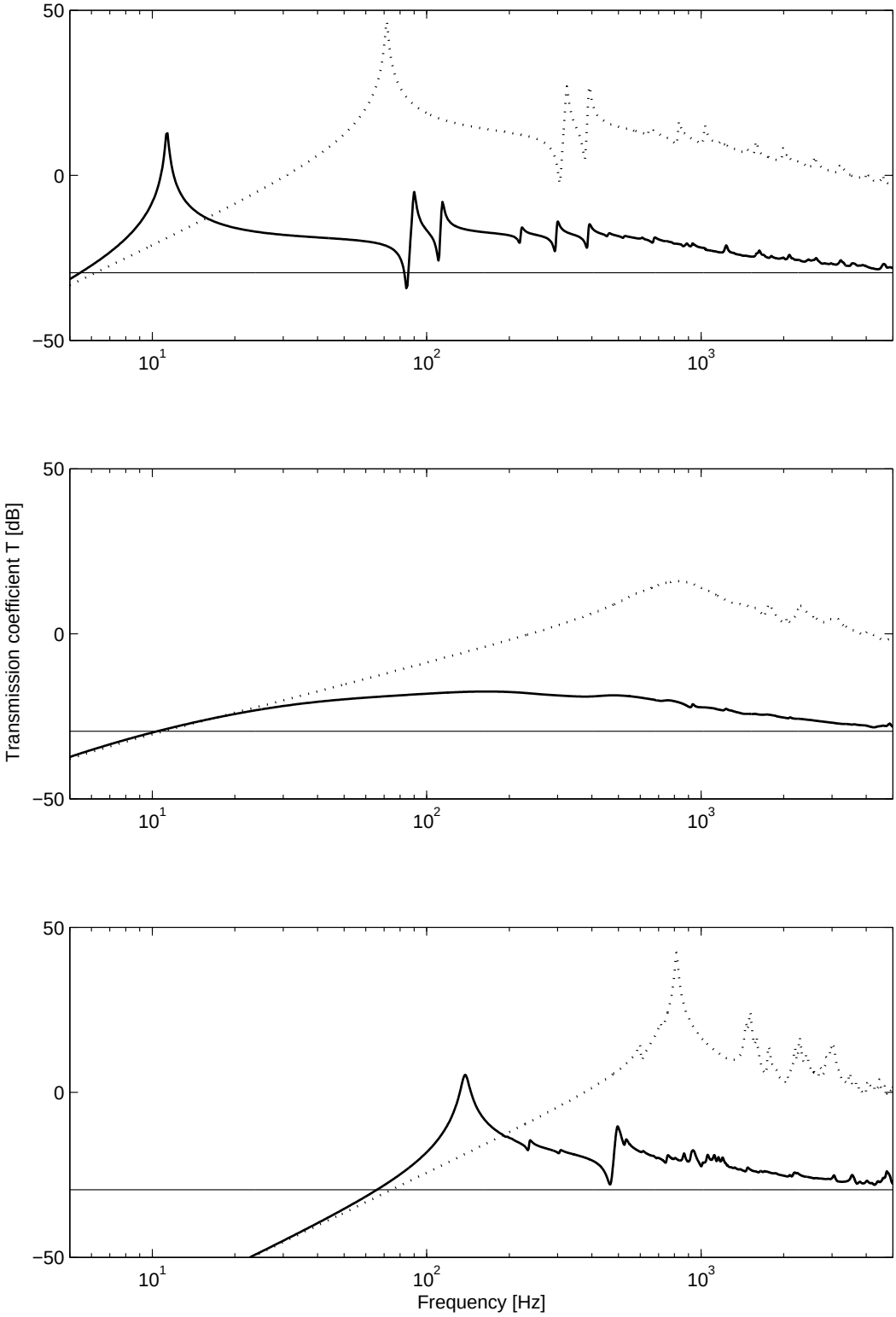

Figure 3.12: Transmission coefficient of panel plane excited by an acoustic plane wave for the case of WATER on the source and AIR on the receiver side. No control (top) velocity feedback gain of 10^2 (middle) and feedback gain of 10^6 (bottom). Considering fluid loading $(solid)$ and without considering fluid loading $(dotted)$; transmission coefficient for normal incidence according to Equation (2.37) $(faint)$.

to adapt to changes in the surrounding fluid. Only a modest reductions in the predicted radiated sound power of about -2 dB are achieved.

Air to water

Figure 3.14 and 3.15 show the predicted kinetic panel energy and transmission coefficient for a panel with air on the excitation side and water on the radiating side for the cases with and without considering fluid loading. Generally similar trends as for the water to air transmission case can be observed. The shift of the fundamental panel frequency from 71.5 Hz to 11.6 Hz is identical to that for the air to water loading, showing that the applied total loading is actually the same. The predicted panel kinetic energy spectra show similar characteristics for both transmission directions. The predicted transmission coefficient for the air to water transmission tends to be 12.7 dB lower than that predicted for water to air transmission. The predicted results for air to water transmission seem to tend to the value of -29.5 [16], given by the impedance mismatch between air and water. Above above 1 kHz the transmission coefficient for all three observed velocity feedback gain cases drops more rapidly than for the transmission coefficient for the water to air transmission case in Figure 3.12. A direct comparison between the two mixed air/water coupled cases is presented and discussed later in this section.

The top two graphs in Figure 3.16 show the resulting panel kinetic energy and transmission coefficient for a passive panel, a panel with 'optimal' velocity feedback gain and a 'maximum' velocity feedback gain of 10^6. The bottom graph shows the achieved reduction in panel kinetic energy and radiated sound power for a velocity feedback gain range form 10^{-3} to 10^6. It can be seen that the optimal control is achieved for a slightly lower velocity feedback gain than for the water to air transmission case in Figure 3.13. The achieved maximum control is about -15 dB and therefore about 4 dB less then in the water to air case. However, the predicted optimal reduction in radiated sound power is -2.5 dB and therefore slightly higher than for the water to air radiation case.

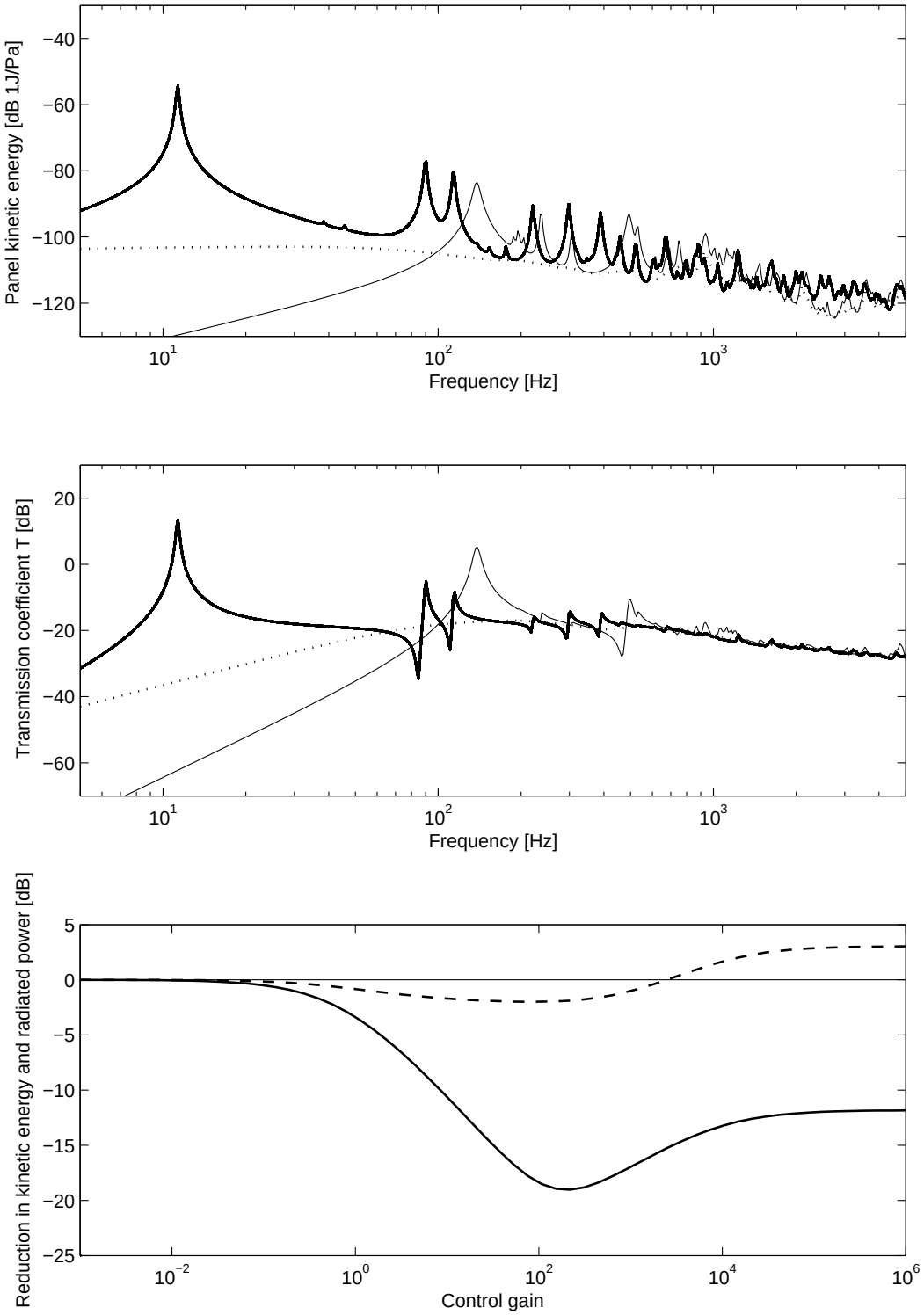

Figure 3.13: Panel kinetic energy, transmission coefficient and achieved reductions of a WATER to AIR fluid loaded panel under plane wave excitation for a range of velocity feedback gains between 10^-3 and 10^6. Panel kinetic energy (top graph) Transmission coefficient (mid graph), no control ($solid$) optimal control($dotted$) max control (10^6) ($faint$) and achieved reduction (bottom graph) in total panel kinetic energy ($solid$)and total radiated sound power ($dashed$).

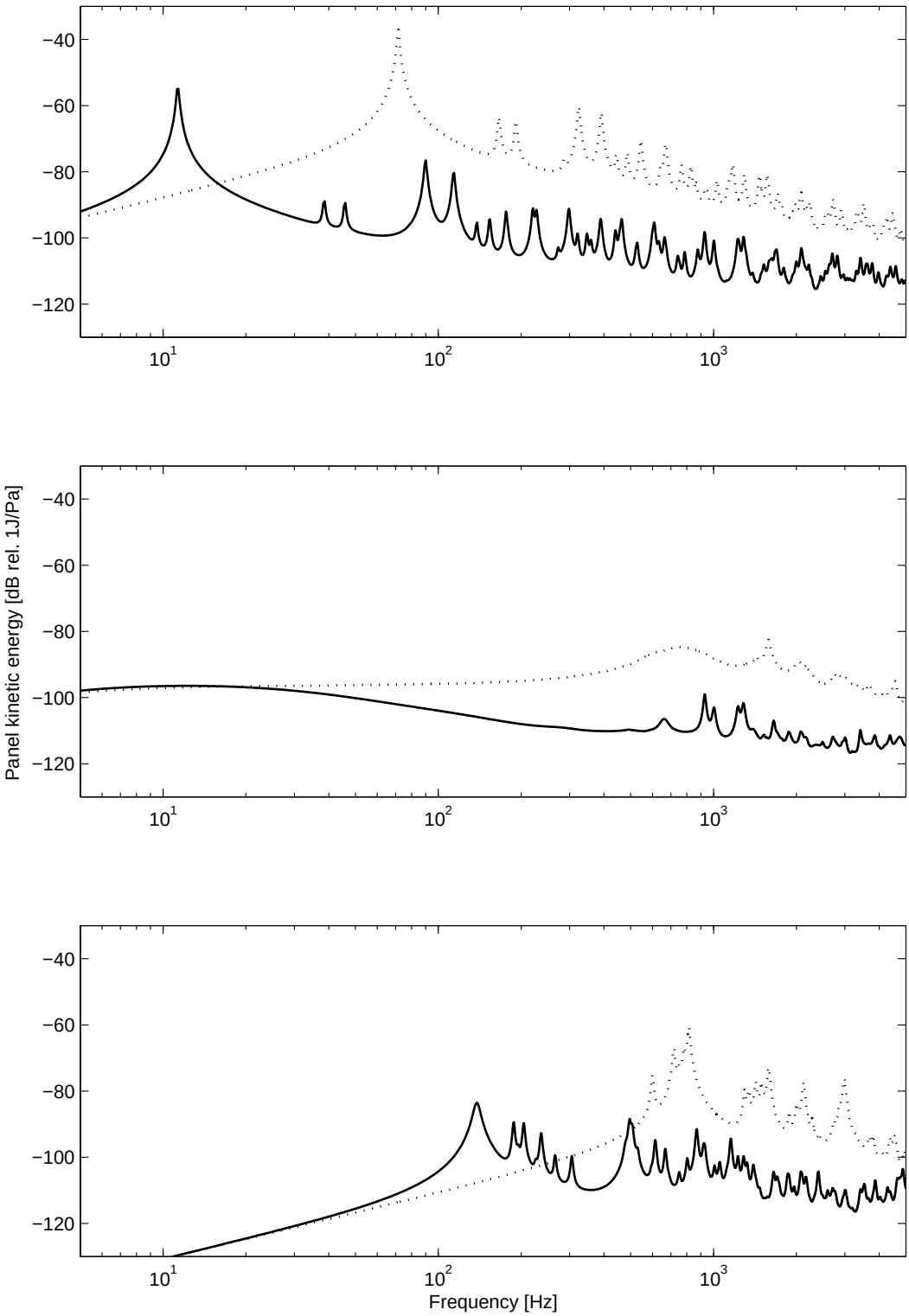

Figure 3.14: Panel kinetic energy normalized to the pressure amplitude of an acoustic plane wave for the case of AIR on the source and WATER on the receiver side of the panel. No control (top) velocity feedback gain of 10^2 (middle) and feedback gain of 10^6 (bottom). Considering fluid loading $(solid)$ and without considering fluid loading $(dotted)$.

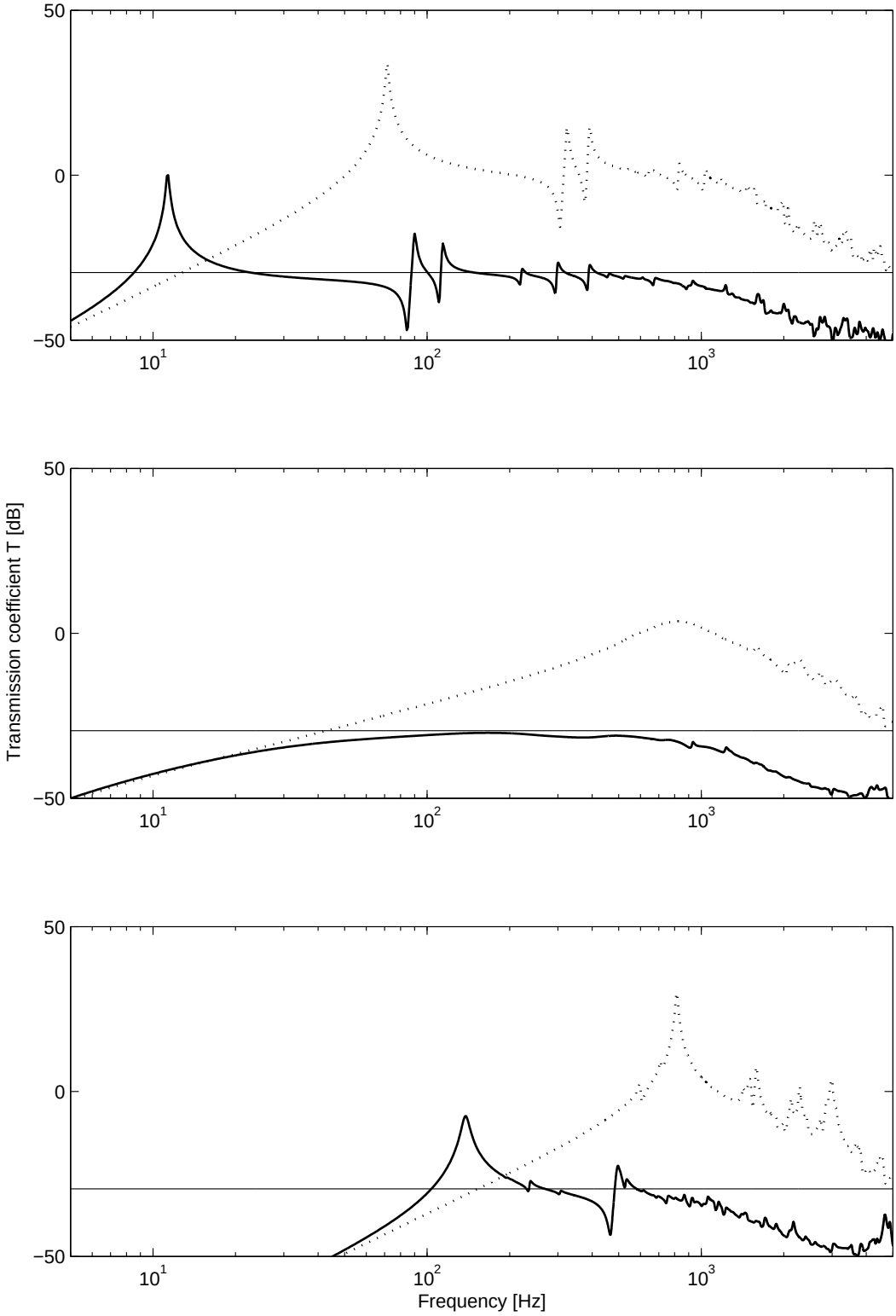

Figure 3.15: Transmission coefficient of panel plane excited by an acoustic plane wave for the case of AIR on the source and WATER on the receiver side. No control (top) velocity feedback gain of 10^2 (middle) and feedback gain of 10^6 (bottom). Considering fluid loading ($solid$) and without considering fluid loading ($dotted$); transmission coefficient for normal incidence according to Equation (2.37) ($faint$).

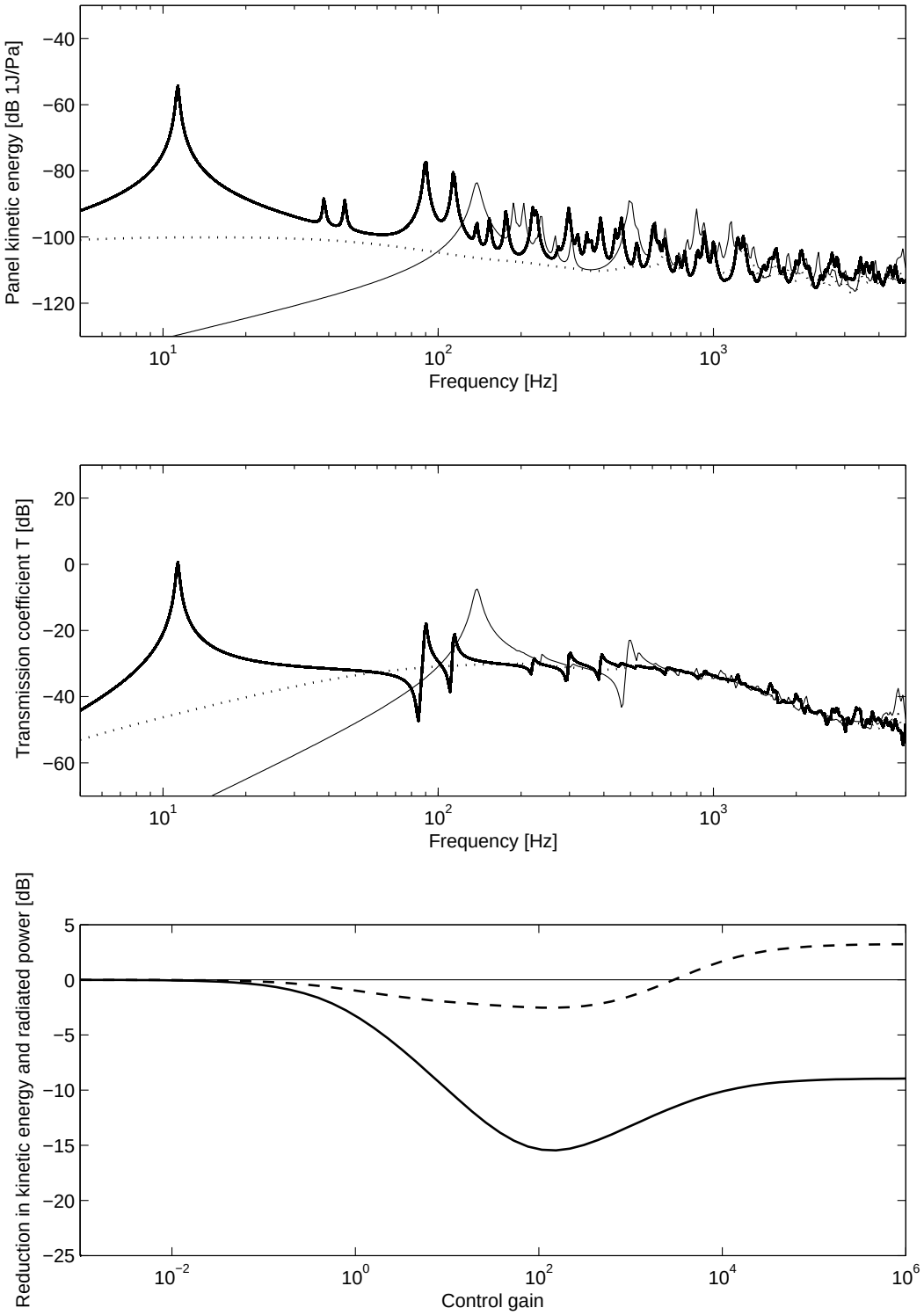

Figure 3.16: Panel kinetic energy, transmission coefficient and achieved reductions of a AIR to WATER fluid loaded panel under plane wave excitation for a range of velocity feedback gains between 10^-3 and 10^6. Panel kinetic energy (top graph) Transmission coefficient (mid graph), no control ($solid$) optimal control ($dotted$) max control (10^6) ($faint$) and achieved reduction (bottom graph) in total panel kinetic energy ($solid$)and total radiated sound power ($dashed$).

Comparison between air to water and water to air sound transmission

From the top graph in Figure 3.17 it can be seen that there are some differences in the panel kinetic energy spectra between the water to air and air to water transmission case. It is assumed that this arises from the different values for the wavenumber k_0 in the two media, which affects the formulation for the spatial distribution of the excitation forces in Equation (2.19) i.e. Equations (2.16) and (2.17). These however only affects the magnitude of the resonance but not the natural frequencies of the panel. Both spectra show a good general agreement in terms of modal resonances, for frequencies above 1 kHz the panel kinetic energy spectra for the air to water transmission case tends to be higher than for the water to air transmission case. Possibly this is due to the wavelength in air becoming comparable to the panel dimensions. This, however has not been further investigated within this study.

From the comparison of the radiated sound power in the middle graph of Figure 3.17 it can be seen that the radiated sound power for the air to water coupling case is about 23 dB higher than in the water to air coupling case. The excitation pressures, i.e. forces in both case are identical and the panel kinetic energy in both cases are very similar. This indicates that the panel mean squared velocities are comparable. Reason for the difference in the the radiated sound power is hence due to the difference in the radiation resistance matrix $\mathbf{R}_{rad}$. From Equation (2.31) and (2.45) it can be seen that the the radiation resistance is proportional to the ratio between the fluid's density ρ_0 and the fluid's specific speed of sound c_0

$$R_{rad} \simeq \frac{\rho_0}{c_0}. \tag{3.2}$$

The difference in the radiated sound power in both fluid loading cases is therefore given by the ratio

$$\frac{R_{rad,W}}{R_{rad,A}} = \frac{\rho_{0,W} c_{0,A}}{c_{0,W} \rho_{0,A}} = 22.8\ [dB]. \tag{3.3}$$

The Comparison of the sound transmission coefficient in the bottom graph of Figure 3.17 shows that the transmission coefficient in the water to air coupling case is about 12.7 dB

higher than in the the air to water coupling case. This can be explained by the difference in the sound power of the incident acoustic wave on the receiving side of the panel. From Equation (2.33) it can be seen that the incident power is proportional to one over the specific impedance of the fluid on the source side of the panel

$$P_i \simeq \frac{1}{Z_0}. \tag{3.4}$$

The difference in incident sound power in both cases is therefore given by the ratio

$$\frac{P_{i,A}}{P_{i,W}} = \frac{\rho_{0,A} c_{0,A}}{\rho_{0,W} c_{0,W}} = -35.5\ [dB]. \tag{3.5}$$

The difference in the transmission coefficients is hence the ratio between the the squared sound speeds of air and water

$$\frac{c_{0,A}^2}{c_{0,W}^2} = -12.7\ [dB] \qquad = 22.8\ [dB] - 35.5\ [dB]. \tag{3.6}$$

Besides the 12.7 dB offset, the spectra for the radiated sound power and the transmission coefficient in Figure 3.17 show similar characteristics up to 1 kHz. Above 1 kHz the sound power and transmission coefficient spectra for the air to water transmission case are dropping more rapidly than for the water to air transmission case. This is possibly due to the wave length in air becoming comparable to the panel dimension.

The focus of this study is active control of sound transmission through panels coupled to fluids with low specific impedance. Therefore phenomena due to loading by fluids with high specific impedance has not been investigated in greater detail.

Summary

In this section the results of a study on the effect of back forces due to fluid loading on the panel have been presented. Homogeneous and mixed cases of fluid loading on the source and receiving side of the panel have been considered. The fluid properties of air and water have been considered because both are common media in engineering application and possess significantly different dynamic behaviour.

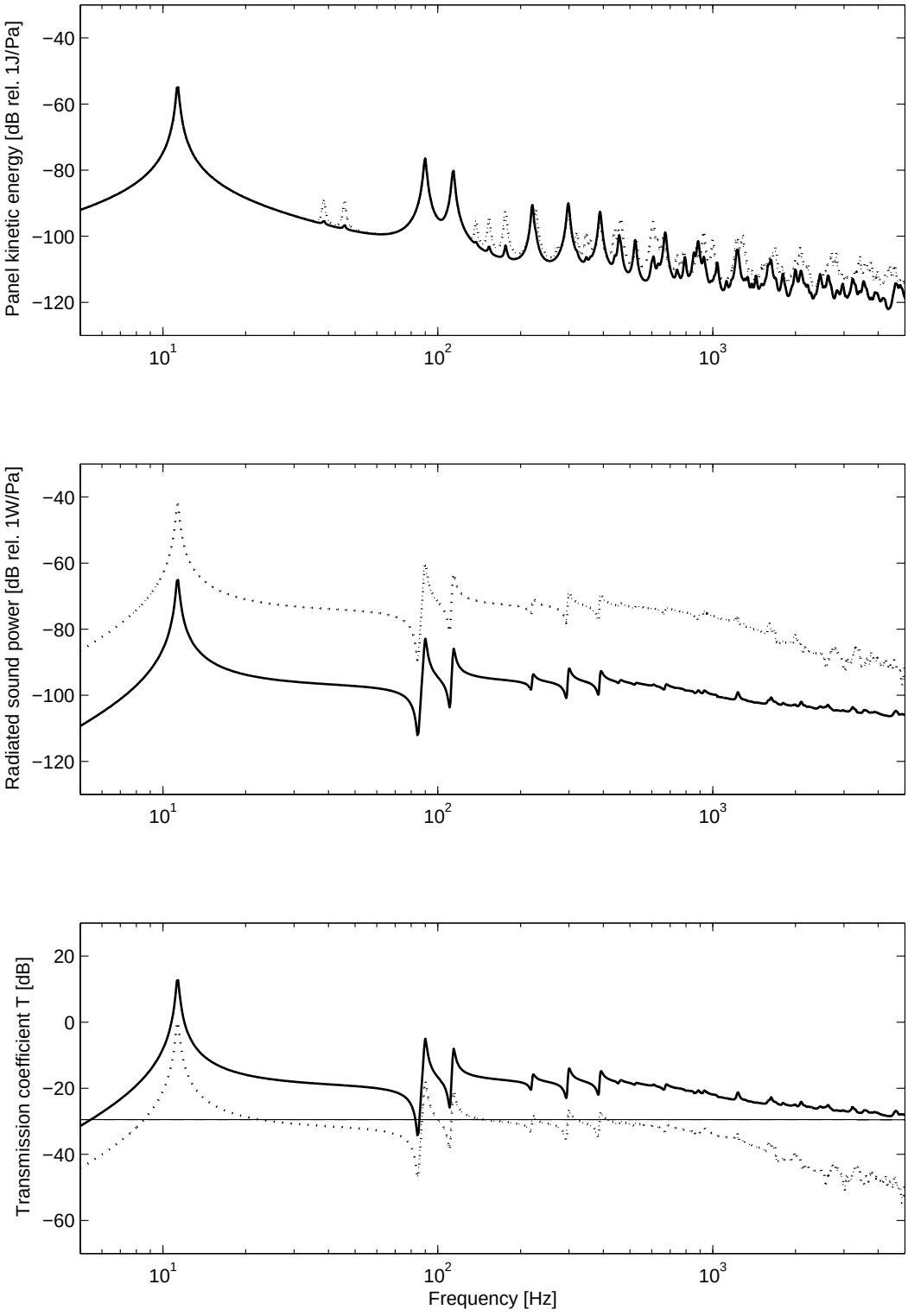

Figure 3.17: Comparison of the panel kinetic energy (top graph), radiated sound power (middle graph) and the transmission coefficient (bottom graph) of a fluid loaded panel under plane wave excitation in the case of WATER to AIR ($solid$) and AIR to WATER coupling ($dashed$)

It has been demonstrated that fluid back forces on the source and radiating side of the panel have a direct effect on the structural response. The developed prediction model from Section 2.4 and 2.6 yields physically feasible results and therefore seems to correctly capture the effect of fluid loading on source and radiating side of a panel.

The predictions show that fluid coupled models solely considering air loading on both sides of the panel do not exhibit much differences to simulations for an uncoupled (weakly coupled) panel model. However models comprising water loading on either or both sides of the panel show significant differences in terms of resulting panel natural frequencies and the magnitude of the predicted panel kinetic energy and sound transmission coefficient.

The effect of fluid loading back forces was found to be predominantly that of added distributed mass, hence the natural frequencies of the panel shift down in frequency. The results for the air to air transmission case also suggested that fluid loading introduces a small amount of distributed damping.

The change in achievable reduction in panel kinetic energy and radiated sound power with increasing velocity feedback gain for all observed fluid coupled cases show a single control optimum, where the optimal velocity feedback gain was found to increase with increasing fluid loading.

The predicted transmission coefficients for the symmetric fluid coupling cases show a good agreement with the approximated results for a normal incident wave from Equation (2.37). For the asymmetric cases certain agreement with the approximated results was achieved for the air to water sound transmission case. The transmission coefficient for the water to air transmission case is predicted to be 12.7 dB higher which corresponds to the ratio of the squared acoustic wave speeds in the two media.

This study is predominantly focused on cases of air to air transmission cases. The results of this section show that the effect of such low impedance fluid coupling is relatively small and might be neglected for further studies. It might however be interesting to investigate how small changes in air density and acoustic wave speed on either one or both sides of the panel, as they occur for an aircraft flying at different altitudes, might effect the control performance.

3.3 Flexible boundary conditions

The formulations derived in Section 2.7 and 2.8 allow for modelling a panel with arbitrary flexible boundaries. In this section the control effects produced by the sixteen channels decentralised velocity feedback loops on panels with enforced pinned and clamped boundary conditions are compared. Enforced boundaries are achieved by applying very high reactive boundary damping terms, to suppress all vertical and / or rotational motion along the panel edges. An additional case with intermediate flexible vertical and rotational springs is presented to demonstrate the possibility to simulate arbitrary intermediate boundaries.

For this study the panel kinetic energy and transmission coefficient are evaluated using the final formulations from Sections 2.4 and 2.6. Throughout this section a plane acoustic wave excitation with a 1 Pa pressure amplitude, incident at an angle $\theta = 45^\circ$ and $\varphi = 45^\circ$ (see definition in Section 2.3) is applied. The results for the passive panel, and the panel with 16 discrete $(\Delta/2, \Delta, \Delta/2)$ distributed idealized velocity feedback control loops, with a feedback gain of 40 (optimal) and 10^6 (maximum gain, pinned condition) are presented. The spatial resolution of the boundary locations is set to be at least 1.5 times the element resolution giving a minimum of 6 elements per shortest bending wave length. This was found to be sufficient to model line connected boundaries. The used distribution of boundary forces (and moments) is shown in Figure 3.18.

3.3.1 Pinned boundary conditions

Figures 3.19 and 3.20 show the simulated results for the kinetic panel energy and transmission coefficient for a plane acoustic wave excitation. The cases of a panel with all sides pinned and that of an initially completely free panel [11] with enforced boundary conditions are compared. Each boundary point is modelled as a passive linear damper with a damping coefficient of $b = 10^{12}$ Nsm^{-1} (simulating rigid boundaries).

The results for both cases show a good overall agreement. The most significant difference is the shift of the fundamental panel frequency from 71.5 Hz to 63.4 Hz which is a relative error of 11.3% This is probably due to the approximation of the natural frequencies and natural modes of the free panel derived by Warburton [11] using a Rayleigh-Ritz approx-

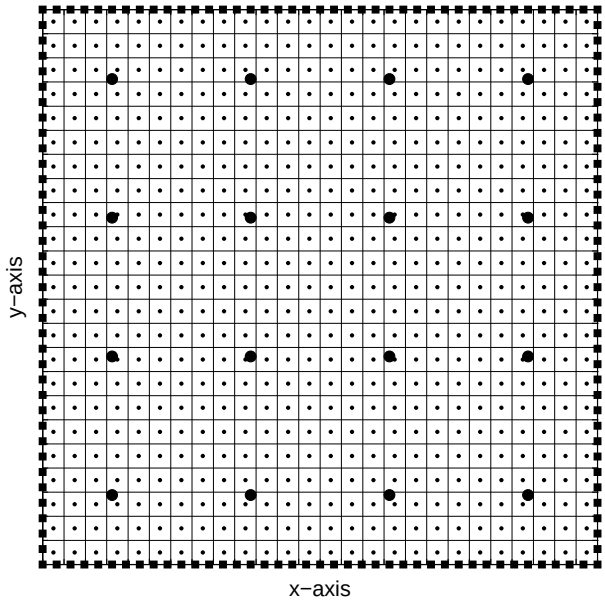

Figure 3.18: Spatial distribution of panel elements ($dots$), control positions ($circles$) and boundary locations along the panel edges ($sqares$)

imation approach. With increasing frequency the relative shift in the natural frequencies is decreasing. A further increase in the number of discrete boundary feedback forces did not cause a significant difference in the frequency response around the first resonance; a systematic study to yield a minimum resolution for the boundary forces needs yet to be conducted.

The top two graphs in Figure 3.21 show the resulting panel kinetic energy and transmission coefficient for the initially complectly free panel with enforced pinned boundary conditions without control, an 'optimal' velocity feedback gain and a 'maximum' velocity feedback gain of 10^6. The bottom graph shows the achieved reduction in panel kinetic energy and radiated sound power for a velocity feedback gain range form 10^{-3} to 10^6. It can be seen that the optimal control is achieved a for a velocity feedback gain of about 40 which corresponds well with the results achieved for a pinned panel using analytical solutions for mode shapes and natural frequencies presented in Figure 3.2.

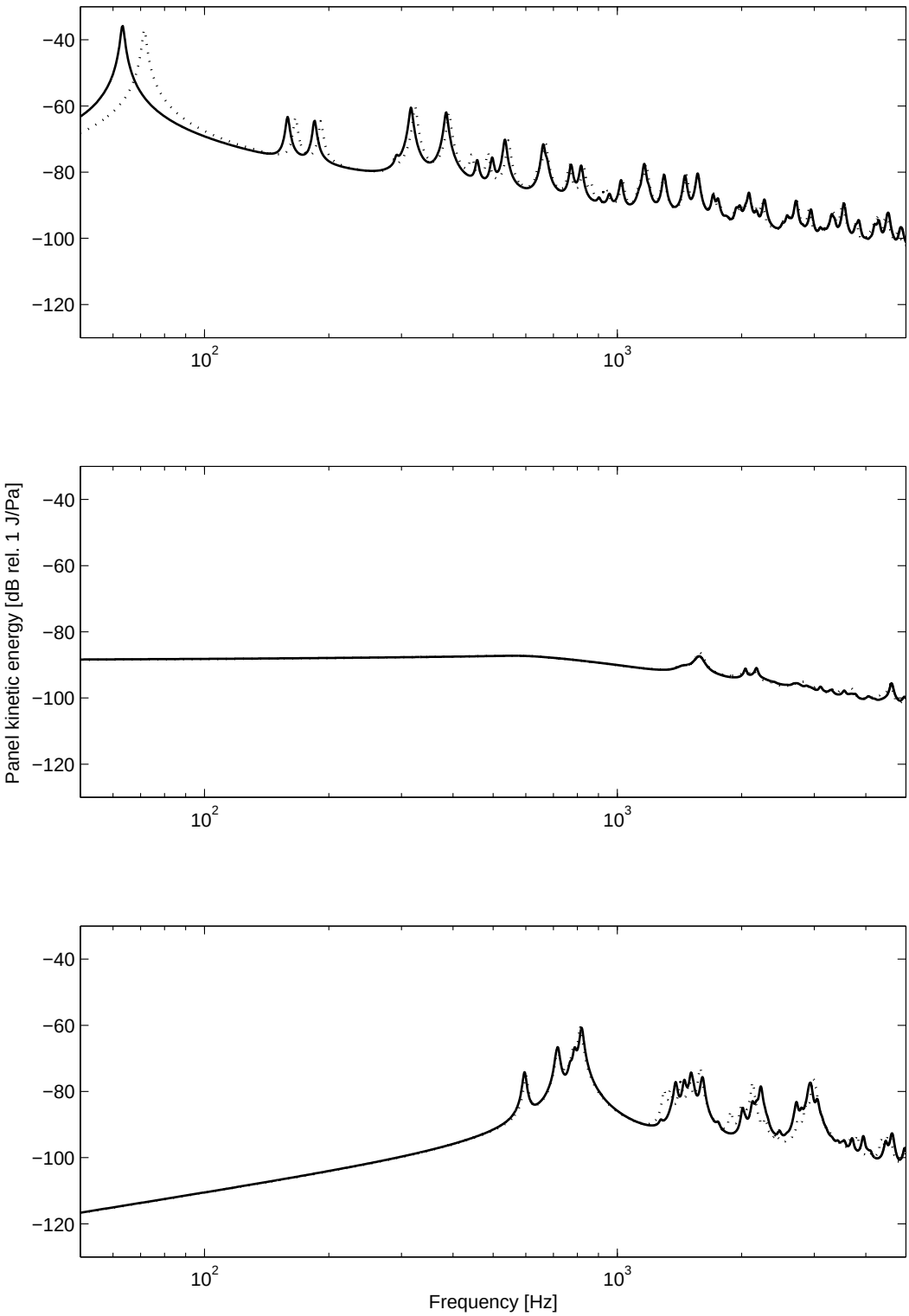

Figure 3.19: Panel Kinetic panel energy normalized to the pressure amplitude of an acoustic plane wave for an all side pinned panel ($dotted$) and an initially completely free panel with linear dampers ($\eta = 10^{12}$) along the boundaries ($solid$). Results without control (top graph), results for an 'optimal' control gain of 40 (mid graph) and a a 'maximum' control gain of 10^6 (bottom graph).

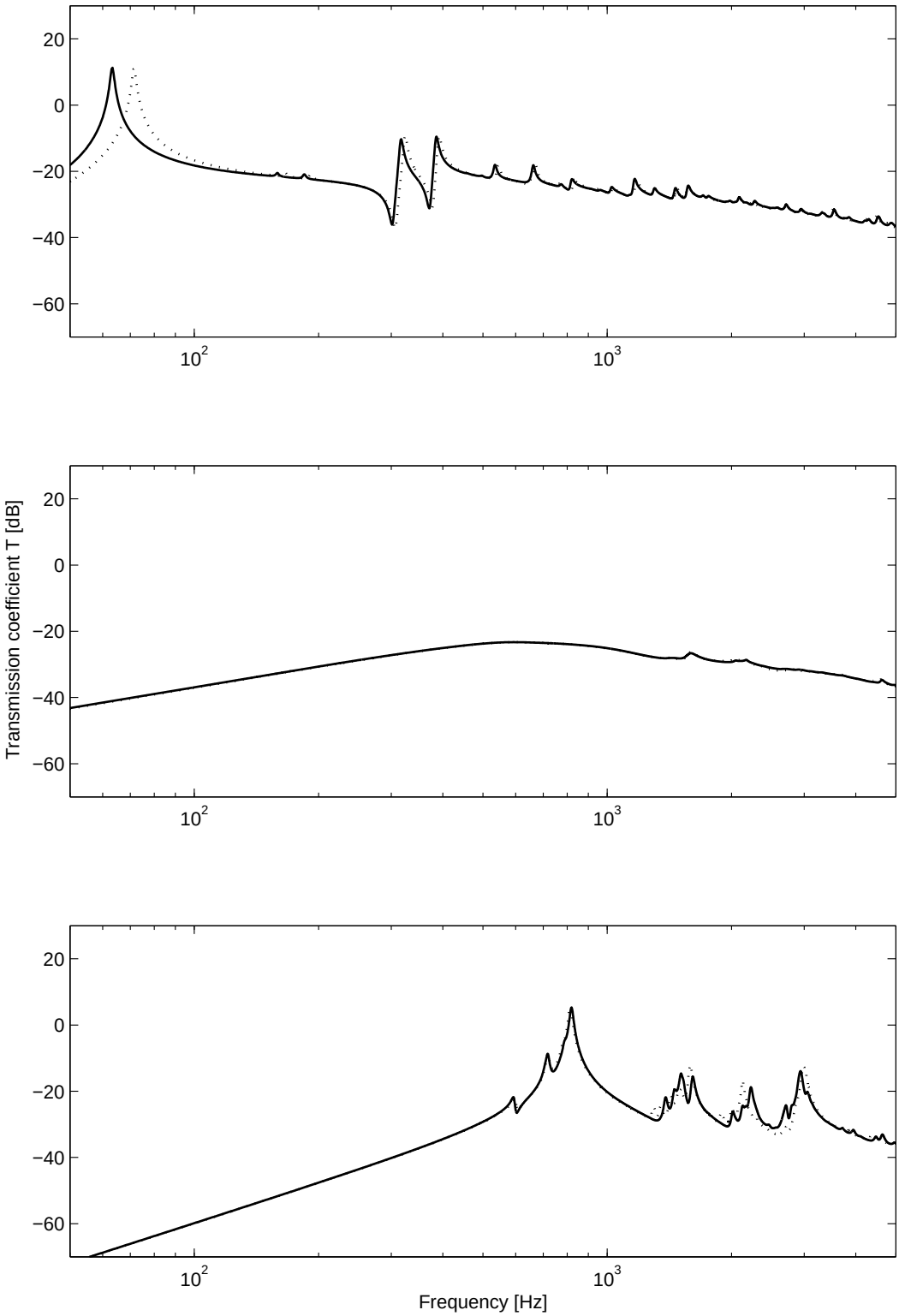

Figure 3.20: Transmission coefficient for a pinned panel model $(dotted)$ and free panel model with linear dampers ($\eta = 10^{12}$) along the boundaries $(solid)$. Results without control (top graph), results for an 'optimal' control gain of 40 (mid graph) and a a 'maximum' control gain of 10^6 (bottom graph).

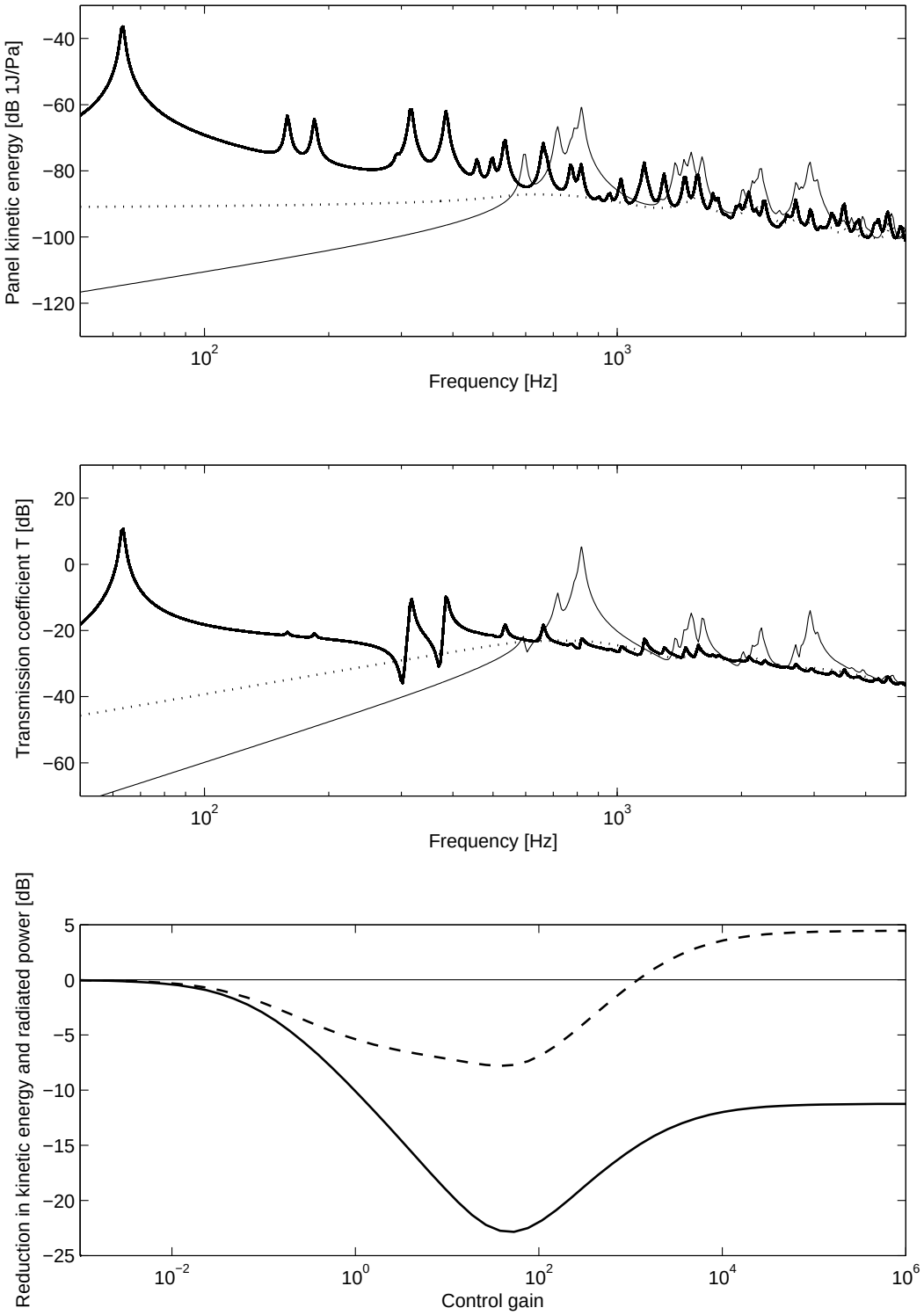

Figure 3.21: Panel kinetic energy, transmission coefficient and achieved reductions for an initially completely free panel with enforced pinned boundary conditions excited by an acoustic plane wave incident at an angle $\theta = 45^\circ$ and $\varphi = 45^\circ$. Panel kinetic energy (top graph), Transmission coefficient (mid graph), no control ($solid$) optimal control ($dotted$) 'maximum' control gain of (10^6) ($faint$) and achieved reduction (bottom graph) in total panel kinetic energy ($solid$) and total radiated sound power ($dashed$).

3.3.2 Clamped boundary conditions

Figures 3.22 and 3.23 show the simulated results for the panel kinetic energy and transmission coefficient for an acoustic plane wave excitation. The cases of a panel with all side clamped is compared to those of an initially all side pinned panel and a completely free panel with enforced clamped boundary conditions. In the case based on the all side pinned boundary conditions, clamped conditions where enforced by introducing rotational dampers at the boundary locations acting perpendicular to the panel edges. In the case based on the initially completely free panel, clamped conditions where enforced by modelling passive linear and rotational dampers at the boundary points along the edges. The damping coefficient for both linear and rotational dampers were set to $b = 10^{12}$ Nsm^{-1}.

The comparison between the kinetic energy and radiated sound power of the clamped panel after Warburton [11] and the pinned panel with enforced boundary moments shows an excellent agreement. For the case initially using formulations for a complectly free panel with enforced boundary forces and moments a reasonably good overall agreement is observed. The difference in the fundamental panel frequency for a clamped and initially free panel model is 131.2 Hz - 135.4 Hz = -4.2 Hz, which is a deviation by 3.2%. In difference to the pinned case the relative difference between the predicted natural frequencies does not decrease with increasing frequency. It is difficult to assess the accuracy of the results for the three models because the clamped and completely free panel models are based on simple approximations formulations for the panel natural frequencies and mode shapes given by Warburton [11]. Only the initially pinned panel model is based on analytically accurate solutions for natural frequencies and modeshapes. The good agreement between the results for the clamped and initially pinned model with boundary moments suggests that the main reason for the observed differences are due to the limited accuracy of the completely free panel formulations used in this study. It has however been shown that the approach of enforced linear and rotational boundaries on an initially completely free panel model can generally be used to estimate the sound transmission through a clamped panel. The yield accuracy is assumed to be acceptable for within the scope of this project.

The top two graphs in Figure 3.21 show the resulting panel kinetic energy and transmis-

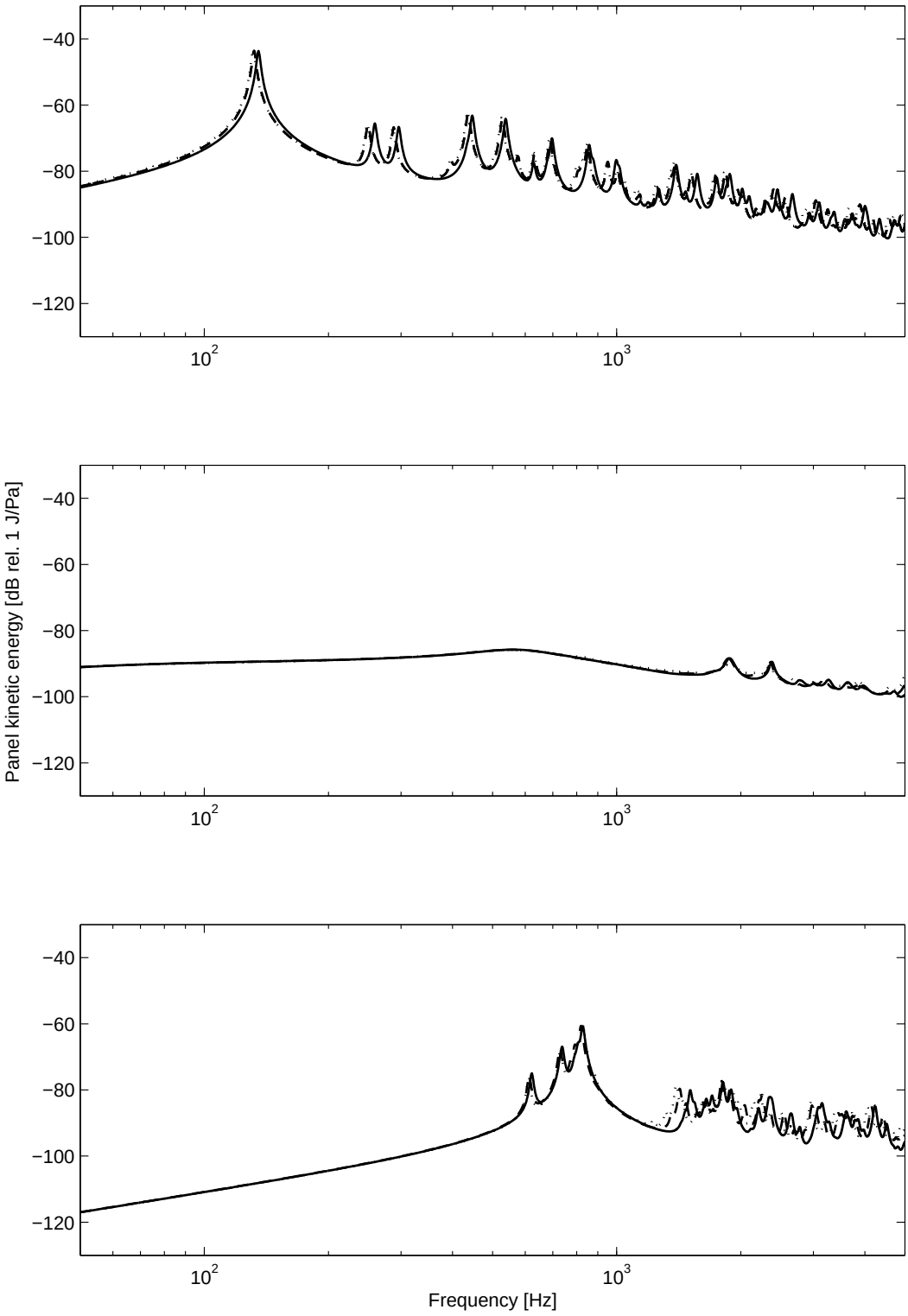

Figure 3.22: Panel Kinetic panel energy normalized to the pressure amplitude of an acoustic plane wave incident at incident at an angle $\theta = 45°$ and $\varphi = 45°$ for a clamped panel model $(dotted)$, an initially pinned panel with rotational dampers $=10^9$ $(dashed)$ and an initially completely free panel model with linear and rotational dampers $(=10^9)(solid)$. Results without control (top graph), results for an 'optimal' control gain of 40 (mid graph) and a a 'maximum' control gain of 10^6 (bottom graph).

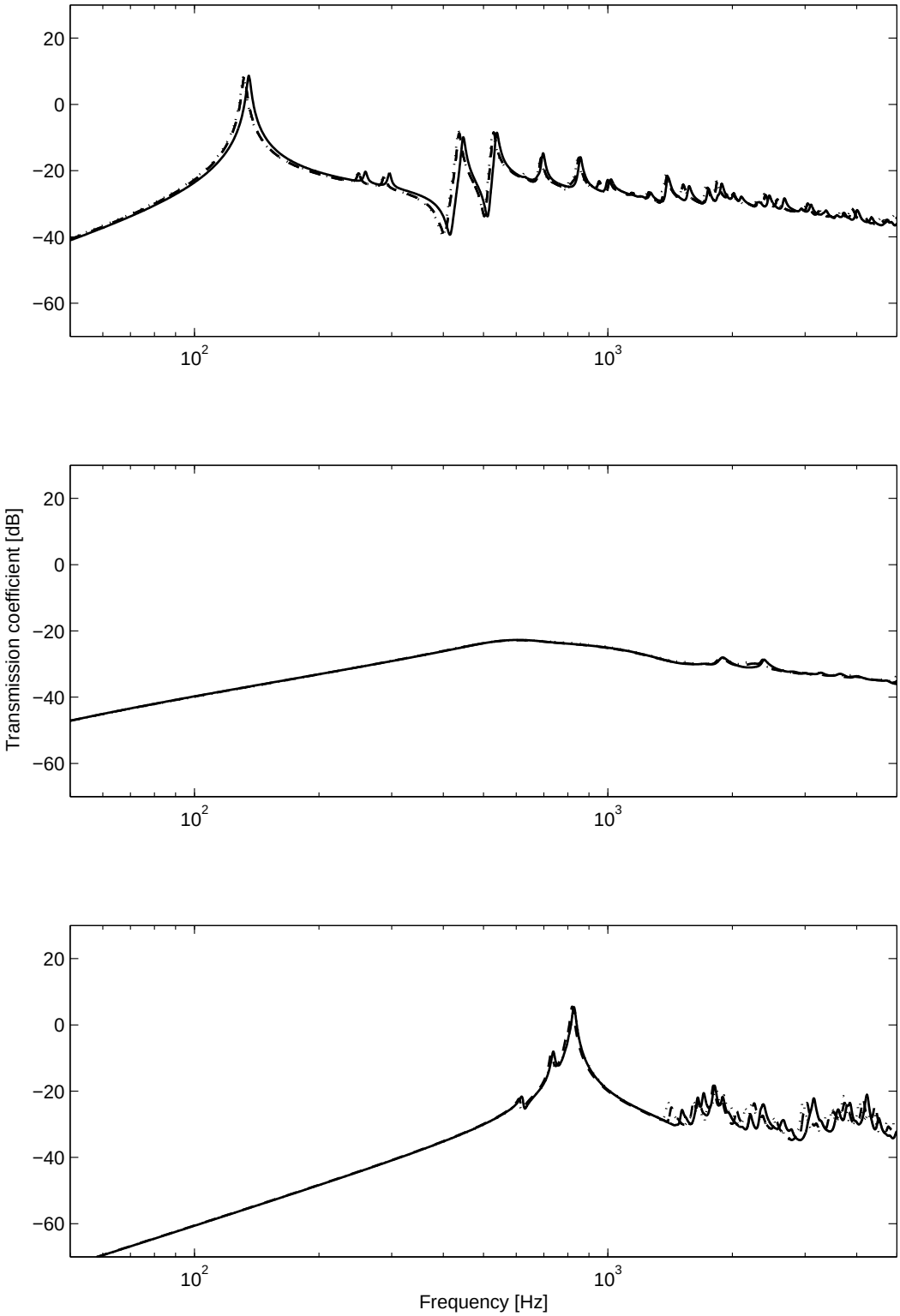

Figure 3.23: Transmission coefficient for a for a clamped panel model $(dotted)$, an initially pinned panel with rotational dampers $=10^9$ $(dashed)$ and an initially completely free panel model with linear and rotational dampers $(=10^9)(solid)$. Results without control (top graph), results for an 'optimal' control gain of 40 (mid graph) and a a 'maximum' control gain of 10^6 (bottom graph).

sion coefficient for the initially complectly free panel with enforced clamped boundary conditions without control, an 'optimal' velocity feedback gain and a 'maximum' velocity feedback gain of 10^6. The bottom graph shows the achieved reduction in panel kinetic energy and radiated sound power for a velocity feedback gain range form 10^{-3} to 10^6. It can be seen that the optimal control is achieved a for a velocity feedback gain of about 40 which is similar to the optimal feedback gain identified for a panel with all edges pinned. The achieved reduction in panel kinetic energy for the clamped boundary case is about 4 dB less than for a panel with all side pinned boundaries. The achieved reduction in radiated sound power for both boundary conditions are very similar.

3.3.3 Flexible boundary conditions

After verifying that the extreme boundary conditions can be modelled adequately accurately, the capability of modelling arbitrary visco-elastic boundaries will be illustrated. Figures 3.25 and 3.26 show the simulated results for the panel kinetic energy and radiated power normalized to the pressure amplitude of the incident acoustic plane wave, for a pinned, a clamped [11] and a completely free rectangular panel [11] with enforced flexible boundaries. For this example each boundary location is modelled as a linear and rotational (in x and y direction) spring with a stiffness $s = 10^3$ Nm^{-1}. The results show that it is possible to simulate a panel with arbitrary flexible, possibly fuzzy boundaries. A systematic study on the effect of variable, uncertain boundaries on the control performance has yet to be conducted and is suggested as future work within this project.

Summary

Within this section the panel model with enforced linear and rotational boundaries has been compared against the two extreme cases of a panel with all sides pinned and with all sides clamped. The results showed a good overall agreement. Relative differences in the predicted natural frequencies of the panel are shown to be fairly small and are thought to be acceptable for most engineering applications. For cases where the accuracy is not sufficient it might be possible to implement more accurate panel formulations such as those developed by Gorman [21, 22, 23].

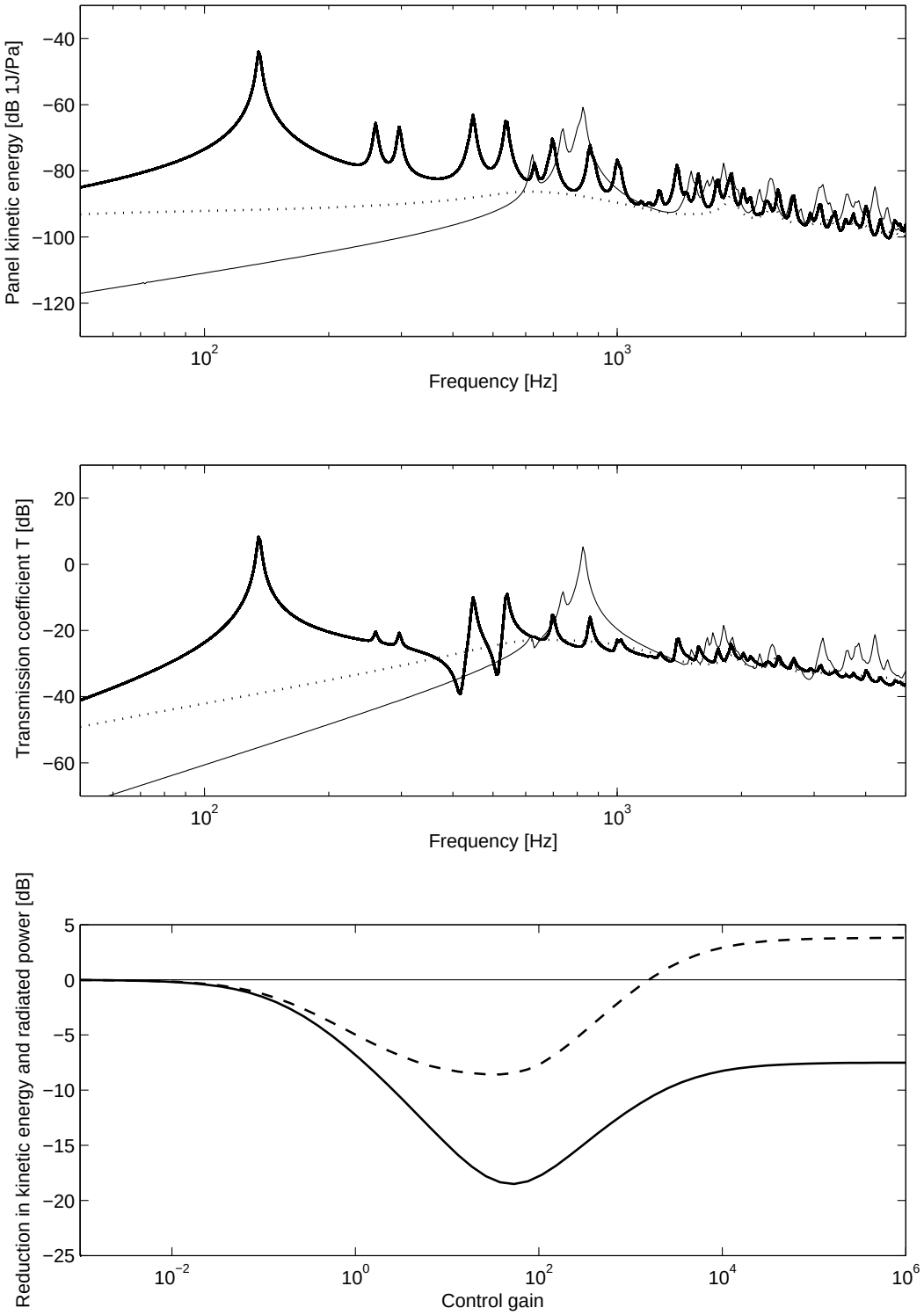

Figure 3.24: Panel kinetic energy, transmission coefficient and achieved reductions for an initially completely free panel with enforced pinned boundary conditions excited by an acoustic plane wave incident at an angle $\theta = 45^\circ$ and $\varphi = 45^\circ$. Panel kinetic energy (top graph), Transmission coefficient (mid graph), no control ($solid$) optimal control ($dotted$) 'maximum' control gain of (10^6) ($faint$) and achieved reduction (bottom graph) in total panel kinetic energy ($solid$) and total radiated sound power ($dashed$).

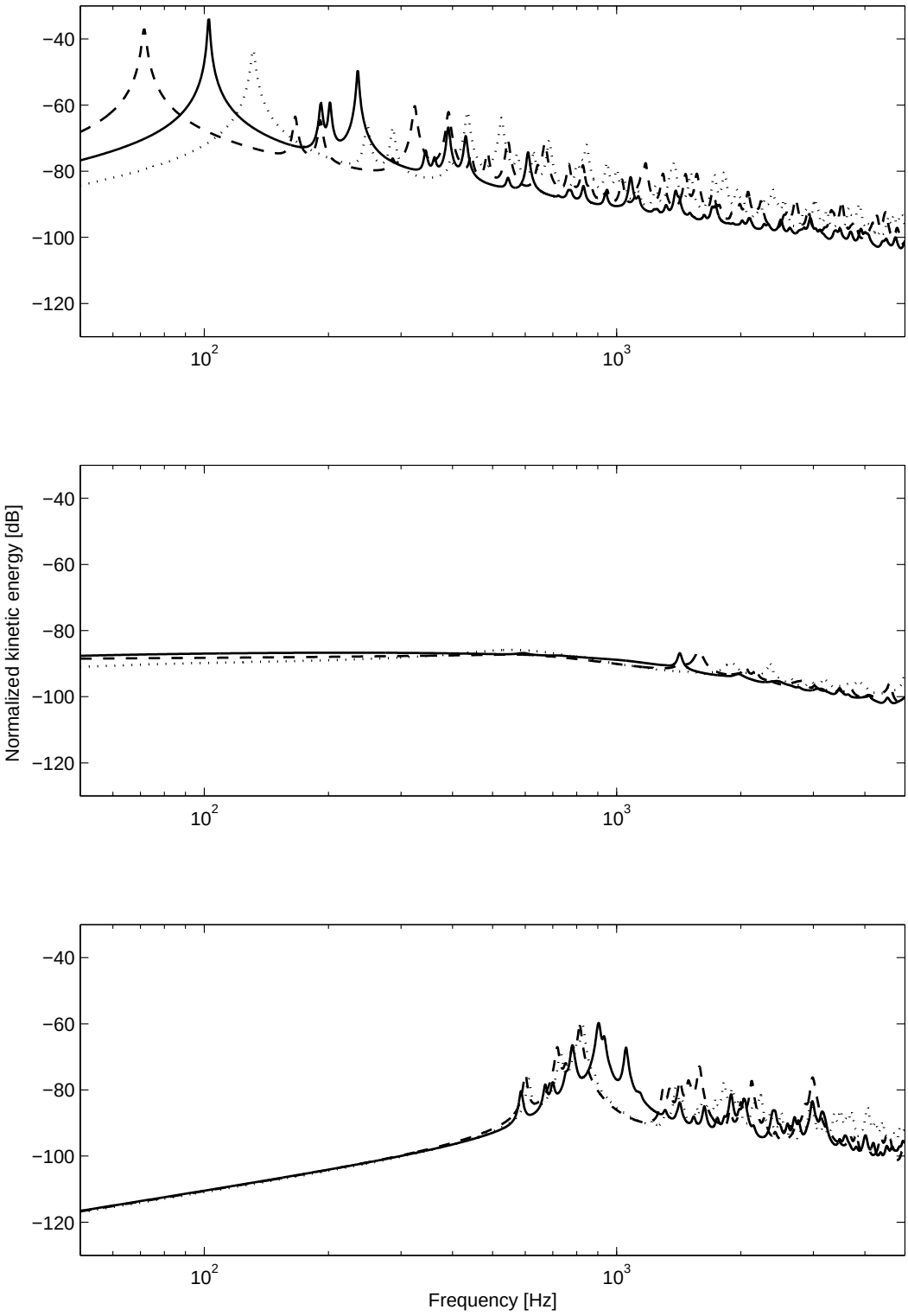

Figure 3.25: Panel Kinetic panel energy normalized to the pressure amplitude of an acoustic plane wave incident at incident at an angle $\theta = 45°$ and $\varphi = 45°$ for an all side pinned panel $(dashed)$, an all side clamped panel $(dotted)$ and an initially completely free panel model with linear and rotational springs $(s = 10^3\ Nm^{-1})(solid)$. Results without control (top graph), results for an 'optimal' control gain of 40 (mid graph) and a a 'maximum' control gain of 10^6 (bottom graph).

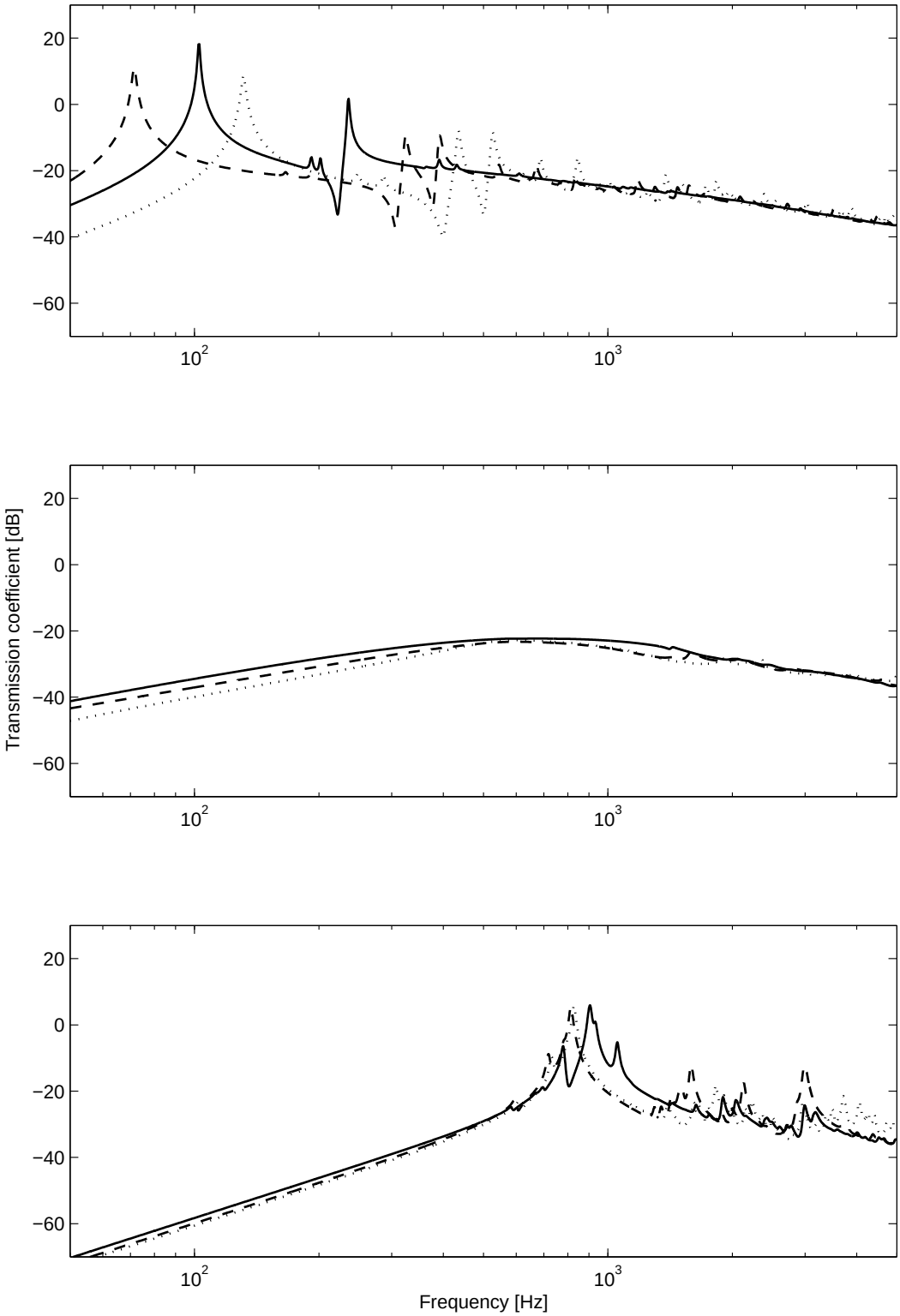

Figure 3.26: Transmission coefficient for an all side pinned panel ($dashed$), an all side clamped panel ($dotted$) and an initially completely free panel model with linear and rotational springs ($s = 10^3\ Nm^{-1}$) ($solid$). Results without control (top graph), results for an 'optimal' control gain of 40 (mid graph) and a a 'maximum' control gain of 10^6 (bottom graph).

A case of boundary conditions with flexible linear and rotational springs is presented to illustrate that the developed model can be used to predict the panel response for intermediate arbitrary visco-elastic boundaries. The formulations developed in Section 2.7 and 2.8 can therefore be used as the basis for systematic studies on the effect of variable boundaries on the control performance of decentralized velocity feedback control. The results for the extreme cases suggest that the achieved overall reduction is dominated by the reduction achieved for the fundamental panel mode. Depending on the control target the overall reduction in the linear spectrum might not always be a good indication of the control performance for a particular application.

3.4 Stochastic excitation

In this section the results for three Stochastic excitation models i.e. acoustic diffuse field, turbulent boundary layer (TBL) and rain on the roof, as introduced in Section 2.10 are presented. The spectra of the panel kinetic energy and the radiated sound power are compared to the case of a deterministic acoustic plane wave excitation. For the acoustic diffuse field the results are fairly similar to the result obtained for a plane wave excitation. For the rain on the roof and the TBL disturbance significant differences in the predicted spectra are observed.

Throughout this section the panel kinetic energy and radiated sound power for a plane acoustic wave with a 1 Pa pressure amplitude, incident at an angle $\theta = 45^\circ$ and $\varphi = 45^\circ$ are used as reference spectra. For each type of disturbance the results for the passive all side pinned panel, and a pinned panel with 16 discrete $(\Delta/2, \Delta, \Delta/2)$ distributed idealized velocity feedback control loops, with a feedback gain of 40 (optimal) and 10^6 (maximum gain, pinned condition) are presented. The formulations for the three types of considered stochastic excitation and required excitation parameter are given in Section 2.10. In addition the achieved control performance for each disturbance type for a range of control gains from 10^{-3} to 10^6 are studied.

3.4.1 Acoustic diffuse field excitation

The acoustic diffuse field model is commonly used to describe the sound field in rigid walled reverberant enclosures and forms the basis for the prediction and experimental estimation of sound transmission through partitions. Figures 3.27 and 3.28 show the simulated results for the panel kinetic energy and radiated sound power due to an acoustic plane wave and an acoustic diffuse field disturbance where the spectra for the acoustic diffuse field is normalized to the pressure amplitude of an equivalent acoustic plane wave. The results for both disturbances are almost identical, no significant difference has been identified. Some minor variations in the spectra can be observed for frequencies above 1 kHz. Therefore the plane wave excitation incident with an angle $\theta = 45°$ and $\varphi = 45°$ seems to be a good approximation for diffuse field conditions in the observed frequency range. For completeness the graphs for the spectrum of the kinetic energy and radiated sound power are presented in Figures 3.27 to 3.29. For later comparison with the TBL and ROR disturbances it is interesting to note that the resonant peaks of the altered panel modes for high velocity feedback gains clearly exceed the levels in the spectrum of the passive panel for both the spectra of the panel kinetic energy and the radiated sound power.

Figure 3.29 shows the predicted panel kinetic energy for a passive panel without control, the 'optimal' control gain and a 'maximum' control velocity feedback gain of 10^6. The results are very similar to those for a acoustic plane wave presented in Section 3.1 Figure 3.2. The bottom graph in Figure 3.29 shows the predicted reduction in panel kinetic energy in the frequency range between 5 Hz and 5 kHz. The control optimum in respect to reduction in panel kinetic energy and reduction in radiated sound power are achieved for the same velocity feedback gain. The maximum achieved reduction in radiated sound power is about -8 dB The maximum reduction in panel kinetic energy is about -22 dB.

3.4.2 Turbulent boundary layer excitation

Turbulent boundary layer excitation is primarily of interest for applications which involve high speed air flow such as aircraft fuselage, body works of high speed trains and cars. Figure 3.30 and 3.31 show the predicted panel kinetic energy and radiated sound power for a acoustic plane wave and TBL disturbance as defined in Table 2.4. The results for

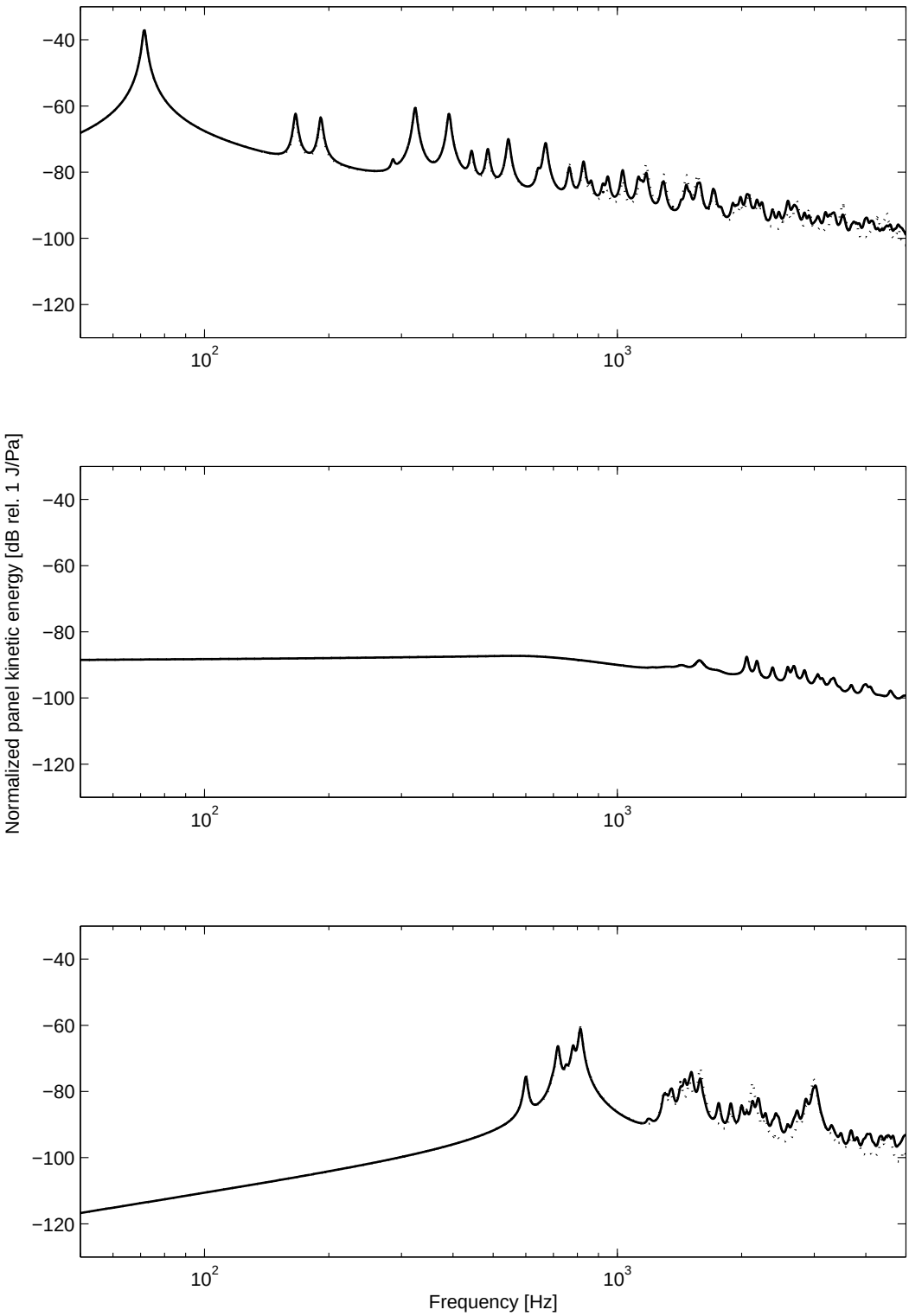

Figure 3.27: Panel kinetic energy for a plane wave incident with an angle θ=45° and φ=45° $(dotted)$ and acoustic diffuse field disturbance $(solid)$ for a passive panel without control (top graph), for an 'optimal' velocity feedback gain of 40 (mid graph) and for a 'maximum' control gain of (10^6) (bottom graph) and achieved reduction (bottom graph).

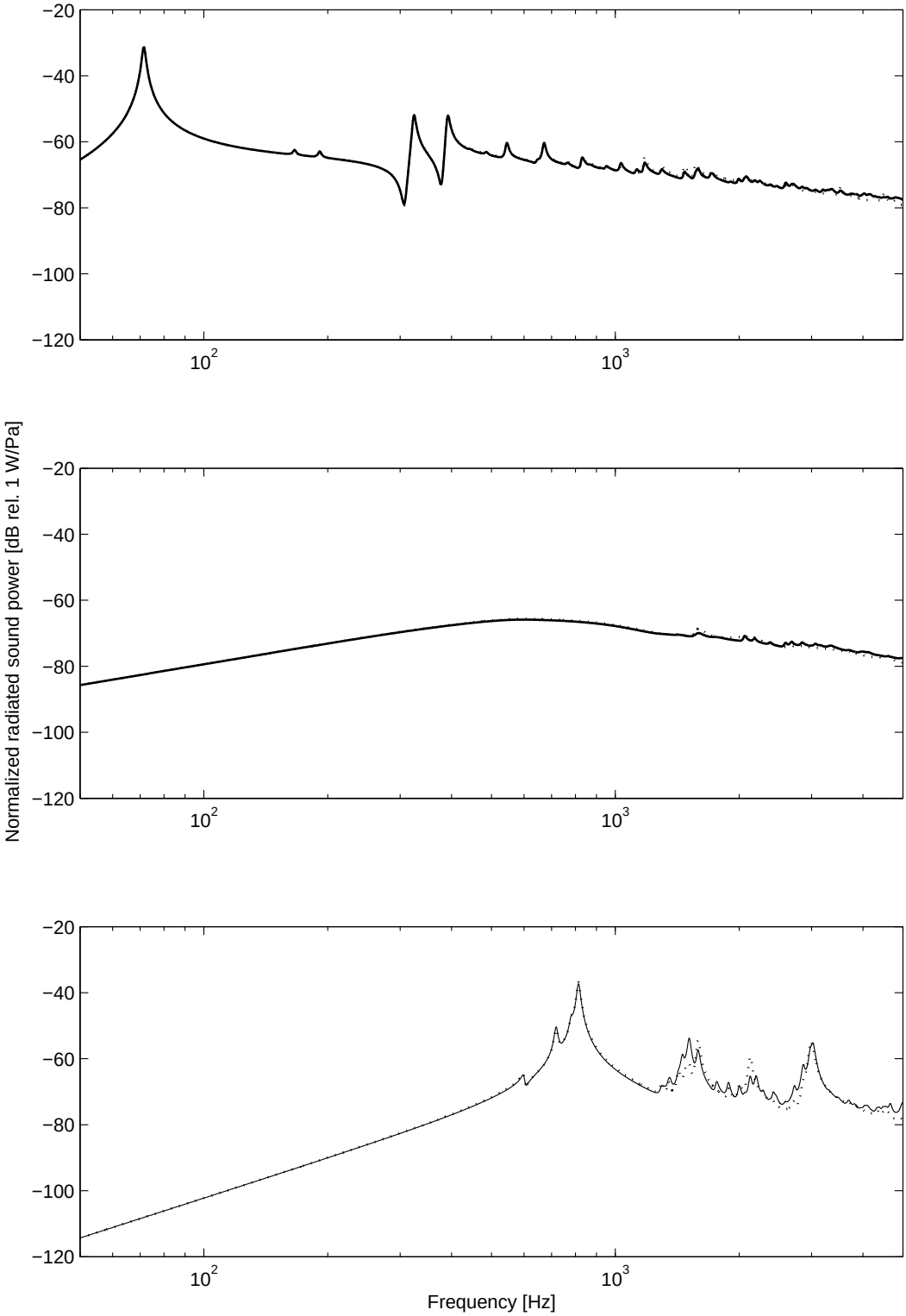

Figure 3.28: Radiated sound power for a plane wave incident with an angle θ=45° and φ=45° $(dotted)$ and acoustic diffuse field disturbance $(solid)$ for a passive panel without control (top graph), for an 'optimal' velocity feedback gain of 40 (mid graph) and for a 'maximum' control gain of (10^6) (bottom graph) and achieved reduction (bottom graph).

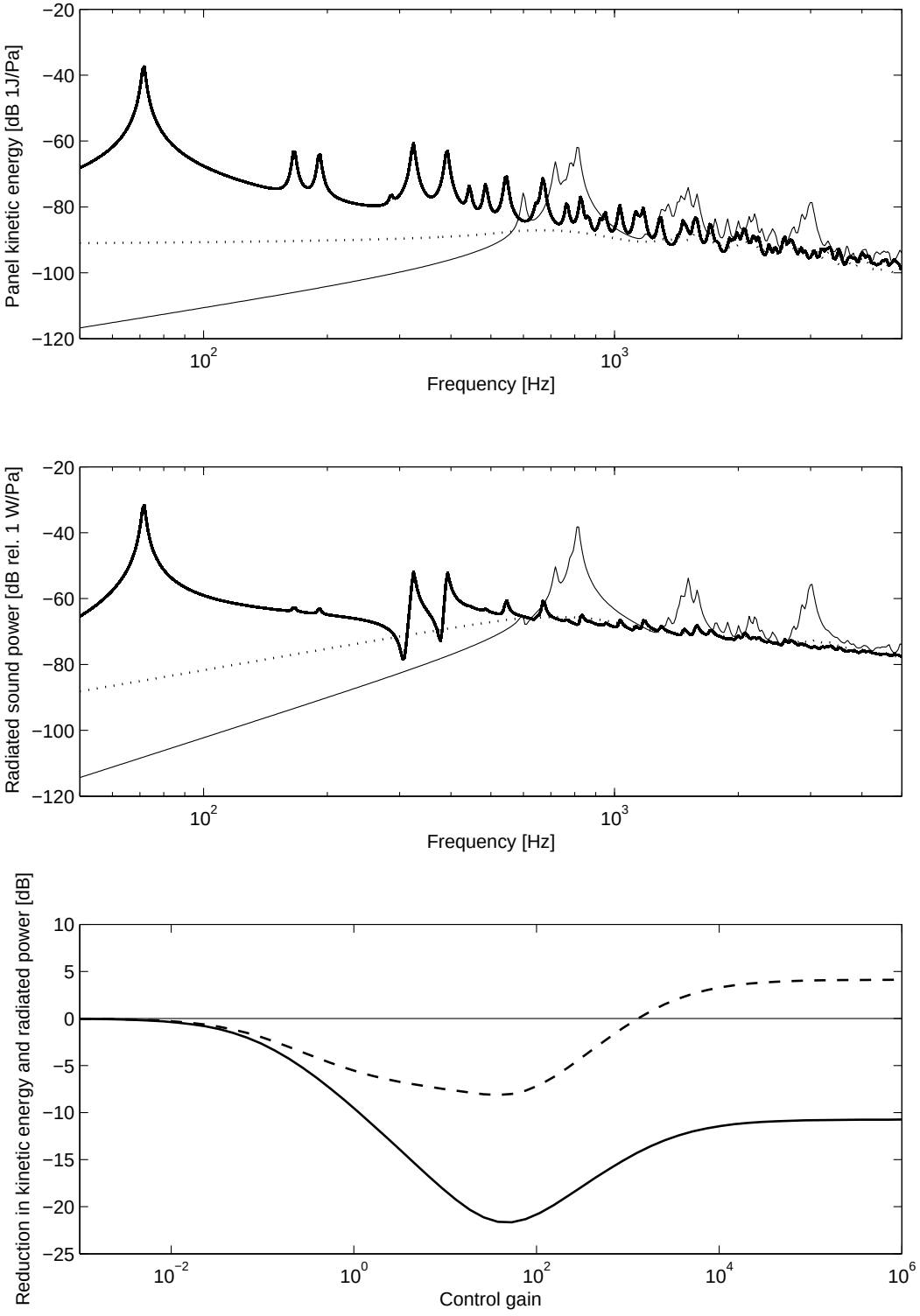

Figure 3.29: Panel kinetic energy, transmission coefficient and achieved reductions for a panel considering acoustic diffuse field disturbance for a range of velocity feedback gains. between 10^-3 and 10^6. Panel kinetic energy (top graph) Transmission coefficient (mid graph), no control ($solid$) optimal control ($dotted$) max control (10^6) ($faint$) and achieved reduction (bottom graph) in total panel kinetic energy ($solid$) and total radiated sound power ($dashed$).

the acoustic plane wave disturbance are normalized to it's pressure amplitude, the results for the TBL are normalized to the pressure amplitude of the equivalent pressure field in the boundary layer acting on the panel. For very low frequencies the element excitation forces for both disturbances are highly spatially correlated. Hence the comparison of the panel kinetic energy spectra of the passive panel for both acoustic plane wave and TBL disturbance in Figure 3.30 show similar results in the frequency range below and around the fundamental panel resonance up to about 100 Hz. For higher frequencies the spectrum for the plane wave excitation follows the 'mass law' and is dropping by 6 dB per octave i.e. 20 dB per decade. The spectrum for TBL disturbance does drop at a comparable rate, but the panel modes seem more evenly excited. Both investigated active control cases, 'optimal' gain of 40 and a maximum gain of 10^6 show almost no differences in the frequency range below 500 Hz where the panel modes are either highly damped or completely cancelled. For frequencies above 500 Hz the spectra are relatively similar.

Figure 3.31 shows the predicted radiated sound power normalized to the pressure amplitude of the incident pressure field, for a plane wave and a TBL disturbance. Although the spectra of the kinetic energy in Figure 3.30 tended to be higher for the TBL than for the acoustic plane wave disturbance, the spectra of the radiated sound power indicate an opposite trend. Results for both, the passive panel and the panel with active velocity feedback control, show a higher radiated power for the acoustic plane wave excitation.

This indicates that the radiation efficiency for both types of disturbances is different. A study on the radiation efficiency of a thin panel under different types of disturbances could yield further insight in the panels radiation characteristics. This however is beyond the scope of this memorandum and is left as a suggestion for future work.

In contrast to the radiated sound power spectra for the plane wave and acoustic diffuse field disturbance, there are no anti resonance in the spectrum of the radiated sound power for the TBL disturbance. It is assumed that this is due to the properties of the spatial correlation function. Different to the two acoustic disturbances the spatial correlation function for the TBL does not have roots, the spatial correlation is positive through out and exponentially decays with increasing distance [5].

The upper two graphs in Figure 3.32 show the normalized panel kinetic energy and radiated sound power for the panel without control, an 'optimal' feedback gain and a 'max-

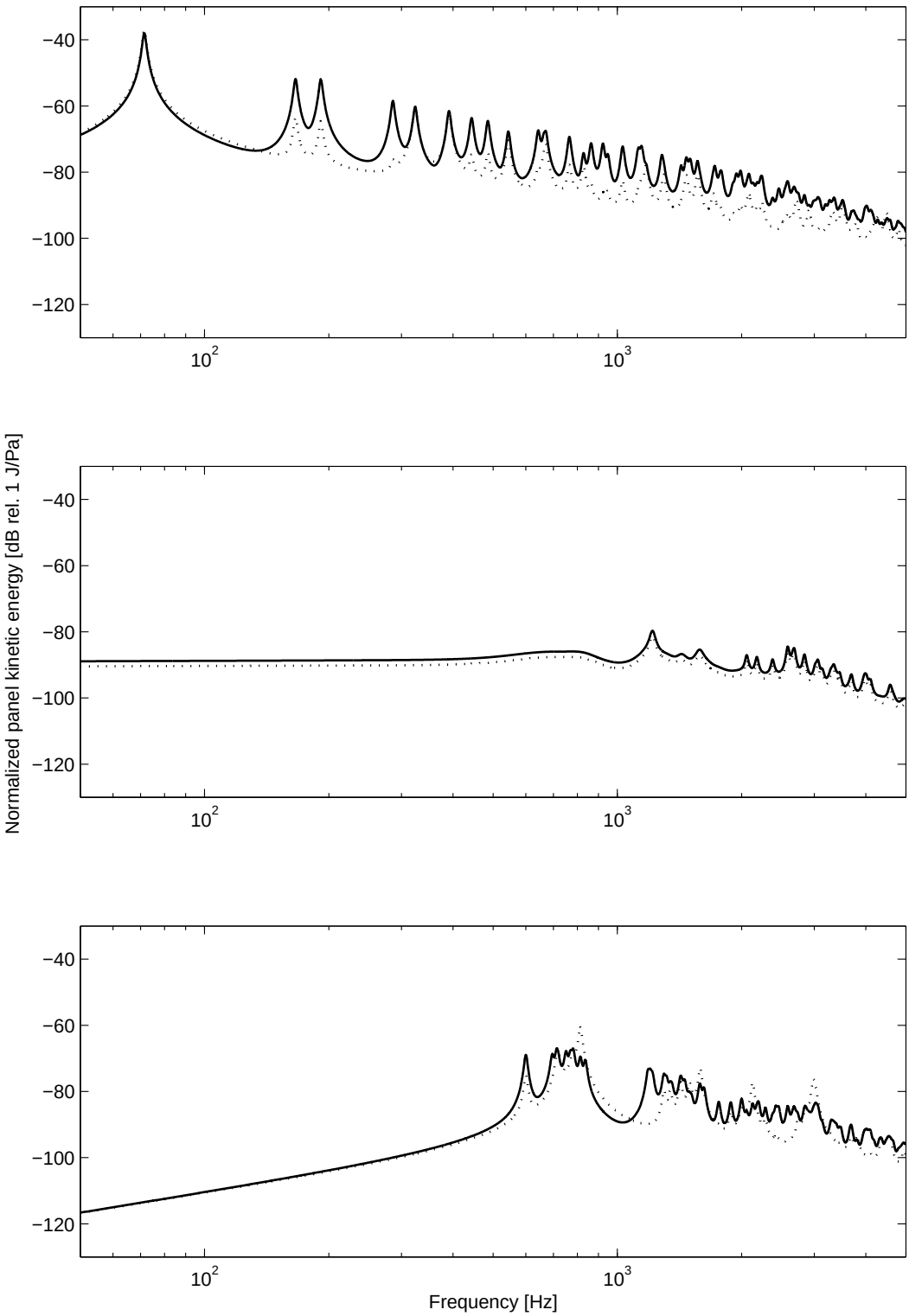

Figure 3.30: Panel kinetic energy for a plane wave incident with an angle θ=45° and φ=45° $(dotted)$ and TBL disturbance $(solid)$ for a passive panel without control (top graph), for an 'optimal' velocity feedback gain of 40 (mid graph) and for a 'maximum' control gain of (10^6) (bottom graph) and achieved reduction (bottom graph).

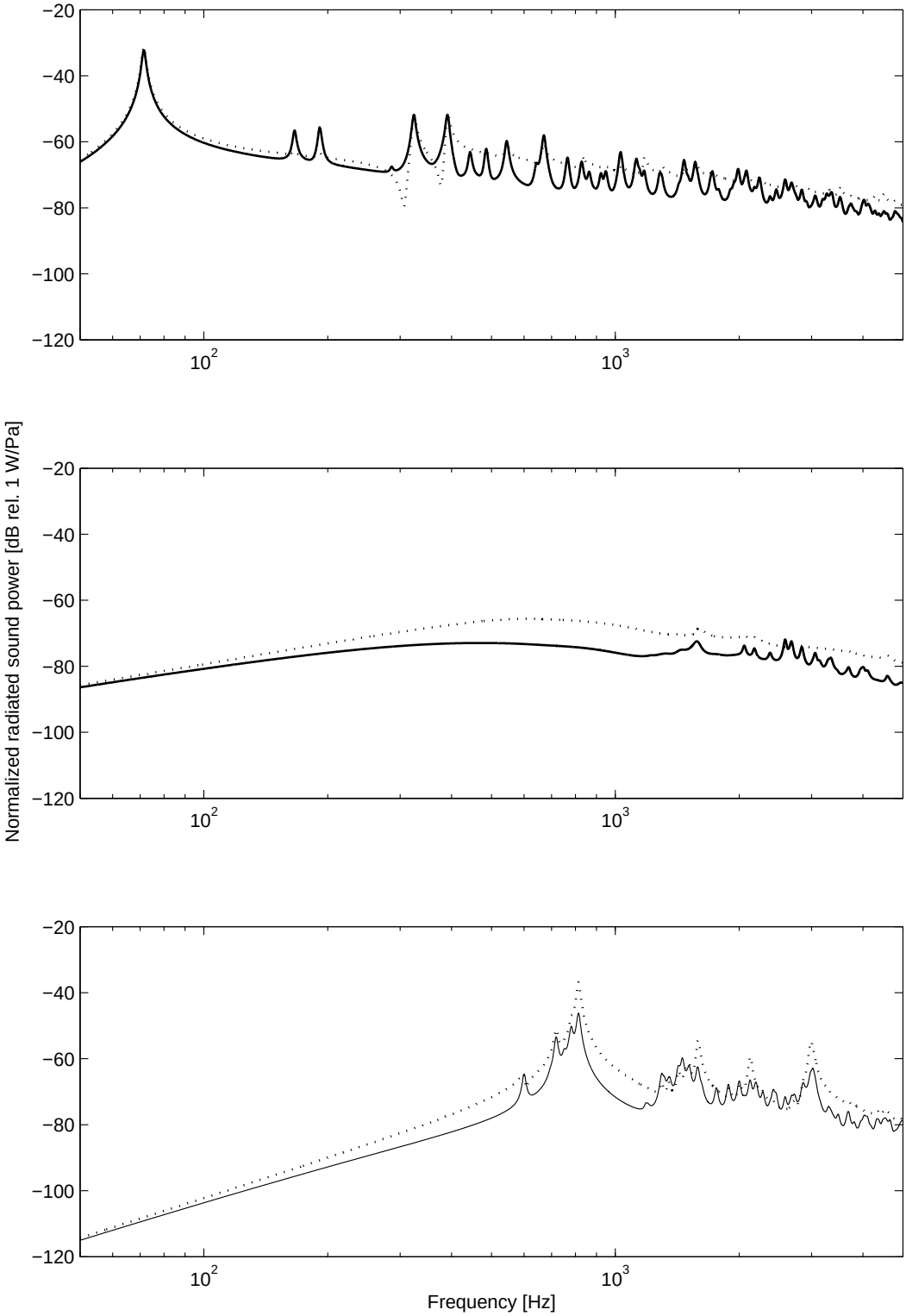

Figure 3.31: Radiated sound power for a plane wave incident with an angle θ=45° and φ=45° $(dotted)$ and TBL disturbance $(solid)$ for a passive panel without control (top graph), for an 'optimal' velocity feedback gain of 40 (mid graph) and for a 'maximum' control gain of (10^6) (bottom graph) and achieved reduction (bottom graph).

imum' control gain of 10^6. It is interesting to note that in contrast to the kinetic energy spectra of the plane wave and acoustic diffuse field excitation the resonant peaks of the altered panel modes do not exceed the peak levels of the passive panel modes at those frequencies. For the spectrum of the radiated sound power in the middle graph of Figure 3.32 this peaks exceed the levels of the passive panel which is similar to the observations made for the radiated sound power spectra for acoustic disturbances. These characteristics might again be explained by considering the properties of the spatial correlation function and the radiation efficiency of the panel for a TBL disturbance.

The bottom graph in Figure 3.32 shows the predicted reduction in panel kinetic energy and radiated sound power in the frequency range between 5 Hz and 5 kHz. The control optimum in respect to reduction in panel kinetic energy and reduction in radiated sound power occur for the same velocity feedback gain. The optimum gain is slightly lower than for the acoustic disturbances. The maximum achieved reduction in radiated sound power is about -15 dB and hence 7 dB higher than for the acoustic disturbances. The maximum reduction in panel kinetic energy is about -21 dB, this is similar to the reduction achieved for the two acoustic disturbance cases. It is interesting to note that for the TBL disturbance the radiated sound power at high control gains is actually not exceeding the levels predicted for a passive panel.

Within this study only one typical model of boundary layer excitation as defined in Table 2.4 has been considered. During a normal flight cycle of an aircraft the specifications of the boundary layer will change with speed, altitude and ambient temperature. Further studies on the variability of the boundary layer and it's effect on the sound transmission and the control performance are suggested as future work within this project.

3.4.3 Rain on the roof excitation

A rain on the roof disturbance is characterized by temporal and spatial uncorrected random point forces across the panel surface. Figure 3.33 and 3.34 show the predicted results for the panel kinetic energy and radiated sound power normalized to the pressure amplitude of the incident acoustic plane wave. The results for the rain on the roof disturbance have been normalized to yield identical energy and radiated sound power levels for the passive panel below the first panel resonance at a reference frequency of 5 Hz. This nor-

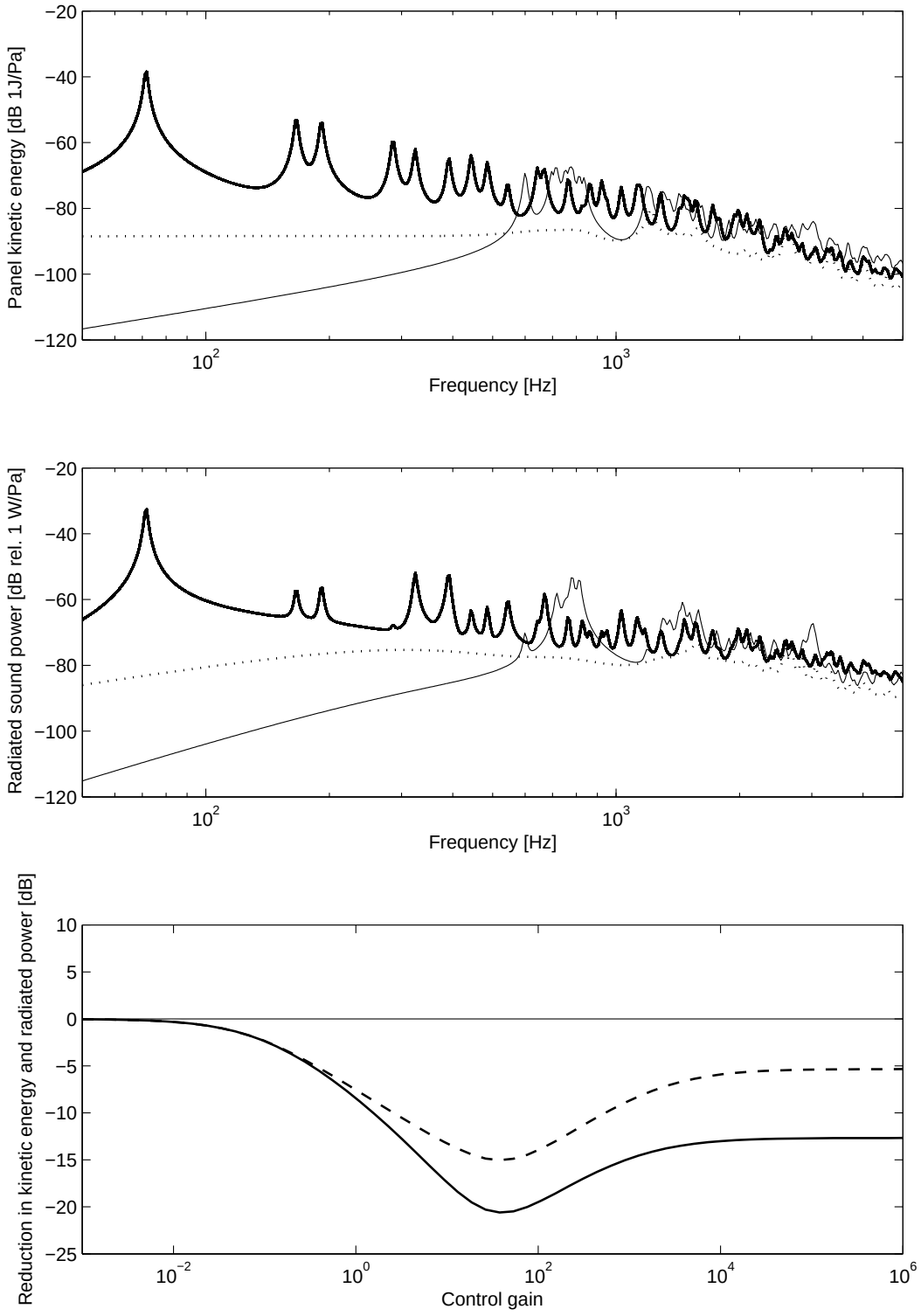

Figure 3.32: Panel kinetic energy, transmission coefficient and achieved reductions for a panel considering TBL disturbance for a range of velocity feedback gains. between 10^-3 and 10^6. Panel kinetic energy (top graph) Transmission coefficient (mid graph), no control ($solid$) optimal control ($dotted$) max control (10^6) ($faint$) and achieved reduction (bottom graph) in total panel kinetic energy ($solid$) and total radiated sound power ($dashed$).

malisation was chosen to allow a direct comparison between the predictions for both types of excitations. A more formal comparison is difficult since the element excitation forces for the plane wave excitation become increasingly spatial correlated with decreasing frequency while the excitation forces for the rain on the roof excitation remain uncorrected throughout.

The comparison of the panel kinetic energy spectra of the passive panel of both, plane acoustic wave and rain on the roof excitation in the top graph of Figure 3.33 shows very similar characteristic for the spectrum below and around the first panel resonance up to 100 Hz. For increasing frequency the spectrum for the plane wave excitation follows the 'mass law' and tends to drop by 6 dB per octave i.e. 20 dB per decade. The spectrum for the rain on the roof disturbance however does not drop but remains constant with frequency. All modes seem equally heavily excited where the magnitude of the resonance peaks is dropping with increasing frequency. For the optimal control case in the middle graph of Figure 3.33 low resonant modes are highly damped but the same general trends as for the passive panel spectrum can be identified. For the maximum velocity feedback gain case in the bottom graph of Figure 3.33 where the panel is pinned at the control points, the spectrum of the kinetic energy is generally higher for the rain on the roof disturbance, even for the low frequency range below the first altered structural mode. It is thought that this is due to the fact that the first altered mode is less heavily excited by the harmonic plane wave excitation than by the spatially uncorrelated rain on the roof excitation. Since the spectrum at low frequencies is dominated by the stiffness region of the first altered mode, the overall spectrum is increased.

Figure 3.34 shows the predicted results for the radiated sound power normalized to the pressure amplitude of the incident acoustic plane wave. The comparison of the radiated sound power of the passive panel of both, plane acoustic wave and rain on the roof excitation in the top graph of Figure 3.34 shows a very similar results for the spectrum below and around the first panel resonance up to the (1,2) mode. As for the panel kinetic energy the sound power spectrum for the plane wave excitation follows the 'mass law' and drops by 6 dB per octave i.e. 20 dB per decade. The spectrum for the rain on the roof disturbance however does not drop with increasing frequency but remains generally constant, it even tends to increase slightly above 3000 Hz. As for the TBL disturbance the radiated power spectrum for the rain on the roof disturbance does not feature anti resonances behaviour.

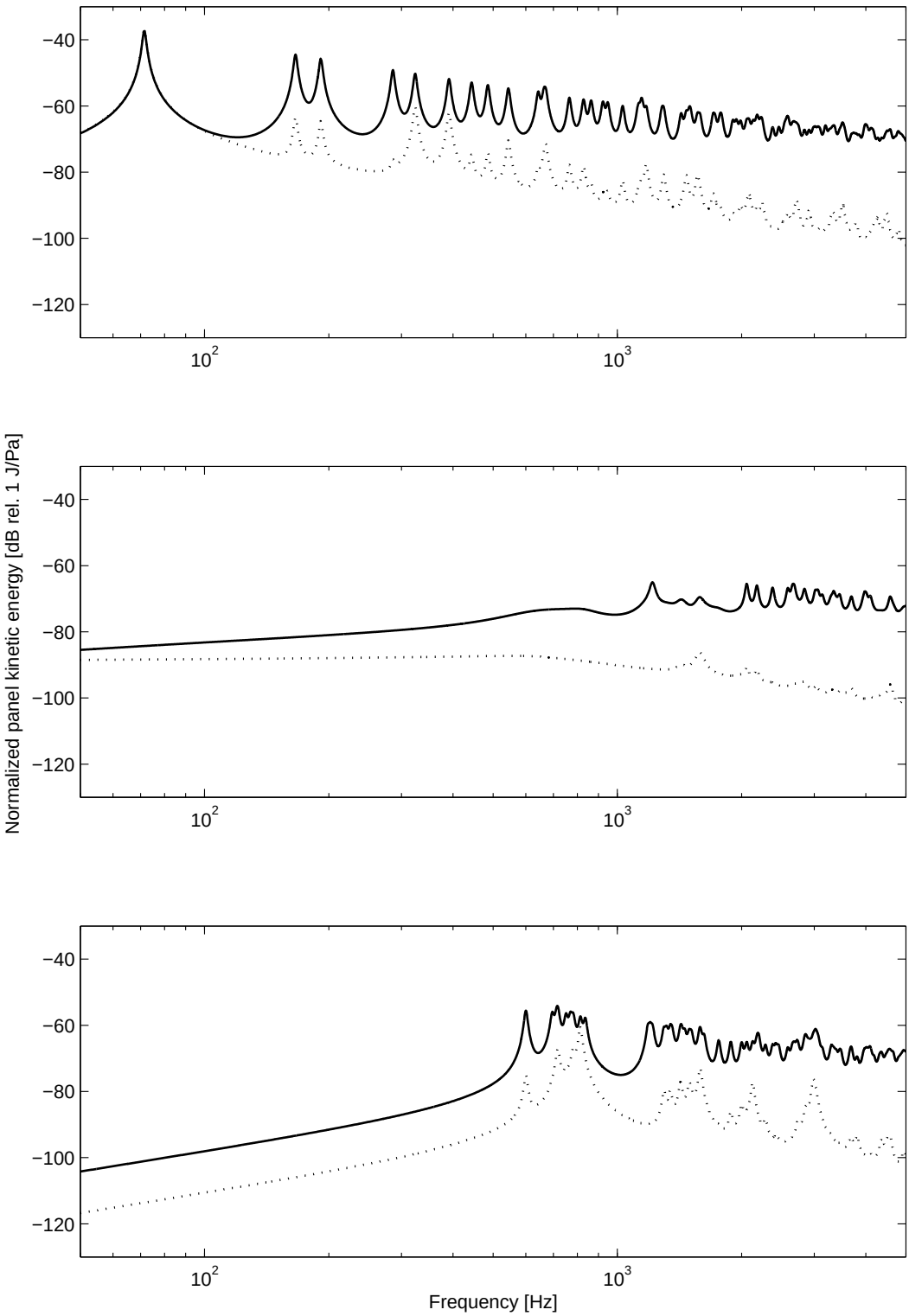

Figure 3.33: Panel kinetic energy for a plane wave incident with an angle θ=45° and φ=45° $(dotted)$ and random rain on the roof disturbance $(solid)$ for a passive panel without control (top graph), for an 'optimal' velocity feedback gain of 40 (mid graph) and for a 'maximum' control gain of (10^6) (bottom graph) and achieved reduction (bottom graph).

The spatial correlation function for a rain on the roof disturbance is a delta function at the orgin, the panel response can therefore be interpreted as an average over a discrete set of point responses across the panel. The result for a panel with velocity feedback control in the two bottom graphs of Figure 3.34 show that the spectrum of the radiated power for both disturbances are similar up to about 500 Hz. Above 500 Hz the predicted radiated sound power spectrum for the rain on the roof disturbance remains 'constant' while the spectrum for the plane wave disturbance rolls off according to the mass law.

The top two graphs in Figure 3.35 show the predicted panel kinetic energy for a passive panel without control, the 'optimal' control gain and a 'maximum' control velocity feedback gain of 10^6. As for the TBL disturbance the resonant peaks of the altered panel modes for high feedback gain do match the height of the peaks in the spectrum of the passive panel but do not exceed them as observed for the acoustic disturbances in the beginning of this section. The middle graph in Figure 3.35 shows the corresponding radiated sound power spectra for the three feedback gain cases. As seen for the other disturbances the resonant peaks of the altered panel modes for 'maximum' velocity feedback exceed the levels of the spectra predicted for the passive panel.

The bottom graph in Figure 3.35 shows the predicted reduction in panel kinetic energy in the frequency range between 5 Hz and 5 kHz. The control optimum in respect to reduction in panel kinetic energy and reduction in radiated sound power is achieved for the same velocity feedback gain. The optimum gain is lower than for the the TBL and acoustic disturbances. The maximum achieved reduction in radiated sound power is about -4 dB and hence significantly lower than for the other disturbances. The maximum reduction of in panel kinetic energy is about -8 dB, this is again significantly lower than the reduction achieved for the TBL and the two acoustic disturbance cases. Since the spectra are not rolling off with frequency uncontrolled higher order modes contribute more significantly to the linear overall panel energy and sound power level. For velocity feedback gains above 10^3 the predicted levels for the radiated sound power exceed the predicted levels for a passive panel by more than 4 dB.

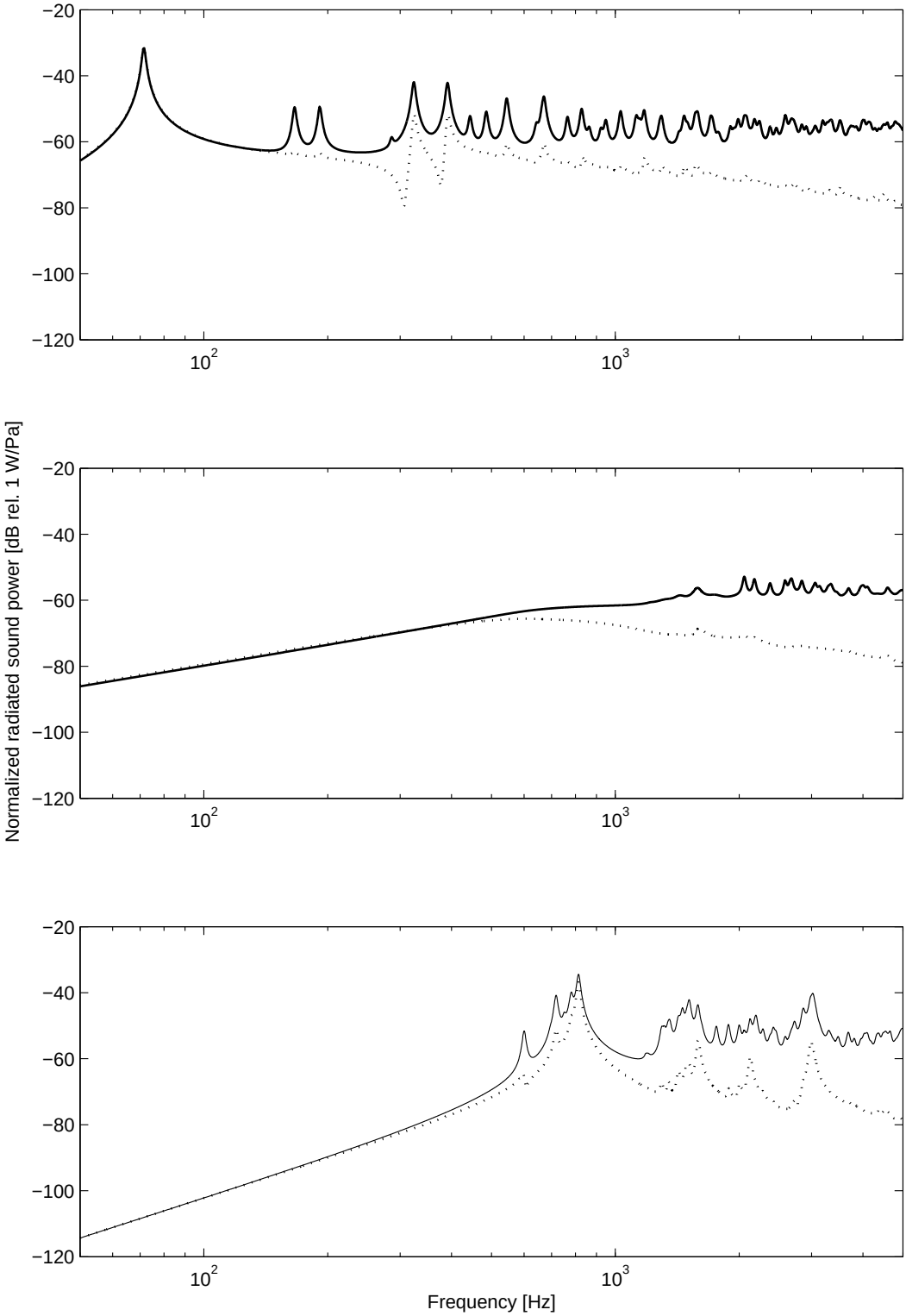

Figure 3.34: Radiated sound power for a plane wave incident with an angle θ=45° and φ=45° $(dotted)$ and random rain on the roof disturbance $(solid)$ for a passive panel without control (top graph), for an 'optimal' velocity feedback gain of 40 (mid graph) and for a 'maximum' control gain of (10^6) (bottom graph) and achieved reduction (bottom graph).

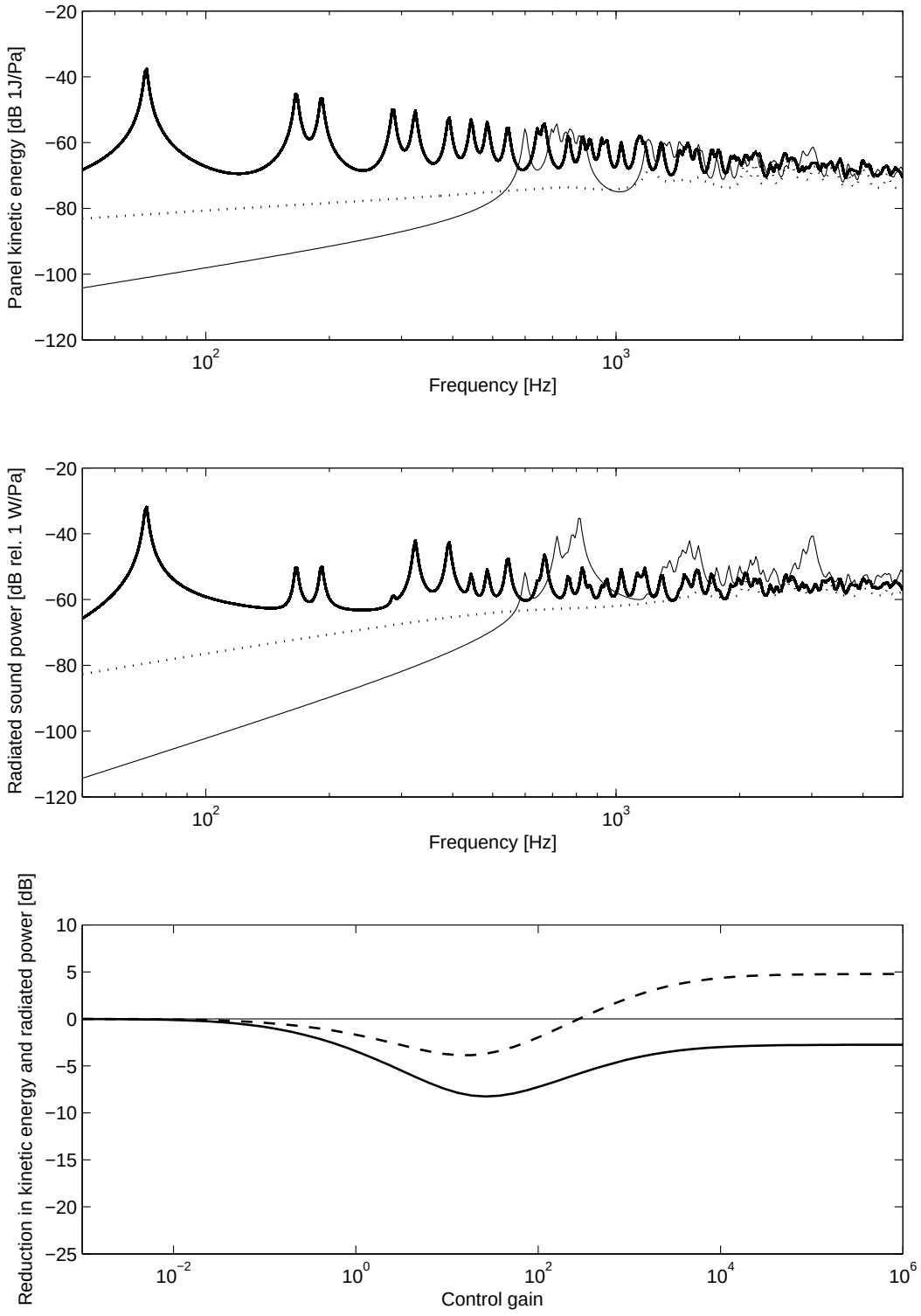

Figure 3.35: Panel kinetic energy, transmission coefficient and achieved reductions for a panel considering rain on the roof disturbance for a range of velocity feedback gains. between 10^-3 and 10^6. Panel kinetic energy (top graph) Transmission coefficient (mid graph), no control ($solid$) optimal control ($dotted$) max control (10^6) ($faint$) and achieved reduction (bottom graph) in total panel kinetic energy ($solid$) and total radiated sound power ($dashed$).

Summary

Within this section the results for three stochastic excitation models i.e. acoustic diffuse field, turbulent boundary layer (TBL) and rain on the roof have been presented. The spectra of the panel kinetic energy and the radiated sound power have been compared to the case of a deterministic acoustic plane wave excitation. For the acoustic diffuse field the results were found to be very similar to those obtained for a plane wave excitation. For the TBL and the rain on the roof disturbance significant differences in the predicted results are observed. It is thought that this can be explained by the different characteristics in spatial correlation. Comparisons of the spatial correlation of the the stochastic excitation models have been presented by Elliott, Maury and Gardonio [5] but have not yet been further investigated within this study.

The main difference between the rain on the roof excitation and the two other disturbances is that it is spatially uncorrelated, independent from frequency. Both acoustic diffuse field and TBL disturbance become increasingly spatially correlated with decreasing frequency. The spectra for the acoustic diffuse field and the TBL disturbance show a characteristic roll of in magnitude with increasing frequency while the spectra for the rain on the roof excitation does not roll off but remains 'constant' with frequency. The panel response to a rain on the roof disturbance can be seen as an average of point responses across the panel surface.

The radiated sound power spectra for the acoustic disturbances show resonance and anti resonance behaviour which is not observed for the two non acoustic disturbances. The anti resonances in the acoustic disturbance cases are thought to be related to the roots in the spatial correlation function which are not present in the correlation functions for the TBL and rain on the roof disturbance.

The relation between panel kinetic energy spectra for the observed disturbances and the corresponding radiated sound power spectra and achieved reductions is not trivial and is found to be different for different disturbances. This indicates that the radiation efficiency of the panel depends on the disturbance, i.e. the sensitivity of single modes to a given disturbance and the constructive or destructive interference between modal contributions to the radiated sound power. To date no systematic investigation on the effect of the disturbance characteristics on the radiation efficiency and control performance of a panel

has been conducted but is suggested for future work within this project.

So far only one typical case of boundary layer disturbance has been considered. During a normal flight cycle of an aircraft the specifications of the boundary layer will change with flight speed, altitude and ambient temperature. Studies on the effect of variability of the turbulent boundary layer disturbance on the sound transmission through a panel and the control performance of a velocity feedback system are suggested as future work within this project.

3.5 Summary

Within this chapter the simulation results of systematic studies on the sound transmission prediction models, developed in Chapter 2 have been presented. Various aspects on the active control of sound transmission through a panel have been addressed and discussed.

Considering the example of two geometrical differently distributed uniform arrays of 16 discrete control forces it was shown that the control point distribution can have a significant influence on the control performance in specific frequency bands. For the observed control point distributions the overall reductions in panel kinetic energy and radiated sound power were significantly different if only the low frequency range up to 1 kHz were considered. Over a wider frequency range up to 5 kHz both cases yield very similar overall reductions.

Symmetric and asymmetric cases of fluid loading for combinations of air and water on the source and the radiating side of the panel were considered to verify the models capability of considering distributed fluid back forces on the panel.

In general the fluid back forces where found to mainly have the effect of additional distributed mass loading on the panel, causing the resonances of the panel to shift down in frequency. For the air to air transmission case also some minor distributed damping effects were observed.

In the case of an air loading on both sides of the panel no significant difference between coupled and uncoupled results was observed and hence it seems to be feasible to neglect fluid back forces in this case.

For all cases involving water on either or both sides of the panel significant differences between the coupled and uncoupled model results have been observed. Due to the high loading forces and hence high additional mass loading on the panel, the resonances are significantly shifted towards lower frequencies. Clear differences in the spectral characteristics between coupled and uncoupled cases have been observed. For the water to water transmission case the sound transmission coefficient tends to 0 dB at higher frequencies, indicating that the panel is not an effective sound barrier under water. This agrees well with classic approximated results for the sound transmission in this case [16]. The comparison for air to water and water to air transmission showed similar spectral characteristics except for a frequency independent offset between the spectra for the radiated sound power and transmission coefficient. These offsets were found to be linked to the different interdependencies on the specific fluid impedances in the estimation of the incident sound power and the radiation resistance.

For the verification of the formulations for arbitrary flexible panel boundaries, the extreme cases of enforced pinned and enforced clamped boundary conditions were studied. Pinned boundary conditions were realised by applying very high linear boundary damping forces along the edges of an initially completely free panel. Clamped conditions were achieved by additionally applying very high boundary damping moments. A second case of clamped boundary conditions was realised by applying high boundary damping moments along the edges of an initially all side pinned panel.

Reasonable overall agreement has been achieved for all enforced boundary cases. The accuracy of the models seem to be limited by the accuracy of the used estimates for the natural panel frequencies and modeshapes of a completely free panel. It is however thought that the formulations derived by Warburton [11] are accurate enough for the objectives in this research project. If a higher accuracy is needed a more exact formulations as those by Gorman [21, 22, 23] could be explored.

A case of flexible linear and rotational springs along the boundary has been utilized to demonstrate that it is actually possible to model arbitrary boundary conditions. Systematic studies on the effect of variable boundary conditions on the panel response and control performance needs yet to be conducted and will be part of the next phase in this project.

Results for three stochastic disturbance models i.e. acoustic diffuse field, turbulent bound-

ary layer and rain on the roof were presented and discussed. The spectra of the panel kinetic energy and the radiated sound power have been compared to the case of a deterministic acoustic plane wave excitation.

For the acoustic diffuse field the results were found to be very similar to those obtained for a plane wave excitation. For the TBL and the rain on the roof disturbance significant differences in the predicted results are observed. It is assumed that these differences are determined by the disturbance specific spatial correlation functions.

Acoustic diffuse field and TBL disturbance become increasingly spatially correlated with decreasing frequency and panel kinetic energy and sound transmission coefficient spectra for both disturbances show a characteristic roll of in magnitude with increasing frequency. The correlation function for the rain on the roof excitation is a simple delta function (spatially uncorrelated) and is frequency independent, therefore the spectra do not roll off but remain 'constant' with frequency. The panel response to a rain on the roof disturbance can be seen as an average of point responses across the panel surface.

The radiated sound power spectra for the acoustic disturbances (plane wave and diffuse field) show resonance and anti resonance behaviour which is not observed for the two non acoustic disturbances. The anti resonances in the acoustic disturbance cases are thought to be related to the roots in the spatial correlation function which are not present in the correlation functions for the TBL and rain on the roof disturbance.

The relation between panel kinetic energy spectra for the observed disturbances and the corresponding radiated sound power spectra and predicted reductions are not trivial and are found to be different for different disturbances. This indicates that the radiation efficiency of the panel depends on the type of disturbance, i.e. the sensitivity of single modes to a given disturbance and the constructive or destructive interaction between modal radiation contributions. To date no systematic investigation on the effect of the disturbance characteristics on the radiation efficiency and control performance of the panel has been conducted but is suggested for future work within this project.

So far only one typical case of boundary layer disturbance has been considered. During a normal flight cycle of an aircraft the specifications of the boundary layer will change with flight speed and altitude. Studies on the effect of variability of the turbulent boundary layer disturbance on the sound transmission through a panel and the control performance

of a velocity feedback system are suggested for future work.

Studies on the variation in the gain of the velocity feedback control loops using collocated point velocity sensor and force actuator pairs were conducted for transmission cases with various control point distributions, boundary conditions, fluid loadings and applied disturbances. For all observed cases a single optimum in velocity feedback control gain was observed.

For the weakly coupled all side pinned panel model under plane wave excitation an optimal velocity feedback gain was found to be about 40. For this value the control forces introduce an optimal amount of damping to low order modes without enhancing the response of higher order modes. For control gains higher than 10^4 the panel appeared to be locally pinned at the control positions, resulting in cancellation of low order modes but in the creation of weakly damped altered panel modes so that no improvement in the overall performance was achieved.

The optimum velocity feedback gain was found to increase with increasing fluid loading on the panel, shifting up to a level of about 300 for the case of water on source and receiving side of the panel.

For the limited range of boundary conditions and disturbances investigated within this study no significant change in the optimal velocity feedback level was observed. Further studies on variable boundaries need yet to be conducted.

The control performance in terms of achieved overall reduction in panel kinetic energy and radiated sound power clearly depend on the considered fluid loading, and applied disturbance. Further studies seem to be necessary to investigate the variability of the control performance for uncertain loading boundary and disturbance parameters.

It was found that the overall achieved control performance across the entire observed frequency range is dominated by the reduction in the response of the fundamental panel mode. The reduction in the linear overall level might not necessarily be a good indicator if the aim is to optimize the control performance in the mid audio frequency range. In this case the control performance should be estimated in a limited frequency band, e.g. 500 Hz to 5 kHz.

Chapter 4

Conclusions

In Chapter 2 a general element based model has been developed and subsequently extended to incorporate fluid loading, feedback control loops using collocated velocity sensors and force actuators and arbitrary flexible boundaries. Formulations for deterministic and stochastic excitation models have been discussed within the the developed framework of matrix formulations.

In Chapter 3 simulation results of systematic studies on the sound transmission prediction models, developed in Chapter 2 have been presented. The results look promising and indicate that the developed modelling framework is a flexible tool that can be used to predict the sound transmissions through a thin panel for a wide variety and range and of parameters. A detailed summary of the outcomes of this chapter is given in Section 3.5.

Future work

Following tasks are suggested for further work within this research project.

- Study on the effect of variable boundary conditions on the panel response and the control performance. This will aim on predicting the variability in the control performance for practical structures comprising thin panels with uncertain boundaries.
- Extension of the observed frequency range beyond the coincidence frequency. The panel response around coincidence is determined by the structural damping of the

panel. It is therefore assumed that active velocity feedback control can be used to achieve a reduction in the panel kinetic energy and the radiated sound power in this critical frequency region.

- Study on the spatial correlation function for different types of deterministic and stochastic disturbances in respect to the resulting panel response, including the investigation of the radiation efficiency of the panel for different types of disturbances. This is to yield a better understanding for the relation ship between the predicted panel kinetic energy and radiated sound power spectra for different types of disturbances.

- So far only a typical case of turbulent boundary layer disturbance has been considered. During a normal flight cycle of an aircraft the specifications of the boundary layer on the outside of the fuselage will change with flight speed, altitude and ambient temperature. Further studies on the variability of the boundary layer and it's effect on the sound transmission and the control performance should be conducted. This study might also consider the effect of small changes in fluid loading due to changes in the properties of air at different altitudes.

Bibliography

[1] Gardonio P. and Elliott S.J. Smart panels for active structural acoustic control. *Smart Materials and Structures*, 13(6):1314–36, 2004.

[2] Brebbia C.A.; Silva J.J.R.S.; Partridge P.W.; edited by Ciskowski R.D. and Brebbia C.A. *Boundaary Element Mehtods in Acoustics*. Computational Mechanics Puplications Southampton Boston / Elservier Applied Science London New York, 1991.

[3] Shorter P.J. and Langley R.S. Vibro-acoustic analysis of complex systems. *Journal of Sound and Vibration*, 288:669–699, 2005.

[4] Elliott S.J. and Johnson M.E. Radiation modes and the active control of sound power. *Journal of the Acoustical Society of America*, 94(4):2194 – 204, 1993/10/.

[5] Elliott S.J.; Maury C.; Gardonio P. The synthesis of spatially correlated random pressure fields. *The Journal of the Acoustical Society of America*, 117(3):1186–1201, 2005.

[6] Corcos G.M. The resolution of pressures in turbulence. *The Journal of the Acoustical Society of America*, 35:192–199, 1963.

[7] Maury C.; Elliott S.J.; Gardonio P.;. Turbulent boundary-layer simulation with an array of loudspeakers. *American Institute of Aeronautics and Astronautics - Journal*, 42(4):706–713, 2004.

[8] Johnson M.E. and Elliott S.J. Active control of sound radiation using volume velocity cancellation. *Journal of the Acoustical Society of America*, 98(4):2174 –, 1995.

[9] Preumont A. *Vibration Control of Active Structures An Introduction*, volume 96 of *Solid Mechanics and its Applications*. Kluwer Academic Publisher, Dordrecht / Boston / London, 2 edition, 2002.

[10] Gardonio P., Brennan M.J.; edited by Fahy F.J., and Walker J.G. *Advanced Applications in Acoustics, Noise and Vibration, Chapter 9: Mobility and impedance methods in structural dynamics*. Spon Press, 2004.

[11] Warburton G.B. The vibration of rectangular plates. *Procedings of the Institute of Mechanical Engineers*, 168:371–384, 1954.

[12] Fahy F.J. and Gardonio P. *Sound and Structural Vibration*. Academic Press, 2 edition, 2007.

[13] Craik R.J.M.;. *Sound Transmission Through Buildings: Using Statistical Energy Analysis*. Gower Publishing Limited, 1996.

[14] Tuma J.J. and Walsh R.A. *Engeneering Mathematics Handbook*. McGraw-Hill, 4 edition, 1997.

[15] Fahy F.J.; edited by Fahy F.J. and Walker J.G. *Fundamentals of NOISE and VIBRATION*. Spon Press, Lodon and New York, 1998.

[16] Fahy F.J. *Sound and Structural Vibration; radiation, tranmission and response*. Academic press, 1985.

[17] Pierce A.D. *ACOUSTICS An Introduction to its Physical Principles and Applications*. Acoustical Society of America, 1994.

[18] McGough R.J. Radiation force and the struve function. Hompepage of the Michigan State University College of Engeneering; http://www.egr.msu.edu/ mcgough/struve/struve.htm; 2007-06-28.

[19] Morse P.M. and Ingard K.U. *Theoretical Acoustics*. Princton University Press, 1968.

[20] Clark R.L.; Saunders W.R.; Gibbs G.P. *Adaptive Structures, Dynamics and Control*. Wiley, New York, NY, 1998.

[21] Gorman D.J. Free vibration analysis of the completely free rectangular plate by the method of superposition. *Journal of Sound and Vibration*, 57(3):437–447, 1978.

[22] Gorman D.J. Free vibration analysis of completely free rectangular plates by the method of superposition-galerkin method. *Journal of Sound and Vibration*, 237(5):901–914, 2000.

[23] Gorman D.J. Accurate free vibration analysis of completely free rectangular mindlin plate. *Journal of Sound and Vibration*, 189(3):341–353, 1996.

[24] Shorter P.J. and Langley R.S. On the reciprocity relationship between direct field radiation and diffuse reverberant loading. *The Journal of the Acoustical Society of America*, 117(1):85–95, 2005.

[25] Gardonio P. and Elliott S.J. Modal response of a beam with a sensor-actuator pair for the implementationof velocity feedback control. *Journal of Sound and Vibration*, 284:1–22, 2005.

[26] Mindlin R.D. Influence of rotary inertia and shear on flexural motion of isotropic elastic plates. *ASME Journal of Applied Mechanics*, 18:31–38, 1951.

[27] Elliott S.J. and Johnson M.E. Radiation modes and the active control of sound power. *Journal of the Acoustical Society of America*, 94(4):2194 – 2204, 1993.

...

Appendix A

Numerical validation of the plate model

Within this appendix a parametric study on the element based panel model, developed in Chapter 2 is presented. The effect of spatial element resolution and the choice for dynamic and residual frequency range will be discussed.

The properties of the all side pinned panel used for the evaluations presented in this appendix are documented in Table 2.1. As excitation a plane acoustic wave incident at an angle $\theta = 45°$ and $\varphi = 45°$ has been considered. The acoustical parameters of the surrounding fluid are taken as those of air at ambient temperature, defined in Table 2.2. The plate dynamics are considered to be unaffected by the fluid loading back forces. Results for a passive panel, and a panel with 16 discrete $(\Delta/2, \Delta, \Delta/2)$ distributed idealized velocity feedback control loops, with a feedback gain of 40 (optimal) and 10^6 (maximum gain, pinned condition) are compared. The frequency spectra are evaluated for a range of 5000 discrete linearly spaced frequencies between 1 Hz and 5 kHz.

Element resolution

For the modelling of the airborne excitation of the panel and the estimation of the panel kinetic energy an elemental approach [1] as developed in Section 2.3 is applied . The panel surface is subdivided in a uniform grid of finite panel elements. The number of elements is defined by the highest mode order of the all side pinned panel in the observed frequency range. Within this study the sensitivity to the numerical results in respect to the

ratio between highest mode order and number of elements in x and y directions across the panel are investigated. The dynamic frequency range has been chosen as twice the maximum frequency of interest ($f_{max,dyn} = 10kHz$) and the residual frequency range has been chosen as twenty times the maximum frequency of interest ($f_{max,res} = 100kHz$).

Figure A.1 shows the predicted panel kinetic energy for a spatial resolution from 1 to 4 elements per highest mode order, this corresponds to 2 to 8 elements per bending wave length. As expected, no differences can be seen in the low frequency region since all setups yield an accurate spatial sampling for low order modes. With increasing frequency the results for the case with a spatial resolution of one element per mode order is deviating from the rest of the results. For the spatial resolutions of 2 to 4 elements per mode order almost no difference can be observed. It is therefore concluded that a spatial resolution of two elements per highest mode order, i.e. 4 elements per bending wavelength, is appropriate.

Figure A.2 shows the total panel kinetic energy integrated over the entire observed frequency range using the trapezoidal rule. The results show that the estimated overall panel kinetic energy is converging with increasing element resolution. Only small changes between the spatial resolution factor of two and the higher factors is observed. It is interesting to note that the effect of the spatial resolution is the highest for the optimal control case. This can explained by the fact that the overall panel kinetic energy for the other two cases, especially the passive panel case, is dominated by contributions of low order modes; changes in the estimation of higher order modes does therefore not have a large effect. For the optimal control case the low order modes are highly damped and are therefore less dominant.

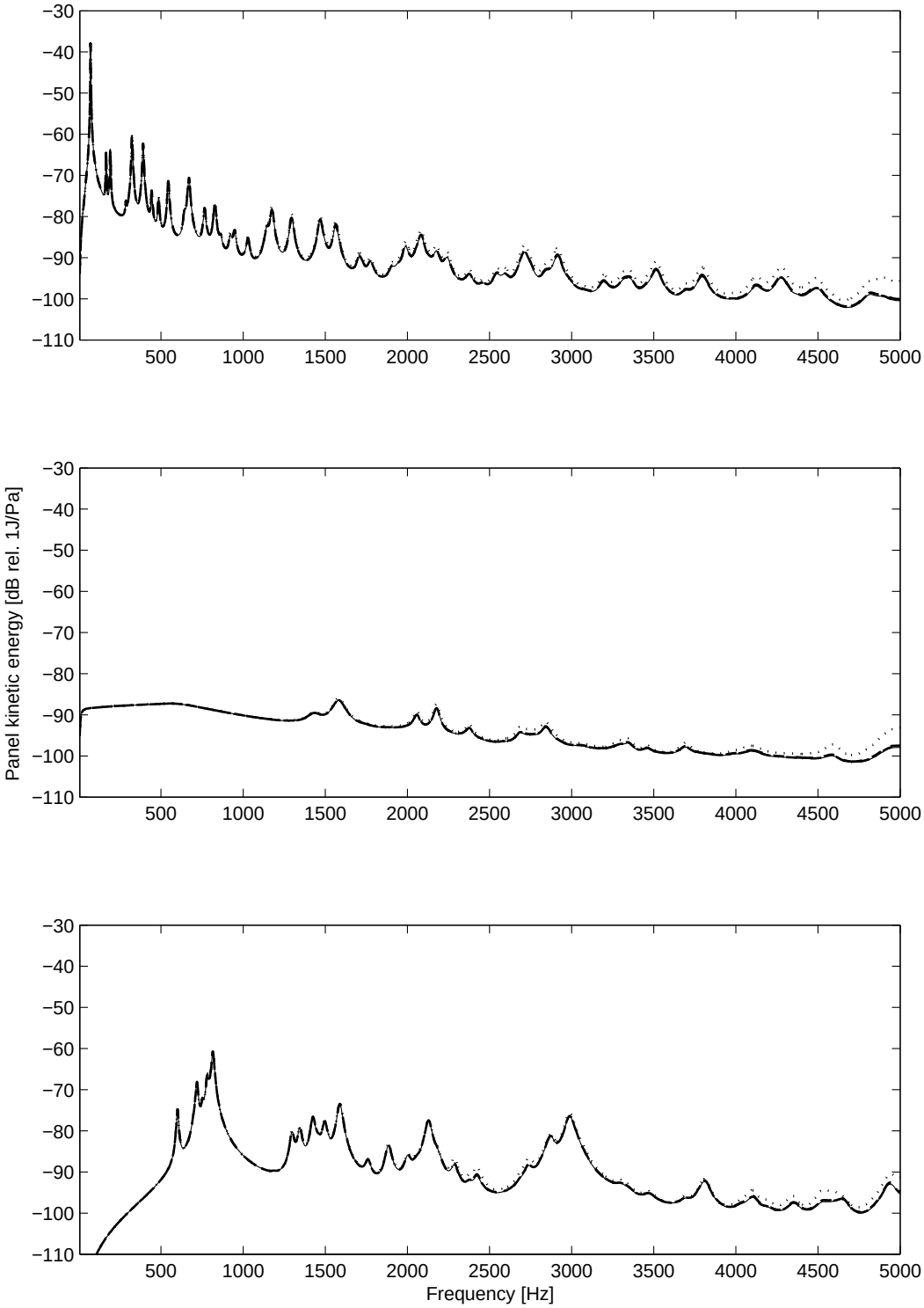

Figure A.1: Predicted panel kinetic energy for a element resolution of 1 $(dotted)$, 2 $(dashed)$, 3 $(dash - dotted)$, 4 $(faint - solid)$ elements per highest mode order, for a panel without control (top graph), an 'optimal' velocity feedback gain of 40 (mid graph) and a 'maximal' feedback gain of 10^6 (bottom graph). Dynamic mode range f_{dyn}/f_{range} = 2 (10 kHz), residual mode range of f_{res}/f_{range} = 20 (100 kHz)

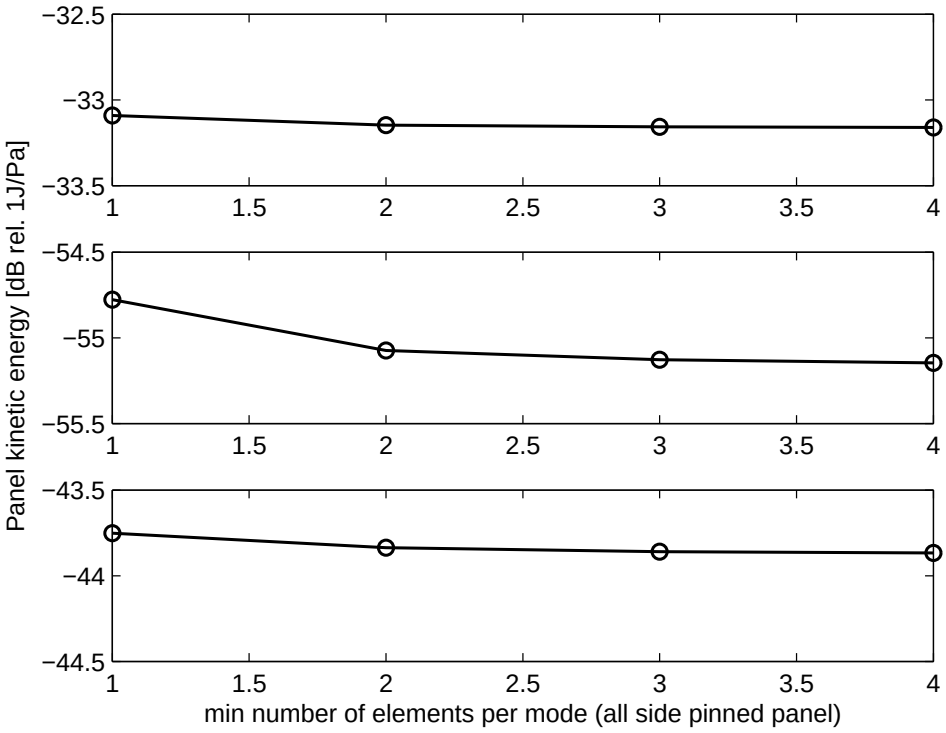

Figure A.2: Predicted total panel kinetic energy depending on the chosen element resolution for a panel without control (top graph), an 'optimal' velocity feedback gain of 40 (mid graph) and a 'maximal' feedback gain of 10^6 (bottom graph) . Dynamic mode range f_{dyn}/f_{range} = 2 (10 kHz), residual mode range of f_{res}/f_{range} = 20 (100 kHz)

Frequency limit for dynamic and residual modes

For the dynamic plate model used within this study the evaluation has been subdivided into three frequency regions, the actually observed frequency range, from 0 Hz to $f_{max,range}$, a frequency range for which dynamic modes are considered, from $f_{max,range}$ to $f_{max,dyn}$ and a frequency range for which only the residual terms of the modes are considered, ranging from $f_{max,dyn}$ to $f_{max,res}$. Within this Appendix the limits for these frequency regions in terms of convergence and relative error in overall panel kinetic energy is investigated.

dynamic modes

Figure A.3 shows the predicted panel energy calculated for dynamic frequency ranges from 1 to 5 times the highest observed frequency. The residual frequency range has been

held constant at 20 times the highest observed frequency ($f_{max,res}$=100 kHz). For the passive and the optimal control almost no differences can be observed except for the case where only modes in the observed frequency range are treated as dynamic modes. The result is a lower response at the upper end of the observed frequency spectrum. For the maximum control case however frequency shifts in the resonance peaks can be observed above 2500 Hz. This indicates that the contributions of higher order modes beyond the observed frequency range are of importance for cases with high level of active control.

The results for the estimated overall panel kinetic energy in Figure A.4 shows that there is no difference in the overall kinetic energy estimation for the passive panel. As discussed before, the optimal control case is less dominated by contributions of lower order modes, changes at the upper end of the observed frequency spectrum are therefore more dominate. Both control cases show similar convergence behaviour. A dynamic range factor of ≥ 2 seems to be yield appropriately accurate results for all three cases.

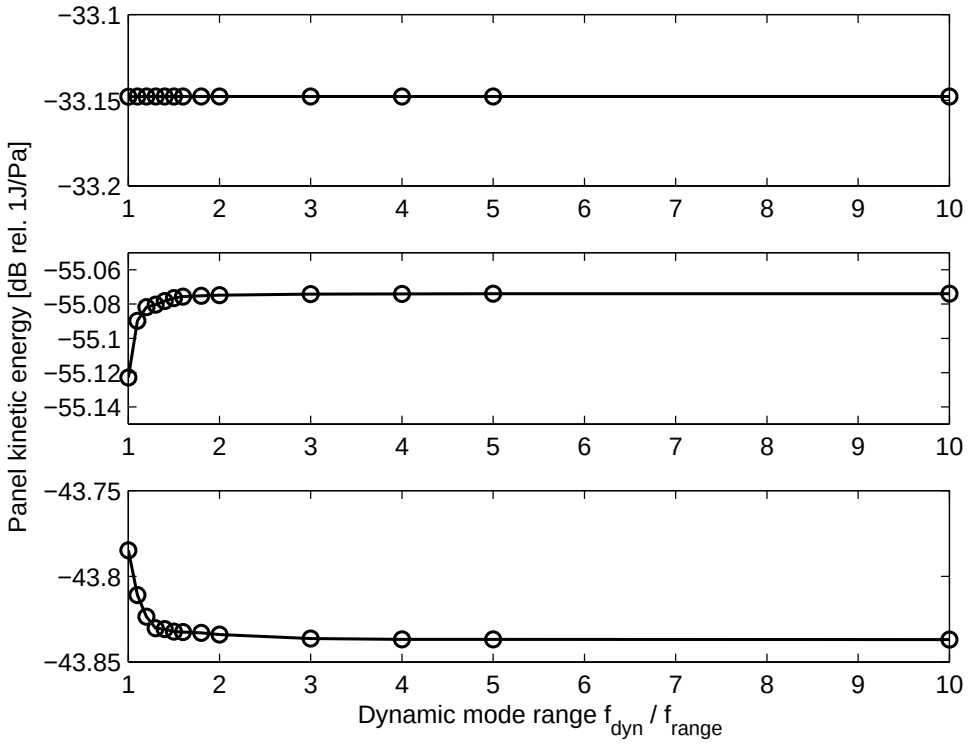

Figure A.4: Predicted total kinetic energy depending on the chosen dynamic mode range f_{dyn}/f_{range} for a panel without control (top graph), an 'optimal' velocity feedback gain of 40 (mid graph) and a 'maximal' feedback gain of 10^6 (bottom graph). Residual mode range: f_{res}/f_{range} = 20 (100 kHz); element resolution: 4 elements per highest mode order.

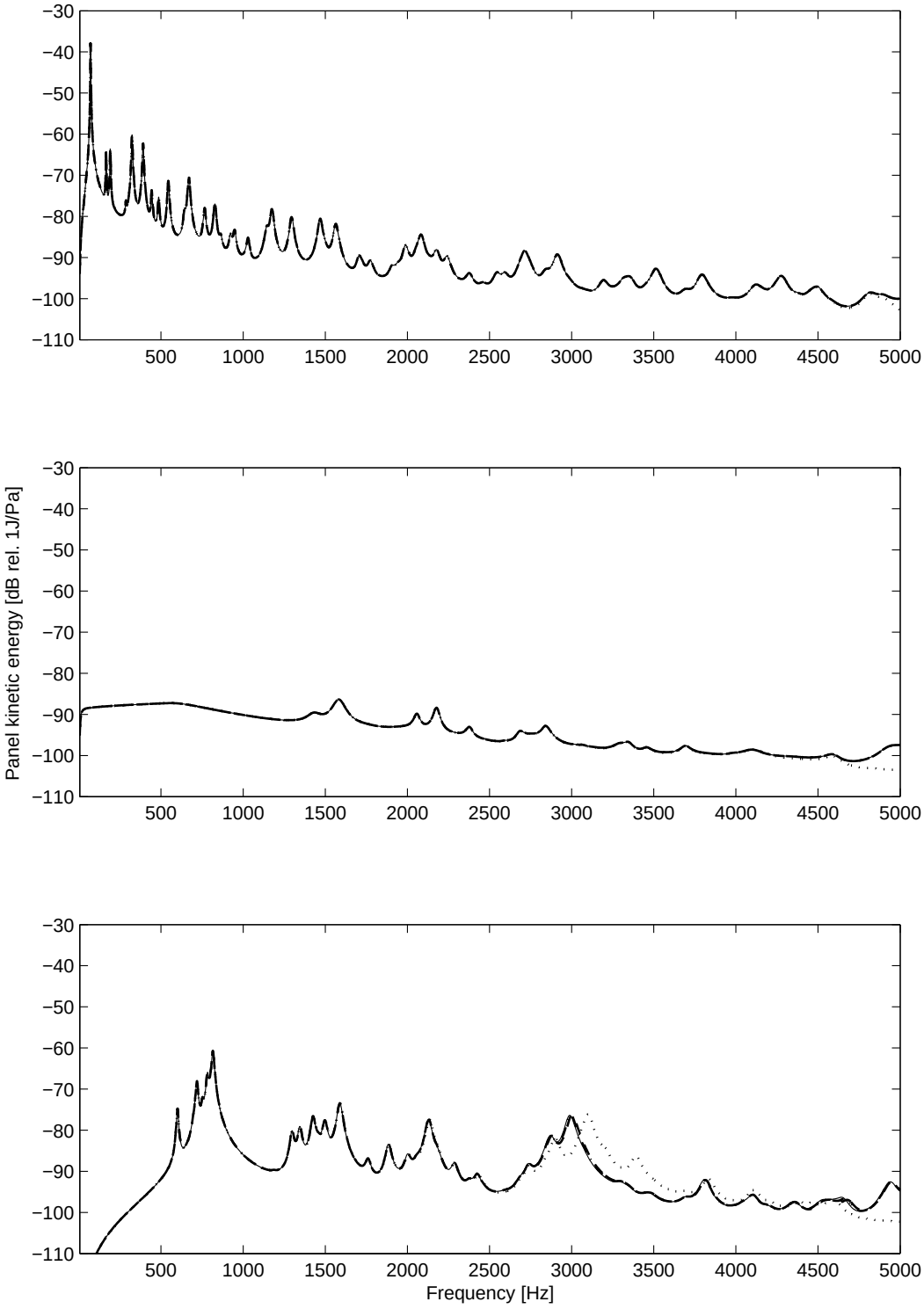

Figure A.3: Predicted panel kinetic energy calculated using a dynamic mode range of f_{dyn}/f_{range} =1 $(dotted)$, 1.5 $(dashed)$, 2 $(dash-dotted)$, 5 $(faint-solid)$ for a panel without control (top graph), an 'optimal' velocity feedback gain of 40 (mid graph) and a 'maximal' feedback gain of 10^6 (bottom graph). Residual mode range: f_{res}/f_{range} = 20 (100 kHz); element resolution: 4 elements per highest mode order.

Residual modes

The contribution of the residual modes towards the dynamic stiffens of the panel is assumed to be independent from the actual observed frequency. This assumption is valid if the observed frequency is much smaller than the natural frequency of the residual mode. Higher order modes can therefore be calculated outside the main frequency loop and can therefore save computation time while only introducing relatively small numerical error.

Figure A.5 shows the results for a residual frequency range from 5 to 100 times the highest observed frequency (25 kHz to 500 kHz). The dynamic mode range has been fixed to twice the highest observed frequency (10 kHz). The figures show that changes in the residual frequency range do not at all affect the evaluated kinetic energy of the passive panel and the panel with optimal control. The kinetic energy estimated for a maximum velocity feedback with an control gain of 10^6 shows some sensitivity to the considered residual frequency range. With increasing residual frequency range the resonance peaks shift downwards in frequency, converging to a common spectrum.

One should note that a feedback gain of 10^6 is a theoretical value that might never be matched in a real application. For such a high velocity feedback gain the panel appears to be pinned at the control positions, which creates a system with different modal behaviour than the uncontrolled panel [25]. The effect of changes in feedback gain have been discussed in section 3.1. For the estimation of a reasonable limit for the residual frequency range this extreme feedback gain was chosen because the dynamic behaviour of the structure is supposed to be most sensitive to the residual mode contributions under these conditions.

Figure A.6 shows the overall panel kinetic energy for different cases of residual frequency ranges. As for the dynamic frequency range there are no changes for the case of a passive model. The results for the two control cases are converging with increasing residual frequency range. A reasonable limit for the evaluation seems to be ratio of ≥ 20 between the frequency range of interest and the frequency limit for the residual modes.

One should note that although using this residual mode approach allows to consider modes up to excessive high frequencies i.e. mode orders, the accuracy of the results is limited by the applied thin plate assumptions. This assumptions hold true for high ratio between

bending wavelength and plate thickness. For ratios below 10 the thin plate model breaks down and Mindlin plate theory [26] i.e. rotary inertia and shear need to be considered. For the 1 mm thin aluminium panel studied here this criterion is valid up to 97.5 kHz; even at 250 kHz the bending wave length is 6 times larger than the panel height.

For computational evaluation the frequency range for residual modes is limited by the size of the $[M_{res}, M_{res}]$ residual omega matrix $\tilde{\mathbf{\Omega}}_{res}$ (Equation (2.12)).

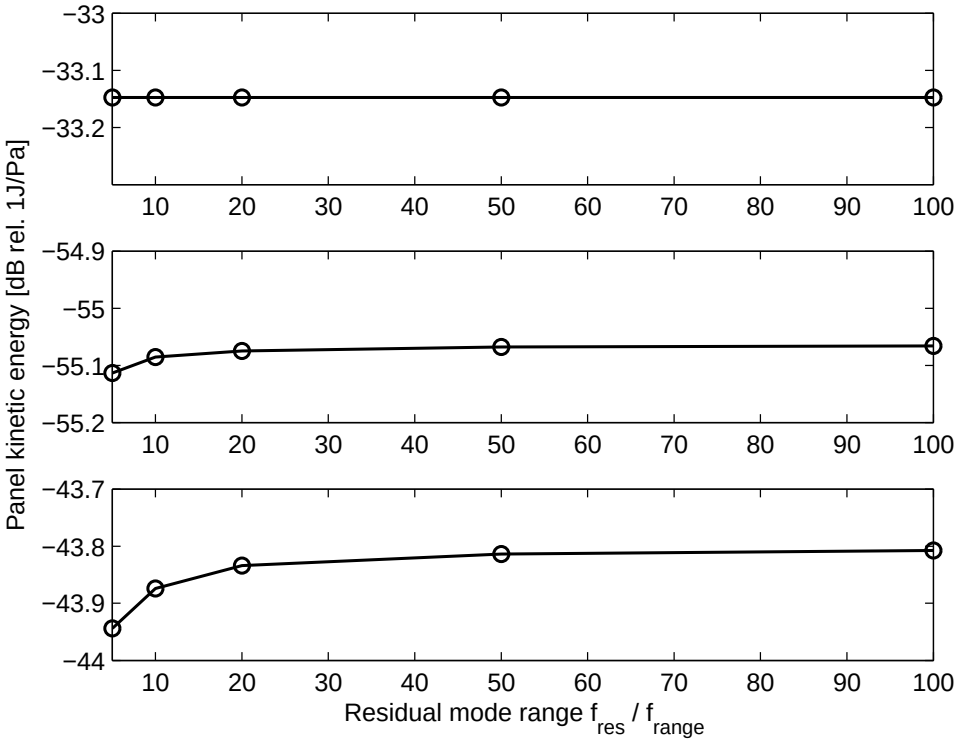

Figure A.6: Predicted total kinetic energy depending on the chosen residual mode range f_{res}/f_{range} for a panel without control (top graph), an 'optimal' velocity feedback gain of 40 (mid graph) and a 'maximal' feedback gain of 10^6 (bottom graph). Dynamic mode range: f_{dyn}/f_{range} = 2 (10 kHz); element resolution: 4 elements per highest mode order.

Summary of parameters

Within this appendix a parametric study on the element based panel model, developed in Chapter 2 has been presented. The affect of spatial element resolution and the choice for dynamic and residual frequency range has bee discussed. Minimum limits for each of these three parameter have been suggested and discussed. The minimum values thought to be adequate for accurate prediction of the panel kinetic energy and radiated sound power

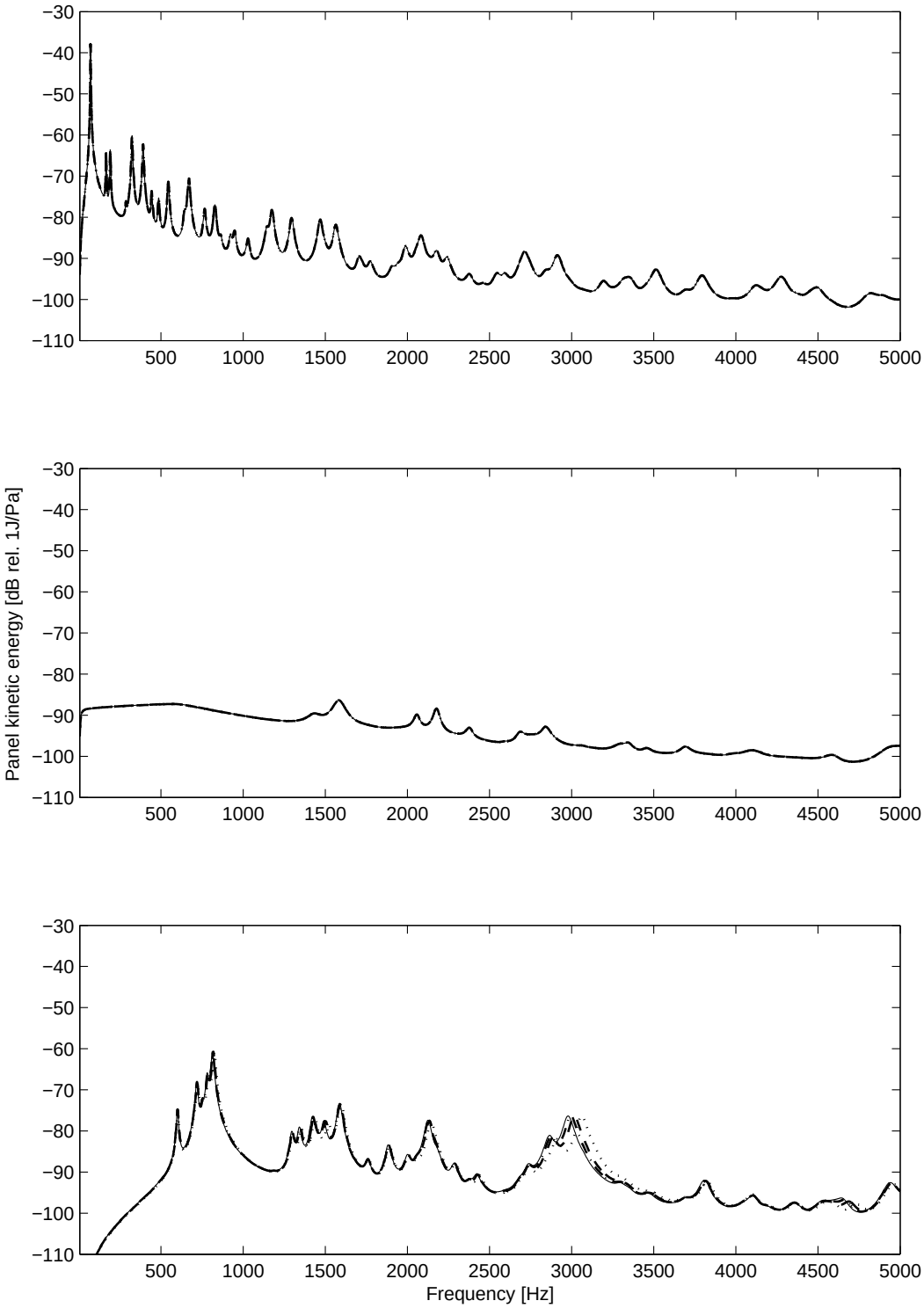

Figure A.5: Predicted panel kinetic energy calculated using a dynamic mode range of f_{res}/f_{range} = 5 (25 kHz) $(dotted)$, 10 (50 kHz) $(dashed)$, 20 (100 kHz) $(dash - dotted)$, 100 (500 kHz) $(faint - solid)$ for a panel without control (top graph), an 'optimal' velocity feedback gain of 40 (mid graph) and a 'maximal' feedback gain of 10^6 (bottom graph). Dynamic mode range: f_{dyn}/f_{range} = 2 (10 kHz); element resolution: 4 elements per highest mode order.

are summarized in Table A.1 below.

Table A.1: Parameters for Numerical evaluation

Parameter	Criterion	Unit
Spatial resolution	$N_{ex} \geq 2 \times n_{1,max}, i.e. N_{ex} \geq 4 \times \frac{l_x}{\lambda_{min}}$ $N_{ey} \geq 2 \times n_{2,max}, i.e. N_{ey} \geq 4 \times \frac{l_y}{\lambda_{min}}$	
Dynamic frequency limit	$f_{max,dyn} \geq 2 \times f_{max,range}$	Hz
Residual frequency limit	$f_{max,res} \geq 20 \times f_{max,range}$	Hz

Appendix B

Formulations for rectangular plates

Within this Appendix the formulations for mode shapes and natural frequencies and modal expansion terms for the point and transfer receptance of thin rectangular plates as used in this report are briefly summarized. For further discussion the interested reader is referred to Gardonio and Brennan [10] and Warburton [11].

Definition of plate properties

The geometric and dynamic properties of the panel are given as:

- Panel surface A_p [m^2]:

$$A_p = l_x l_y \tag{B.1}$$

- Mass per unit area: $\rho_{s,p}$ [kg/m^2]:

$$\rho_{s,p} = \rho_p h_p \tag{B.2}$$

- Panel mass m_p [kg]:

$$m_p = A_p \rho_{s,p} \tag{B.3}$$

- Bending stiffness D_p [N m]:

$$D_p = \frac{E_p h_p^3}{12(1-\nu_p^2)} \tag{B.4}$$

Natural frequencies and mode shapes

The natural frequencies for rectangular plates $\omega_{nat,p}$ [rad/s] for any type of boundary are given by [11]

$$\omega_{nat,p,n}(n_1,n_2) = \sqrt{\frac{D_p}{\rho_{s,p}}}\left(\frac{\pi}{l_x}\right)^2 q(n_1,n_2) \tag{B.5}$$

where the factor $q(n_1,n_2)$ is given by

$$q(n_1,n_2) = \sqrt{G_x^4(n_1) + G_y^4(n_2)\left(\frac{l_x}{l_y}\right)^4 + 2\left(\frac{l_x}{l_y}\right)^2 [\nu_p H_x(n_1)H_y(n_2) + (1-\nu_p)J_x(n_1)J_y(n_2)]} \tag{B.6}$$

The constants G_x, H_x, J_x and G_y, H_y, J_y are given in Table B.1.

For the all side pinned boundary condition Equation (B.5) with the formulations in Table B.1 yields the formulation for the natural frequencies $\omega_{nat,p}$ [rad/s] as

$$\omega_{nat,p,n}(n_1,n_2) = \sqrt{\frac{D_p}{\rho_{s,p}}}\left[\left(\frac{n_1\pi}{l_x}\right)^2 + \left(\frac{n_2\pi}{l_y}\right)^2\right] \tag{B.7}$$

The mass normalized mode shapes ψ_p are given by

$$\psi_{p,n} = 2\sin\left(\frac{n_1\pi x}{l_x}\right)\sin\left(\frac{n_2\pi y}{l_y}\right) \tag{B.8}$$

Table B.1: Constants for the the variables G_x, H_x, J_x and G_y, H_y, J_y for all side pinned and side clamped and all side free boundary conditions; taken from [10].

Boundary conditions	n	G	H	J
P-P-P-P $w(0) = 0$ $w''(0) = 0$ $w(L) = 0$ $w''(L) = 0$	1,2,3,...	n	n^2	n^2
C-C-C-C $w(0) = 0$ $w'(0) = 0$ $w(L) = 0$ $w'(L) = 0$	1	1.506	1.248	
	$2, 3, 4...$	$n + \frac{1}{2}$	$\left(n + \frac{1}{2}\right)^2 \times \left[1 - \frac{4}{(2n+1)\pi}\right]$	
F-F-F-F $w''(0) = 0$ $w'''(0) = 0$ $w''(L) = 0$ $w'''(L) = 0$	even	0	0	0
	rocking	0	0	$12/\pi^2$
	1	1.506	1.248	5.017
	$2, 3, 4...$	$n + \frac{1}{2}$	$\left(n + \frac{1}{2}\right)^2 \times \left[1 - \frac{4}{(2n+1)\pi}\right]$	$\left(n + \frac{1}{2}\right)^2 \times \left[1 + \frac{12}{(2n+1)\pi}\right]$

Table B.2: Characteristic beam functions for all side pinned, all side clamped and all side free boundary conditions; taken from [10].

Boundary conditions	$\theta_{1,3,5...}(x)$ with $i = (n+1)/2$	$\theta_{2,4,6...}(x)$ with $j = (n/2)$
P-P-P-P $w(0) = 0$ $w''(0) = 0$ $w(L) = 0$ $w''(L) = 0$	$\theta_n(x) = \sqrt{2}\sin\left(\frac{n\pi x}{l_x}\right)$	
C-C-C-C $w(0) = 0$ $w'(0) = 0$ $w(L) = 0$ $w'(L) = 0$	$\theta_n(x) = \sqrt{2}\left\{\cos\left[\gamma_i\left(\frac{x}{l_x}-\frac{1}{2}\right)\right] + k_n\cosh\left[\gamma_i\left(\frac{x}{l_x}-\frac{1}{2}\right)\right]\right\}$ $k_n = -\frac{\sin\left(\frac{\gamma_i}{2}\right)}{\sinh\left(\frac{\gamma_i}{2}\right)}$ with $\tan\left(\frac{\gamma_i}{2}\right) + \tanh\left(\frac{\gamma_i}{2}\right) = 0$	$\theta_n(x) = \sqrt{2}\left\{\sin\left[\gamma_i\left(\frac{x}{l_x}-\frac{1}{2}\right)\right] + k_n\sinh\left[\gamma_i\left(\frac{x}{l_x}-\frac{1}{2}\right)\right]\right\}$ $k_n = \frac{\sin\left(\frac{\gamma_j}{2}\right)}{\sinh\left(\frac{\gamma_j}{2}\right)}$ with $\tan\left(\frac{\gamma_j}{2}\right) - \tanh\left(\frac{\gamma_j}{2}\right) = 0$
F-F-F-F $w''(0) = 0$ $w'''(0) = 0$ $w''(L) = 0$ $w'''(L) = 0$	$\theta_{even_n}(x) = 1$ $\theta_{rocking_n}(x) = \sqrt{3}(1 - \frac{2x}{l})$	
	$\theta_n(x) = \sqrt{2}\left\{\cos\left[\gamma_i\left(\frac{x}{l_x}-\frac{1}{2}\right)\right] + k_n\cosh\left[\gamma_i\left(\frac{x}{l_x}-\frac{1}{2}\right)\right]\right\}$ $k_n = -\frac{\sin\left(\frac{\gamma_i}{2}\right)}{\sinh\left(\frac{\gamma_i}{2}\right)}$ with $\tan\left(\frac{\gamma_i}{2}\right) + \tanh\left(\frac{\gamma_i}{2}\right) = 0$	$\theta_n(x) = \sqrt{2}\left\{\sin\left[\gamma_i\left(\frac{x}{l_x}-\frac{1}{2}\right)\right] + k_n\sinh\left[\gamma_i\left(\frac{x}{l_x}-\frac{1}{2}\right)\right]\right\}$ $k_n = \frac{\sin\left(\frac{\gamma_j}{2}\right)}{\sinh\left(\frac{\gamma_j}{2}\right)}$ with $\tan\left(\frac{\gamma_j}{2}\right) - \tanh\left(\frac{\gamma_j}{2}\right) = 0$

Note that the first values for γ can be determined using numerical root find methods, where it is important to yield results with a high precision. For values larger than 10 the numerical methods can fail to determine the roots correctly. For i higher than 10, γ_i is given by

$$\gamma_i = \frac{(4i+1)\pi}{2} \quad \text{for} \quad \tan\left(\frac{\gamma_i}{2}\right) - \tanh\left(\frac{\gamma_i}{2}\right), \tag{B.9}$$

as

$$\gamma_i = \frac{(4i-1)\pi}{2} \quad \text{for} \quad \tan\left(\frac{\gamma_i}{2}\right) + \tanh\left(\frac{\gamma_i}{2}\right) \tag{B.10}$$

respectively.

Linear and rotational panel receptance terms

The modal expansion terms for the nine possible combinations of mass normalized linear and rotational force and moment acceptance terms are [**?**]:

$$\tilde{G}_{w,F}(\omega) = \sum_{n=1}^{\infty}\sum_{m=1}^{\infty} \frac{\psi_{m,n}(x_r, y_r)\,\psi_{m,n}(x_s, y_s)}{\omega_{m,n}^2(1+j\eta_p) - \omega^2}, \tag{B.11}$$

$$\tilde{G}_{w,M_x}(\omega) = \sum_{n=1}^{\infty}\sum_{m=1}^{\infty} \frac{\psi_{m,n}(x_r, y_r)\,\psi^x_{m,n}(x_s, y_s)}{\omega_{m,n}^2(1+j\eta_p) - \omega^2}, \tag{B.12}$$

$$\tilde{G}_{w,My}(\omega) = \sum_{n=1}^{\infty}\sum_{m=1}^{\infty} \frac{\psi_{m,n}(x_r, y_r)\,\psi^y_{m,n}(x_s, y_s)}{\omega_{m,n}^2(1+j\eta_p) - \omega^2}, \tag{B.13}$$

$$\tilde{G}_{\Theta_x,F}(\omega) = \sum_{n=1}^{\infty}\sum_{m=1}^{\infty} \frac{\psi^x_{m,n}(x_r, y_r)\,\psi_{m,n}(x_s, y_s)}{\omega_{m,n}^2(1+j\eta_p) - \omega^2}, \tag{B.14}$$

$$\tilde{G}_{\Theta_x,M_x}(\omega) = \sum_{n=1}^{\infty}\sum_{m=1}^{\infty} \frac{\psi^x_{m,n}(x_r, y_r)\,\psi^x_{m,n}(x_s, y_s)}{\omega_{m,n}^2(1+j\eta_p) - \omega^2}, \tag{B.15}$$

$$\tilde{G}_{\Theta_x,My}(\omega) = \sum_{n=1}^{\infty}\sum_{m=1}^{\infty} \frac{\psi^x_{m,n}(x_r, y_r)\,\psi^y_{m,n}(x_s, y_s)}{\omega_{m,n}^2(1+j\eta_p) - \omega^2}, \tag{B.16}$$

$$\tilde{G}_{\Theta_y,F}(\omega) = \sum_{n=1}^{\infty}\sum_{m=1}^{\infty} \frac{\psi^y_{m,n}(x_r, y_r)\,\psi_{m,n}(x_s, y_s)}{\omega^2_{m,n}(1 + j\eta_p) - \omega^2}, \tag{B.17}$$

$$\tilde{G}_{\Theta_y,M_x}(\omega) = \sum_{n=1}^{\infty}\sum_{m=1}^{\infty} \frac{\psi^y_{m,n}(x_r, y_r)\,\psi^x_{m,n}(x_s, y_s)}{\omega^2_{m,n}(1 + j\eta_p) - \omega^2}, \tag{B.18}$$

$$\tilde{G}_{\Theta_y,My}(\omega) = \sum_{n=1}^{\infty}\sum_{m=1}^{\infty} \frac{\psi^y_{m,n}(x_r, y_r)\,\psi^y_{m,n}(x_s, y_s)}{\omega^2_{m,n}(1 + j\eta_p) - \omega^2}, \tag{B.19}$$

where the rotational modeshape functions $\psi^x_{m,n}(x, y)$ and $\psi^y_{m,n}(x, y)$ are given by

$$\psi^x_{m,n}(x, y) = \phi_m(x)\frac{\partial\phi_n(y)}{\partial y}, \tag{B.20}$$

$$\psi^y_{m,n}(x, y) = -\frac{\partial\phi_m(x)}{\partial x}\phi_n(y), \tag{B.21}$$

respectively.

Appendix C

Radiation impedance of panel elements

Within this study the radiation impedance of the panel elements was approximated as that of an circular piston of equal surface area, this gives consistent results with the radiation model suggested by Elliott and Johnson [27]. Within this Appendix the radiation impedance of a circular piston and alternatively that of a rectangular piston is discussed and compared.

According to Fahy and Gardonio [12] the radiation impedance of a general plane surface in a rigid baffle can be expressed in terms of the following double surface integral

$$\tilde{Z}_{rad} = \frac{j\omega\rho_0}{2\pi} \int_{A_s} \int_{A_r} \frac{e^{-jk_0 r}}{r} dA_s dA_r. \tag{C.1}$$

Full details about the evaluation of the double integral for a circular piston sitting in a rigid baffle are discussed by Pierce [17] and Morse and Ingard [19]. Morse and Ingard [19] also derive the solution for a rectangular piston with edge length a and b. In both references the complex radiation impedance is expressed in terms of the radiation resistance the radiation reactance R_{rad} and X_{rad}

$$\tilde{Z}_{rad} = \rho_0 c_0 A(R_{rad} + jX_{rad}), \tag{C.2}$$

where A_e denotes the Piston surface area. Note that the sign of the imaginary part depends on the definition of the time dependance of the harmonic motion. Within this report the time dependency has been defined as $e^{j\omega t}$.

Circular piston

Pierce [17] gives the solution for the radiation resistance R_O and radiation reactance X_O terms of a circular piston as

$$R_O(k_0 d) = 1 - \frac{2J_1(k_0 d)}{k_0 d} \tag{C.3}$$

$$X_O(k_0 d) = \frac{2M_1(k_0 d)}{k_0 d}. \tag{C.4}$$

where k_0 is the wavenumber, d is the piston diameter, J_1 denotes the first order Bessel unction and M_1 denotes the first order Struve function.

Rectangular piston

Morse and Ingard [19] give the the radiation resistance $R_\square$ and the radiation reactance $X_\square$ terms for a rectangular piston as

$$R_\square \simeq \frac{a^2\mathfrak{R}_\square(k_0 a) - b^2\mathfrak{R}_\square(k_0 b)}{a^2 - b^2}, \tag{C.5}$$

$$X_\square \simeq \frac{a^2\mathfrak{X}_\square(k_0 a) - b^2\mathfrak{X}_\square(k_0 b)}{a^2 - b^2} \tag{C.6}$$

where the edge length dependent resistance and reactance terms $\mathfrak{R}_\square$ and $\mathfrak{X}_\square$ are given as

$$\mathfrak{R}_\square(z) = 1 - 4\frac{1 - J_0(z)}{z^2}, \tag{C.7}$$

$$\mathfrak{X}_\square(z) = 1 - \frac{\pi}{2z}M_0(z), \tag{C.8}$$

here J_0 denotes the zero order Bessel function and M_0 denotes the zero order Struve function. For a nearly square piston with $a \to b$ the radiation impedance tends to that of

an circular piston of diameter d but surface area $A = d^2$.

Approximations

Algorithms for an accurate estimations of zero and first order Bessel and Struve functions for arbitrary arguments are partly part of the the MATLAB standard function package or can be found in on-line libraries [18]. Morse and Ingard [19] and Pierce [17] however provide useful approximate expressions either valid for arguments much smaller than 1 or arguments much larger than 1.

For a circular piston Pierce [17] finds an approximation to the first order Bessel and Struve functions for small arguments ($k_0 d \ll 1$) in terms of Taylor series. Radiation resistance and reactance are than given as

$$R_O(k_0 d) = \rho_0 c_0 \pi \left(\frac{d}{2}\right)^2 \left[\frac{(k_0 d)^2}{2^2 \times 1! \times 2!} - \frac{(k_0 d)^4}{2^4 \times 2! \times 3!} + \frac{(k_0 d)^6}{2^6 \times 3! \times 4!} - \ldots\right] \tag{C.9}$$

$$\tilde{X}_O(k_0 d) = j\rho_0 c_0 d^2 \left[\frac{k_0 d}{3} - \frac{(k_0 d)^3}{5 \times 3^2} + \frac{(k_0 d)^5}{7 \times 5^2 \times 3^2} - \ldots\right]. \tag{C.10}$$

Ignoring higher order terms results in a first order low frequency approximation for the self radiation impedance of a circular piston of the form

$$\tilde{Z}_{rad,O}(\omega) = \frac{\omega^2 \rho_0 A^2}{2\pi c_0} \left[1 + j\frac{16 c_0}{3\omega\sqrt{\pi A}}\right]. \tag{C.11}$$

Similarly Morse and Ingard [19] give an approximation for the radiation impedance of a rectangular piston valid for values of $k_0 a$ and $k_0 b$ much smaller than unity

$$\tilde{Z}_{rad,\square}(\omega) = rho_0 c_0 A \left(= \frac{1}{16} k_0^2 \left(a^2 + b^2\right) + \frac{i8}{9\pi} k_0 \frac{a^2 + ab + b^2}{a + b}\right). \tag{C.12}$$

In the case of a nearly square piston, i.e. in the limit that $a \to b$ this approximation simplifies to

$$\tilde{Z}_{rad,\square}(\omega) = \frac{\omega^2 \rho_0 A^2}{8c_0} \left[1 + j\frac{32c_0}{3\pi\omega\sqrt{A}}\right]. \tag{C.13}$$

As indicated before this is equivalent to the impedance of a circular piston of diameter a but surface area $A = a^2$. The approximated results for a circular and and nearly square piston in Equation (C.11) and Equation (C.13) are therefore very similar. Assuming an identical surface area A, the real part of the radiation impedance of a rectangular piston is a factor $\pi/4 = 0.785$ times smaller than that of a circular piston. The imaginary part of the radiation impedance of a rectangular piston is a factor $\sqrt{\pi}/2 = 0.886$ times smaller than that of a circular piston.